

See discussions, stats, and author profiles for this publication at: <https://www.researchgate.net/publication/296695475>

# The Limits of Visual Resolution

Thesis · December 2009

---

CITATIONS

0

READS

399

1 author:



Ethan A Rossi

University of Pittsburgh

36 PUBLICATIONS 757 CITATIONS

SEE PROFILE

The Limits of Visual Resolution

by

Ethan Andrew Rossi

A dissertation submitted in partial satisfaction of the

requirements for the degree of

Doctor of Philosophy

in

Vision Science

in the

Graduate Division

of the

University of California, Berkeley

Committee in charge:

Professor Austin Roorda, Chair

Professor Karen K. De Valois

Professor James R. Graham

Professor Dennis M. Levi

Fall 2009

The Limits of Visual Resolution

© 2009

by Ethan Andrew Rossi

## Abstract

The Limits of Visual Resolution

by

Ethan Andrew Rossi

Doctor of Philosophy in Vision Science

University of California, Berkeley

Professor Austin Roorda, Chair

Visual resolution, the ability to see fine spatial detail, emerges from the capacities of both the eye and the brain. A great deal of insight into the anatomical and physiological basis of human visual resolution has been gained since Helmholtz first proposed his sampling theory of visual resolution. Anatomical, physiological and psychophysical investigations have revealed in great detail the properties of the biological structures underlying visual resolution and identified many of the optical, retinal, and cortical factors that govern the limits of visual resolution. However, technological limitations have long prevented researchers from examining both the structure and function of the visual system simultaneously in the living eye. The microscopic photoreceptors of the retina have been inaccessible to optical examination, preventing high quality measurements of both visual resolution and retinal anatomy from being obtained in the same eyes. The present studies investigated the relationship between the optical, retinal, and cortical factors that govern visual resolution in humans. These experiments employed adaptive optics scanning laser ophthalmoscopy (AOSLO) as a tool to study how these factors govern visual resolution in normal and diseased eyes. The AOSLO is an ideal tool for studying the limits of vision because of its ability to present complex stimuli to the retina that are of higher optical quality than the visual system has ever experienced, while simultaneously imaging the underlying cone photoreceptor mosaic on a microscopic scale.

Adaptive optics correction of ocular aberrations allowed observers to achieve immediate and significant improvements in visual resolution. Training was not required to achieve this benefit, which allowed the resolving capacity of the retinal and cortical visual system to be assessed unobstructed by the optics of the eye. Not all participants in these studies benefited to the same extent from AO correction. Visual resolution was found to be significantly poorer in low myopia as compared to emmetropia, despite the similar optical quality afforded by AO correction, showing that retinal and cortical changes in myopia caused the observed deficit. Simultaneous imaging and visual resolution testing determined the precise relationship between the spatial sampling limit of the cone mosaic and visual resolution across the human fovea. These studies revealed that the spatial sampling limit of the cone mosaic largely governs visual resolution at the center of the fovea for normal eyes, but that outside the foveal center visual resolution falls off at a greater rate than predicted by cone spacing and is governed by the spatial sampling limit of the mosaic of midget retinal ganglion cells.

Significant differences between otherwise normally appearing observers were revealed using AOSLO, showing the power of visual resolution testing after AO correction for detecting small changes in the visual system resulting from disease. Significant retinal changes were revealed in female carriers of a rare X-linked genetic mutation in the L and M opsin gene array that causes blue cone monochromacy (the loss of all L and M cone function) in affected males. Retinal findings from AO imaging provided insight into the development and function of the carrier retina. Although carriers had visual resolution within the normal range when tested clinically, visual resolution testing in AOSLO revealed significantly reduced visual resolution compared to normal eyes. Resolution testing across the fovea in normal and diseased eyes provided insight into the relationship between cones, ganglion cells and visual resolution across the visual field. Retinal imaging showed that carriers had fairly normal cone topography despite peak cone density that was ~50% lower than normal; showing that cones destined to express a non-functional photopigment degenerated early in development. Drastic reductions in visual resolution across the fovea in the carrier are best explained by ganglion cell loss that resulted from the loss of cones in the carrier. The relationship between resolution and the spatial sampling limit of the carrier cone mosaic was similar to what was predicted for normal eyes, suggesting an organizing principle in the visual system whereby cone density is the primary determinant of the retinal circuitry that governs visual resolution across the visual field. Together, these studies provide an important contribution to the understanding of the limits of human visual resolution.

## TABLE OF CONTENTS

<b>LIST OF FIGURES .....</b>	<b>iii</b>
<b>LIST OF ABBREVIATIONS .....</b>	<b>v</b>
<b>ACKNOWLEDGEMENTS .....</b>	<b>vi</b>
<b>CHAPTER 1: THE LIMITS TO VISUAL RESOLUTION AND THE SAMPLING THEORY OF VISION .....</b>	<b>1</b>
FACTORS INFLUENCING VISUAL RESOLUTION 1.1 .....	1
OPTICAL LIMITS TO VISUAL RESOLUTION 1.2 .....	1
RETINAL LIMITS TO VISUAL RESOLUTION 1.3 .....	3
NEURAL LIMITS TO VISUAL RESOLUTION 1.4 .....	4
THE SAMPLING THEORY OF VISION AND ALIASING IN HUMAN VISION 1.5.....	5
THE AOSLO AS A TOOL TO STUDY THE LIMITS OF VISUAL RESOLUTION 1.6 .....	7
DISSERTATION OVERVIEW 1.7 .....	9
<b>CHAPTER 2 IS VISUAL RESOLUTION WITH ADAPTIVE OPTICS CORRECTION SUSCEPTIBLE TO PERCEPTUAL LEARNING? .....</b>	<b>10</b>
ABSTRACT 2.1 .....	10
INTRODUCTION 2.2 .....	10
METHODS 2.3 .....	12
RESULTS 2.4 .....	15
DISCUSSION 2.5 .....	18
CONCLUSIONS 2.6 .....	22
<b>CHAPTER 3: VISUAL RESOLUTION IN EMMETROPIA AND LOW-MYOPIA AFTER ADAPTIVE OPTICS CORRECTION OF HIGH-ORDER ABERRATIONS.....</b>	<b>23</b>
ABSTRACT 3.1 .....	23
INTRODUCTION 3.2 .....	23
METHODS 3.3 .....	25
RESULTS 3.4 .....	29
DISCUSSION 3.5 .....	32
CONCLUSIONS 3.6 .....	36
<b>CHAPTER 4: THE RELATIONSHIP BETWEEN VISUAL RESOLUTION AND CONE SPACING IN THE HUMAN FOVEA .....</b>	<b>37</b>
ABSTRACT 4.1 .....	37
INTRODUCTION 4.2 .....	37
METHODS 4.3 .....	39
RESULTS 4.4 .....	45
DISCUSSION 4.5 .....	50
CONCLUSIONS 4.6 .....	57
<b>CHAPTER 4: PHOTORECEPTOR DEVELOPMENT, VISUAL RESOLUTION, AND RETINAL ORGANIZATION IN CARRIERS OF BLUE-CONE MONOCHROMACY ...</b>	<b>58</b>
ABSTRACT 5.1 .....	58

INTRODUCTION 5.2 .....	58
METHODS 5.3 .....	62
RESULTS 5.4 .....	68
DISCUSSION 5.5 .....	79
CONCLUSIONS 5.6.....	83
<b>DISSERTATION SUMMARY .....</b>	<b>84</b>
<b>REFERENCES.....</b>	<b>85</b>

## LIST OF FIGURES

### CHAPTER 1

FIGURE 1:	PSF for a perfect diffraction-limited eye as a function of pupil size .....	2
FIGURE 2:	PSF for a real eye as a function of pupil size.....	2

### CHAPTER 2

FIGURE 3:	MAR as a function of time.....	16
FIGURE 4:	Bland-Altman plot shows good agreement between results obtained in each AO condition .....	16
FIGURE 5:	Pre and post training thresholds for the untrained eye.....	17
FIGURE 6:	MAR without AO correction before and after training.....	17
FIGURE 7:	Modulation transfer functions.....	18
FIGURE 8:	Information beyond the Nyquist limit.....	19
FIGURE 9:	The effect of diffraction blur on tumbling Es and truncated square waves .....	20

### CHAPTER 3

FIGURE 10:	Spherical equivalent refractive error as a function of axial length.....	27
FIGURE 11:	Raw MAR for the myopic group.....	29
FIGURE 12:	Raw MAR for the emmetropic group .....	29
FIGURE 13:	Spectacle magnification adjusted AO corrected MAR.....	30
FIGURE 14:	Critical feature of the Snellen E .....	30
FIGURE 15:	AO corrected critical feature size .....	31
FIGURE 16:	Modulation transfer functions .....	31
FIGURE 17:	Zernike modes 3-21 without AO-correction .....	32
FIGURE 18:	Zernike modes 3-21 with AO-correction.....	32
FIGURE 19:	PSFs and convolved Snellen E's for subject M10.....	33
FIGURE 20:	Wavefront aberrations under each condition for subject M10 .....	34
FIGURE 21:	MTF before and after AO correction for subject M10 .....	34
FIGURE 22:	PTF before and after AO correction for subject M10 .....	34

### CHAPTER 4

FIGURE 23:	Cone positions are triangulated to find cone neighbors for spacing and regularity measurements .....	41
FIGURE 24:	Model of cone apertures .....	44
FIGURE 25:	Stimulus modeling.....	44
FIGURE 26:	Cone stimulation map for subjects S1, S2, S3 & S5 .....	46
FIGURE 27:	Cone stimulation map for subject S4.....	47
FIGURE 28:	Visual resolution and the Nyquist limit of the cone mosaic.....	48
FIGURE 29:	Mosaic regularity .....	48
FIGURE 30:	Visual resolution matches the Nyquist limit of the mRGC mosaic, not the cone Nyquist limit.....	49
FIGURE 31:	Bland-Altman Plot shows poor agreement between MAR and $N_c$ .....	50
FIGURE 32:	Cone stimulation patterns of threshold sized stimuli for subjects S1, S2, S3 & S5.....	51
FIGURE 33:	Cone stimulation patterns of threshold sized stimuli for subject S4 .....	52

FIGURE 34: Tumbling-E resolution measurements matched results obtained with laser interferometry .....	53
--	----

## CHAPTER 5

FIGURE 35: TCA measurement.....	65
FIGURE 36: Appearance of carrier cone mosaic .....	68
FIGURE 37: Comparison of retinal images from different AO imaging systems.....	69
FIGURE 38: Full comparison of 1° location from different AO imaging systems .....	70
FIGURE 39: Cone density along the horizontal meridian .....	71
FIGURE 40: Percentage of cones having 6 neighbors.....	72
FIGURE 41: Voronoi diagrams .....	73
FIGURE 42: Fixation stability at resolution test locations .....	74
FIGURE 43: Fixational stability when observers looked at the stimulus or fixation target.....	74
FIGURE 44:	
a) Nyquist limit of the cone mosaic ( $N_c$ )	
b) Visual resolution (MAR) as a function of eccentricity.....	75
FIGURE 45: Retinal imagery overlaid with contour lines showing stimulated cones .....	76
FIGURE 46:	
a) MAR is worse than predicted by the Nyquist limit of the cone mosaic outside the PRLF	
b) Nyquist limit of the normal eye's mRGC mosaic does not predict resolution outside the PRLF for BCM carriers .....	77
FIGURE 47: More cones are required to see the stimulus at locations outside the PRLF .....	78
FIGURE 48: BCM carriers and normal observers have a similar relationship between MAR and $N_c$ .....	82

## LIST OF ABBREVIATIONS

AO:	adaptive optics
AOSLO:	adaptive optics scanning laser ophthalmoscopy (or ophthalmoscope)
BCM:	blue-cone monochromacy
CFS:	critical feature size
cpd:	cycles per degree
CRT:	cathode ray tube
CSF:	contrast sensitivity function
D <sub>m<sub>gcrf</sub></sub> :	midget ganglion cell receptive field density
DM:	deformable mirror
E <sub>2c</sub> :	eccentricity at which the cone Nyquist limit doubles
E <sub>2m</sub> :	eccentricity at which the MAR doubles
ERG:	electroretinogram
FFT:	fast Fourier transform
GUI:	graphical user interface
ICD:	center-to-center inter-cone distance
LCA:	longitudinal chromatic aberration
LCR:	locus control region
LGN:	lateral geniculate nucleus
MAR:	minimum angle of resolution
MEMS:	microelectromechanical systems
mRGC:	midget retinal ganglion cell
MSC:	map seeking circuit
MTF:	modulation transfer function
N <sub>c</sub> :	Nyquist limit of the cone photoreceptor mosaic
N <sub>mRGC</sub> :	Nyquist limit of the midget retinal ganglion cell mosaic
OTF:	optical transfer function
PRLF:	preferred retinal locus of fixation
PTF:	phase transfer function
RGC:	retinal ganglion cell
RMS:	root mean square
SHWS:	Shack-Hartmann wavefront sensor
TCA:	transverse chromatic aberration
V1:	primary visual cortex

## **ACKNOWLEDGEMENTS**

First of all I want to thank my family for all of their support and encouragement. In particular, my sister Jessica, who always believed in me and was there for me whenever I needed her. My parents, without whose support I never would have made it this far. My grandparents, Louis and Arlene Rossi, for their encouragement and for teaching me the value of hard work. All of my friends, especially Brock, that have stuck with me through the good times and bad times. And finally, Mary, whose love and support helped tremendously to get me through these past two years.

I am grateful to all of the people that have contributed to my professional growth. Walter Makous, who first introduced me to psychophysics and gave me my first experience in vision research. Joel M. Miller, for taking a chance on a long-hair fresh out of college and giving me my first real job in vision science; for the countless things he taught me and for encouraging me to apply to the Vision Science graduate program at Berkeley. Austin Roorda, who has been instrumental in my growth as a graduate student and vision scientist. All of the many Roorda lab people that I have had the pleasure of working with over the years, especially Siddarth, Pavan and Kate. All of the scientists that I have collaborated with, especially Joe Carroll, without whom the final chapter of this dissertation would not have been possible. And a special thanks to my qualifying exam and dissertation committee members, especially Gerald Westheimer, for the many conversations we had regarding this work.

## **Chapter 1**

### **The Limits to Visual Resolution and the Sampling Theory of Vision**

#### **1.1 Factors Influencing Visual Resolution**

Visual resolution can be considered to be constrained by the information loss or ambiguity introduced at each stage in the visual process, as each imposes different limits on the information that reaches the next level of processing and ultimately the information that reaches the highest visual areas of the cortex. The information received by the eye and that is transmitted to subsequent stages of visual processing is governed in part by the laws of physics that describe the propagation and imaging of light and in part by the precision of the biological structures that optimize performance within these limits (Westheimer, 2006). The broad categories that define the limits of vision can be considered to be: 1) optical 2) retinal and 3) cortical. These categories are an oversimplification as there is overlap between them all, but they provide a framework for addressing the loss of information or ambiguities introduced at each stage in visual processing. Understanding the constraints imposed by different stages of visual processing on the performance of the visual system as a whole can provide insight not only into the normal structure and function of the visual system but can help to understand disruptions in visual function resulting from disease. Conversely, changes in visual function with disease can provide insight into the organization and function of the normal visual system. The process of visual perception begins with the light incident on the cornea of the eye which proceeds through the eyes optics to form the electromagnetic disturbance at the retina, the proximal stimulus from which all visual abilities fundamentally arise.

#### **1.2 Optical Limits to Visual Resolution**

The optical quality of the retinal image depends on diffraction, aberrations in the optical components of the eye, transmission and scatter in the optical media, and upon the optical properties of the retina itself (Artal, Benito, & Tabernero, 2006; Campbell & Green, 1965; Enoch, 1963; Porter, Guirao, Cox, & Williams, 2001; Roorda & Williams, 2002a; Roorda & Glasser, 2004; Westheimer, 2006; Williams & Hofer, 2004). Geometrical optics is quite sufficient for describing many important aspects of the retinal image, such as the refractive and accommodative state of the eye and the positions and sizes of objects (Westheimer, 2006). However, Fourier optics is required to accurately describe the effects of diffraction and aberrations on the retinal image (Goodman, 1968; Packer & Williams, 2003; Williams et al., 2004). For a perfect (diffraction limited) eye, a distant point of light will form planar wavefronts incident at the cornea which will be converted to spherical wavefronts by the cornea and lens and form a compact light distribution focused on the retina (Westheimer, 2006; Williams et al., 2004). However, imperfections present in the optical elements of the eye never allow it to act as a diffraction limited system when the pupil is large.

The subjective effect of these aberrations was recognized by Helmholtz who noted that a point of light did not appear as a small circle to him (as he would have expected based upon the case of an out of focus telescope) but rather as a star shaped spot (Helmholtz, 1962). One can visualize their own point spread function by looking at a bright star in the night sky and experience the same subjective effect of the aberrations of the eye as was recognized by Helmholtz. Although several methods had been developed to examine the aberrations of the eye since the time of Helmholtz (Artal, Santamaría, & Bescós, 1988; Campbell, Harrison, & Simonet, 1990; Hartmann, 1900; Howland & Howland, 1976; Howland & Howland, 1977;



**Figure 1| PSF for a perfect diffraction-limited eye as a function of pupil size.** The size of the point spread function is inversely related to pupil size for a perfect diffraction limited eye.

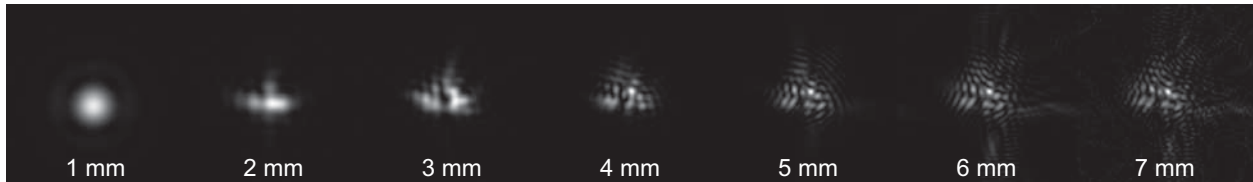


**Figure 2| PSF for a real eye as a function of pupil size.** In the real eye the effect of aberrations on optical quality increases with pupil size. When the pupil is small, the blur from diffraction dominates, but when the pupil is large the blur from aberrations dominates.

Howland, 2000; Rosenblum & Christensen, 1976; Tscherning, 1894; Walsh, Charman, & Howland, 1984), it was not until after the application of Shack-Hartmann wavefront sensing to the human eye by Liang that the objective measurement of the wavefront aberration of the eye became fast and easy enough to become routine (Liang, Grimm, Goelz, & Bille, 1994). The source of most of the aberrations in the eye are imperfections in the cornea and lens (Roorda et al., 2004), with the lens tending to compensate for some of the corneal aberrations, such that the entire eye attains higher optical quality than either element on its own (Artal et al., 2006).

The wavefront aberration of the eye is usually expressed as its difference (in  $\mu\text{m}$ ) from a perfectly flat wavefront. It has become commonplace and convenient in vision science to decompose the wave aberration into component aberrations using the Zernike decomposition (Williams et al., 2004). It has been shown that the low order aberrations of defocus and astigmatism have the largest magnitude in normal eyes; the first three Zernike modes (defocus and the astigmatisms) accounted for 92% of the total variance of the wave aberration in a population of 109 normal humans examined by Porter and colleagues (Porter et al., 2001). These low order aberrations are commonly corrected with spectacle or contact lenses. However, it is well known that many monochromatic aberrations exist in the normal eye beyond just defocus and astigmatism (Artal et al., 1988; Howland et al., 1976; Howland et al., 1977; Liang et al., 1994; Liang, Williams, & Miller, 1997; Packer et al., 2003; Porter et al., 2001; Walsh et al., 1984; Williams et al., 2004).

When the wavefront aberration and pupil size of the eye are precisely measured it is possible to compute the point spread function (PSF) of the eye. The PSF describes the distribution of light in the retinal image for a distant point of light and provides a complete description of image quality at a given retinal location for a given wavelength of light (Williams et al., 2004). The size of the PSF is inversely related to the size of the pupil. Blur due to diffraction alone is greatest when the pupil is small (this is illustrated in Figure 1, which shows diffraction-limited PSFs for a range of pupil sizes). For the normal eye, blur from diffraction dominates when the PSF is small, but when the PSF is large the blur from ocular aberrations dominates (this is shown in Figure 2). When the PSF of the eye is known the retinal image of any object may be computed (Williams et al., 2004). The optical transfer function (OTF) of the eye can be calculated by taking the Fourier transform of the PSF. The OTF is complex,

consisting of two parts, the modulation transfer function (MTF) and the phase transfer function (PTF). The MTF describes how the amplitude of different spatial frequencies is modulated by the optics of the eye, while the PTF describes the phase shifts that occur for different spatial frequencies (for images composed of multiple spatial frequencies). The PTF will be non-zero and phase shifts will occur when the pupil is large and there are asymmetric aberrations in the optics of the eye (Charman & Walsh, 1985; Williams et al., 2004). It is well known that for complex imagery, such as natural images, which are composed of multiple spatial frequencies, the visual consequence of disruptions of spatial phase relationships (ie. the PTF) is more important for visual perception than is the modulation of amplitude (ie. the MTF), although the latter has been the focus of much more study because of its accessibility to measurement prior to wavefront sensing (Campbell et al., 1965; Campbell & Robson, 1968; Charman et al., 1985; Piotrowski & Campbell, 1982; Sarver & Applegate, 2004).

When wavefront sensing is combined with wavefront control, the result is adaptive optics (AO), which has given vision researchers unprecedented control over the optical image on the retina (Liang et al., 1997). This control over the retinal image has allowed for the performance of the visual system to be measured unobstructed by the limitations usually imposed by the imperfect optics of the eye (Liang et al., 1997). This decoupling of the optical image from later neural processing, by using prior knowledge of optical factors, provides the critical description of the proximal stimulus (the retinal image) that is needed to probe the retinal and neural limits to vision (Westheimer, 2006). After the optics of the eye, the primary factors to consider, which limit the information available to the cortex, are sampling of the retinal image by the photoreceptor mosaic and neural circuitry in the retina.

### 1.3 Retinal Limits to Visual Resolution

The photoreceptor mosaic has the highest density of cones at the foveal center; density falls off rapidly with eccentricity (Chui, Song, & Burns, 2008; Curcio, Sloan, Packer, Hendrickson, & Kalina, 1987; Curcio et al., 1990b; Østerberg, 1935). Visual resolution and contrast sensitivity also fall off rapidly with eccentricity (DeValois & DeValois, 1988; Enoch et al., 1973; Green, 1970; Ludvigh, 1941; Marcos & Navarro, 1997; Merigan & Katz, 1990; Weiskrantz & Cowey, 1963; Wertheim, 1894; Westheimer, 1982; Weymouth, Hines, Acres, Raaf, & Wheeler, 1928; Weymouth, 1958) as does the perception of spatial form (Saarinen, Rovamo, & Virsu, 1989) and spatial phase relationships (Rentschler & Treutwein, 1985). Cone density is inversely proportional to cone spacing, which increases with retinal eccentricity; increased cone spacing reduces the spatial sampling capabilities of the retina reducing the instantaneous information available to postreceptoral stages of visual processing. In addition to photoreceptor spacing, the spatial arrangement of photoreceptors is an important retinal factor that forms a constraint on postreceptoral information. The photoreceptor mosaic is often considered to be arranged in a triangular lattice pattern (Curcio et al., 1987; Curcio et al., 1990b; Snyder & Miller, 1977), however, there is disorder in the cone mosaic which varies with retinal location and has important implications for its sampling characteristics (Ahumada & Poirson, 1987; Curcio & Sloan, 1992; Hirsch & Hylton, 1984; Hirsch & Miller, 1987; Yellott, 1982; Yellott, 1983).

Due to the Stiles-Crawford effect, the quantum efficiency of the retina depends on the entry point of light in the pupil (Stiles & Crawford, 1933). This is a consequence of the waveguide nature of the cones and their angular alignment towards the center of the pupil (Enoch, 1963; Roorda et al., 2002a; Williams et al., 2004). The cone photoreceptor acts like an

antenna to funnel light to the photopigment of the outer segment (Enoch, 1963; Williams et al., 2004). Light is absorbed by the photopigment molecules in the outer segment of the cone, which generates an electrical neural signal in the form of hyperpolarization of the cell membrane (Tomita, 1970; Yau, 1994). This signal influences postreceptoral neurons in the retina by modulating the rate of neurotransmitter release from the synaptic terminal of the cone, which is high in the dark and is reduced in a graded fashion by light (Yau, 1994). It has been shown that even at the cone level there is evidence of a loss in spatial resolution as this electrical signal spreads out to adjacent cones due to electrical coupling between cones at gap junctions (DeVries, Qi, Makous, & Sterling, 2002).

Beyond the level of the cones, the diverse retinal circuitry shapes the signal that ultimately reaches the retinal ganglion cells (RGCs), the output cells of the retina. The retinal circuitry that is believed to be most important for visual resolution is the so-called “private-line” path from the cone photoreceptor to the midget bipolar cell to the midget retinal ganglion cell (mRGC) (Polyak, 1941). It is this pathway that is thought to convey fine spatial information to later stages of neural processing; this retinal circuitry changes rapidly with eccentricity from the foveal center and is governed by the relationship between the densities of and connectivity between cones and mRGCs across the retina (Curcio & Allen, 1990a; Dacey, 1993; Drasdo et al., 2007; Kolb, 1970; Kolb & Marshak, 2003). This circuitry mediates the structure of mRGC receptive fields. The organization of the mRGC receptive field ultimately governs the spatial resolving capacity of the retina (McMahon, Lankheet, Lennie, & Williams, 2000; Sincich, Zhang, Tiruveedhula, Horton, & Roorda, 2009).

#### 1.4 Neural Limits to Visual Resolution

Axons from mRGCs terminate in the parvocellular layers of the lateral geniculate nucleus (LGN) (DeValois et al., 1988). LGN neurons are arranged retinotopically; the receptive fields of LGN neurons are monocular (DeValois et al., 1988). The LGN was long considered simply a waystation for signals on their way to the visual cortex, but recent evidence suggests a more prominent role for the LGN in modulating visual attention and awareness (Kastner, Schneider, & Wunderlich, 2006). It has been shown that some LGN cells have receptive field centers fed by single cones (Derrington & Lennie, 1984; McMahon et al., 2000; Sincich et al., 2009); this structure is necessary to retain fine spatial information at the level of the LGN. Recent work has shown that it is now possible to use adaptive optics imaging combined with single unit recording from cells in the LGN to map single cone input to LGN receptive fields; this advancement should provide needed insight into how signals from single cones influence the response properties of LGN neurons (Sincich et al., 2009).

Signals from the LGN are then sent to the primary visual cortex (V1), which contains a map of visual space; each location in the visual field is represented by a single physical location in V1 (Hubel & Wiesel, 1974; Shira, Wade, & Tyler, 2007). This representation of visual space in the cortex is not uniform, with an overwhelming proportion of cortical area devoted to the central visual field, specifically the fovea. This “cortical magnification” describes the areal magnification in cortical representation of visual space with respect to eccentricity and has been the focus of a significant amount of study (Azzopardi & Cowey, 1993; Cowey & Rolls, 1974; Drasdo, 1977; Duncan & Boynton, 2003; Rovamo, Virsu, & Näsänen, 1978; Rovamo & Virsu, 1979; Shira et al., 2007; Virsu & Rovamo, 1979; Wässle, Grünert, Röhrenbeck, & Boycott, 1989; Wässle, Grünert, Röhrenbeck, & Boycott, 1990). Cortical magnification has been shown to be correlated with ganglion cell density (Wässle et al., 1989; Wässle et al., 1990), visual

acuity, contrast sensitivity (Duncan et al., 2003; Rovamo et al., 1978; Virsu et al., 1979), and hyperacuity (Yap, Levi, & Klein, 1987). Beyond the sheer amount of cortex devoted to different parts of the visual field, an important consideration is the spatial frequency response of cortical neurons and specifically their sensitivity to the highest spatial frequencies, for it is upon this factor that visual resolution must ultimately depend.

According to the Fourier theory of vision, there exist within the visual system quasi-linearly operating independent mechanisms (channels) that are selectively sensitive to a limited range of spatial frequencies (Campbell et al., 1968). There is overwhelming evidence that the constituent elements of these channels are neurons located in V1, which are tuned to specific bands of spatial frequencies (DeValois et al., 1988). Although much has been discovered about the properties of cortical neurons, it is not well known what the finest grain is at which vision is represented in the cortex. The highest spatial frequencies to which these neurons respond should be set by the spacing between foveal cones, which for the most closely spaced cones in the center of the fovea (~0.5 arcmin) would correspond to a spatial frequency of approximately 60 cycles per degree. However, due to the technically challenging nature of the task of mapping receptive fields in V1, no evidence yet exists of cortical receptive fields fed by single cones (Smallman, MacLeod, He, & Kentridge, 1996). Furthermore, there is no physiological evidence of neurons in V1 that are tuned to very high spatial frequencies, with the highest reported preferred center spatial frequencies in the literature being 16 cycles per degree for the macaque (DeValois, Albrecht, & Thorell, 1982) and 24 cycles per degree for the vervet monkey (Parker & Hawken, 1985). However, there is psychophysical evidence that these high spatial frequency channels do exist and that there are receptive fields that are so small as to be fed by a single cone (Smallman et al., 1996).

Although there is psychophysical evidence to suggest that these high spatial frequency channels do exist in some individuals, it is certainly not well known if all persons will possess them and therefore have the ability to see the highest spatial frequencies. The development of these channels may be stimulus driven and rest upon the ability of the optical and retinal stages of vision to: 1) produce a retinal image containing high spatial frequency information, 2) sample this image efficiently by the photoreceptors in the retina, and 3) convey this information, without significant loss in the many intermediate processing stages, to the cortex. This ability would be influenced by factors already considered, such as the optical quality of the retinal image, and the sampling characteristics of the retina, of which there is evidence of wide variability in the normal population (Curcio et al., 1990b; Porter et al., 2001). The case of uncorrected refractive error is one that might be a simple case to consider from an optical standpoint: if an in-focus image is never presented to the retina, will the visual system develop the mechanisms required to make use of high spatial frequency information?

## 1.5 The Sampling Theory of Visual Resolution and Aliasing in Human Vision

The fact that sampling by the receptive elements in the eye provides a limit to the information available at post receptoral stages of visual processing has been recognized since the second half of the 19<sup>th</sup> century. During this time, the work of Bergmann and the work of Helmholtz formed the foundation of what is now known as the sampling theory of visual resolution (D'Zmura, 1996; Helmholtz, 1962; Thibos, 2000). According to Helmholtz's formulation of this theory: "two bright points in space cannot be resolved as separate unless the distance between their images on the retina are greater than the diameter of a single receptive element" (Helmholtz, 1962). He correctly proposed that this receptive element was the cone

photoreceptor (it was still a matter of contention at the time as to whether or not the rod was also a photoreceptor). He went on to further explain that: “The distance separating the images must be greater than the width of a single receptive element if the two images are to fall on two different and non-contiguous elements, with another element in between them that is not stimulated by light at all, or at least is less stimulated than the others.” (Helmholtz, 1962). The modern formulation of this theory has been distilled into a single sentence: “for two points to be discriminated, at least one relatively unstimulated photoreceptor must lie between two relatively stimulated photoreceptors” (Thibos, 2000). This is sometimes referred to as Helmholtz’s rule, or the Bergmann-Helmholtz rule; the simplicity and logic underlying it is undeniable.

Students of information theory will recognize the Bergmann-Helmholtz rule as the Nyquist-Shannon sampling theorem, which was described in a more mathematical way by Shannon: “If a function  $f(t)$  contains no frequencies higher than  $W$  cycles/second, it is completely determined by giving its ordinates at a series of points spaced  $1/2W$  seconds apart” (Nyquist, 1928; Shannon, 1949). So, to efficiently sample a continuous signal, one must have at least twice as many samples as the maximum frequency present in that signal. This minimum sampling frequency is called the Nyquist frequency, the inverse of which in spatial coordinates is the Nyquist limit. Although sampling in the eye by the photoreceptor mosaic is a complex two-dimensional process of sampling by a hexagonal array (Mersereau, 1979), to the first order, this limit can be considered to be the Nyquist sampling limit of the cone mosaic ( $N_c$ ). Sampling below the Nyquist frequency results in aliasing. Aliasing is the appearance of spurious low spatial frequencies in a sampled signal due to under sampling of high frequencies (Williams, 1985a).

Helmholtz formulated his sampling theory of visual resolution based upon a thought experiment involving an idealized two point resolution task; however, nearly all of the data to support the theory comes from modern experiments that employed grating stimuli (Williams, 1985a; Williams, 1985b). The observation of aliasing by observers viewing high spatial frequency gratings continues to be the most compelling evidence to support the sampling theory of visual resolution (Byram, 1944; D'Zmura, 1996; Helmholtz, 1962; Williams, 1985a; Williams, 1985b). Both Bergmann and Helmholtz each described seeing distortions consistent with aliasing when viewing high spatial frequency gratings (D'Zmura, 1996; Helmholtz, 1962). In his classic treatise on physiological optics, Helmholtz provided an illustration very similar to those later created by Byram and Williams, showing the subjective perception of aliasing (Byram, 1944; Helmholtz, 1962; Williams, 1985a). Multiple observers in Bergmann's study reported that a grating stimulus viewed from a distance frequently appeared checkered or mottled (D'Zmura, 1996). The optical quality of the eyes of Bergmann's subjects must have been exceptionally high because normally the optics of the eye limit the contrast of high spatial frequencies, a mechanism which should prevent aliasing (Campbell et al., 1965). However, it is likely that Bergmann was the first to report true aliasing in the eye as he noted two specific consequences of aliasing that have been reported in more recent studies by researchers employing interference fringe stimuli: the orientation reversal effect, and the instability of the aliased percept.

Bergmann reported that the “illusion” frequently took on the orientation exactly perpendicular to the orientation of the actual stripes (D'Zmura, 1996). This is the orientation reversal effect that Coletta and Williams reported when viewing interference fringes in the parafovea, and that they used to estimate the Nyquist limit of the parafoveal cone photoreceptor mosaic (Coletta & Williams, 1987). They found that near to, but outside the fovea, interference fringes at spatial frequencies higher than the resolution limit look like two-dimensional spatial

noise, but that over a limited range of high spatial frequencies this noise takes on a striated appearance, with the striations running perpendicular to the true fringe orientation (Coletta et al., 1987). Bergmann also noted that “The faulty perceptions of stripes, just like the correct perceptions made at the greatest distances, are stable only for very short periods. Their disappearance is presumably due … perhaps to the fact that the image of the grating on a group of cones that provides either the false or the veridical perception shifts in position to another group that does not do this.”(D’Zmura, 1996). Williams gave a similar description and probable cause of the instability of the aliasing percept: “The observed mottled pattern changes rapidly over time, presumably as eye movements shift the retina relative to the image.” (Williams & Collier, 1983).

Although Bergmann and Helmholtz laid a solid foundation for the sampling theory of vision with their work, the best evidence to support and validate it has come from 20<sup>th</sup> century researchers who developed advanced stimulus delivery techniques and experimental methods. In 1935 Le Grand introduced the method of interferometry to produce high contrast interference fringes on the retina (Charman & Simonet, 1997). This technique allowed for the resolving capacity of the retina to be examined unrestricted by the limitations of both diffraction and the imperfect optics of the human eye (Charman et al., 1997; Byram, 1944; Westheimer, 1960; Campbell et al., 1965). Interference fringe stimuli continue to be an important tool for examining the performance of the human visual system unconstrained by the limitations of the optics of the eye, and have been utilized by many researchers (Byram, 1944; Campbell et al., 1965; Charman et al., 1997; Coletta & Watson, 2006; Green, 1970; Westheimer, 1960; Williams et al., 1983; Williams, 1985b; Williams, 1985a; Williams & Coletta, 1987). This technique has been very successful; among numerous other applications, it has been applied to: estimating the contrast transfer function of the human eye (Campbell et al., 1965), determining the absolute contrast sensitivity of the neural visual system (Williams, 1985b), and estimating the topography of the foveal cone mosaic (Williams, 1988). However, this method has limitations, in that it can only be used to project gratings onto the retina, not complex imagery such as natural scenes or complex patterns commonly used to test visual resolution.

## 1.6 The AOSLO as a Tool to Study the Limits of Visual Resolution

Since the invention of the scanning laser ophthalmoscope (SLO), modulation of the scanning laser beam to project complex patterns onto the retina and simultaneously record retinal images has found many applications. It has been applied to locating scotomas with microperimetry, finding the preferred retinal locus of fixation (PRLF) in eyes with central scotomas, measuring visual acuity and visual function, and for examining fixational dynamics during reading and in patients with retinal pathology (Guez et al., 1998; Le Gargasson, Rigaudiere, Guez, Schmitt, & Grall, 1992; Mainster, Timberlake, Webb, & Hughes, 1982; Timberlake, Mainster, Webb, Hughes, & Tempe, 1982; Timberlake et al., 1986; Webb, Hughes, & Pomerantzeff, 1980). However, technical limitations of the traditional SLO, including its wide scan field and low resolution have limited its usefulness for certain applications, such as probing the fine structure of the retina and for delivering photoreceptor scale stimuli to the retina. The adaptive optics scanning laser ophthalmoscope (AOSLO) overcomes many of these limitations (Roorda et al., 2002b).

AO correction of the eyes optical aberrations in the AOSLO not only allows for much higher resolution imaging of the retina than conventional SLO, but also for the delivery of ultra-sharp photoreceptor scale complex stimuli (Poonja, Patel, Henry, & Roorda, 2005; Roorda et al.,

2002b). Visual stimulus delivery in the AOSLO allows for the display of static images and also for presentation of dynamic imagery, such as videos or animations. With recent software and hardware innovations, this has become almost as simple as presenting them on a CRT (Poonja et al., 2005). The AOSLO brings a great advantage to psychophysics because of its ability to present complex stimuli to the retina that are of higher optical quality than the visual system has ever experienced while simultaneously imaging the underlying cone photoreceptor mosaic. This feature provides the technological capacity required to appropriately test the sampling theory of vision. An important goal in vision science has been to discern the relationship between the physical object (the distal stimulus), the retinal image (the proximal stimulus), the pattern of retinal stimulation at the level of the photoreceptors, the neural processing mechanisms of the both retina and cortex, and finally perception (Westheimer, 2006). The AOSLO is a powerful tool for vision scientists to use to realize this goal.

With the development of AO systems, researchers have examined the improvement in contrast sensitivity and visual resolution afforded by directly measuring the eyes high order aberrations with a wavefront sensor and correcting them with either a deformable mirror (Liang et al., 1997; Poonja et al., 2005; Williams et al., 2000; Yoon & Williams, 2002), a phase plate (Yoon, Jeong, Cox, & Williams, 2004), or a spatial light modulator (Fernández, Prieto, & Artal, 2009). The amount of high order aberrations that can be corrected varies as a function of pupil size, with the biggest pupils having the greatest potential for large improvements in optical quality. This is because the magnitude of high order aberrations increases and the blur from diffraction decreases with increasing pupil size (as shown in Figure 2). When the pupil is small (~3mm) diffraction dominates and monochromatic aberrations beyond defocus and astigmatism are less of a factor (Liang et al., 1997). Theoretically, those eyes that naturally have more high-order aberrations should benefit the most from AO correction (Liang et al., 1997). The contrast sensitivity improvement for normal healthy eyes has been shown to be quite substantial, affording a 6 fold increase in sensitivity at 27.5 cycles per degree (cpd) and allowing for the detection of very high spatial frequency gratings at 55 cpd, which were imperceptible while viewing through the eyes normal optics (Liang et al., 1997).

Improvements have also been seen in visual resolution, but they have not been shown to be as great as the improvements in contrast sensitivity (Yoon et al., 2004; Yoon et al., 2002). Yoon and Williams reported a 1.6 fold improvement in visual resolution (a 37.5% reduction in the minimum angle of resolution (MAR)) after correcting for both monochromatic and chromatic aberrations in 7 eyes (Yoon et al., 2002). Poonja et al. showed an average reduction in the MAR of 33% for 6 eyes after adaptive optics correction in AOSLO (Poonja et al., 2005). Visual resolution and contrast sensitivity are, of course, not directly comparable, as benefits at a particular low spatial frequency may not result in improvements in a resolution task. This would depend upon the spatial frequency content of the resolution stimulus and whether an observer used the information at that particular spatial frequency for making their decision in that resolution task. However, the high spatial frequency cutoff of the contrast sensitivity function (CSF) (usually only detectable at 100% contrast) is often considered to be the grating acuity limit (expressed in MAR) (Thorn & Schwartz, 1990). Previous studies that looked at the improvement in contrast sensitivity after AO correction did not measure contrast sensitivity out to the high spatial frequency cutoff. Liang et al. approached it by measuring out to 55 cpd, but Yoon and Williams only tested out to 32 cpd (Liang et al., 1997; Yoon et al., 2002). If they had, it is likely that they would have found a higher spatial frequency cutoff after adaptive optics correction than before, as was shown by Liang et al. (Liang et al., 1997).

The more modest improvements found in visual resolution after AO correction may also be due to the fact that resolution measurements obtained with letter stimuli are more sensitive than grating acuity to changes in resolution resulting from blur (Green & Campbell, 1965; Hirsch, 1945; Radhakrishnan, Pardhan, Calver, & O'Leary, 2004a; Strang, Winn, & Bradley, 1998; Thorn et al., 1990). Any residual aberrations in the eye or instrument that caused retinal image blur would therefore affect visual resolution measurements more than contrast sensitivity measurements. This is especially likely, considering that visual resolution is generally tested clinically with letter stimuli that have broad spatial frequency content and that blur is more likely to affect higher spatial frequencies to a greater extent than lower spatial frequencies. In addition, any residual aberrations causing phase distortions would disrupt the phase relationships between the individual spatial frequency components of a complex stimulus, whereas a grating of a single spatial frequency would only be displaced.

## **1.7 Dissertation overview**

The experiments presented in this dissertation address the limits of visual resolution as broadly outlined in this introduction. As insight into the function of the normal visual system is often found by examining how it is disrupted in disease, both normal and diseased eyes were examined. In Chapter 2, a perceptual learning paradigm is implemented in AOSLO to examine the role that both optical and neural factors play in limiting visual resolution. Chapter 3 examines visual resolution when disease disrupts the optics of the eye in myopia. This experiment addresses all three categories by examining whether the resolution deficit seen in myopia is due to optical aberrations, or if retinal and neural changes in myopia cause the visual deficit. Chapter 4 finally puts the sampling theory of vision to the test, by simultaneously measuring visual resolution and the sampling characteristics of the retina across the fovea. This study combines for the first time both high quality measurements of the sampling limit of the retina with optically optimal measurements of visual resolution in the same eyes. Chapter 5 examines visual resolution across the fovea in female carriers of a rare genetic mutation affecting the cone photoreceptor. This study provides information not only about visual structure and function in this rare condition but also fascinating insight into the development, organization and function of the normal visual system.

## **Chapter 2**

### **Is visual resolution with adaptive optics correction susceptible to perceptual learning?**

#### **2.1 Abstract**

Recent research suggests that the visual benefit of correction of high order aberrations might not be fully realized due to neural mechanisms that naturally compensate for the aberrations of the eye (Artal et al., 2004). The purpose of this experiment was to measure the extent to which these neural mechanisms might be susceptible to perceptual learning in an AO corrected test of visual resolution. The AOSLO was used to project a high contrast AO–corrected stimulus onto the retina of four observers (three emmetropes and one myope). Visual resolution was measured using a four alternative forced choice tumbling E test in the following conditions: 1) spectacle correction without AO 2) 3 mm pupil with AO correction and 3) 5.81 mm pupil with AO correction. Prior to training, measurements were made on both eyes in all three conditions.

Subjects then underwent training with one eye in both AO corrected conditions over a period of five consecutive days. Post-training measurements were then made again in both eyes under all three conditions. The range of measured acuities in minimum angle of resolution (MAR) for the three conditions were as follows: 1) spectacle correction without AO: 0.52–0.94 arcmin 2) 3 mm pupil with AO: 0.33 to 0.59 arcmin and 3) 5.81 mm pupil with AO: 0.35 to 0.59 arcmin. AO correction of ocular aberrations allowed all observers to achieve an immediate and significant increase in resolution. The three emmetropic observers consistently achieved acuities below 0.4 arcmin (Snellen equivalent of 20/8). Training did not significantly improve performance suggesting that any aberration adaptation mechanism that might exist does not hinder AO correction from providing an immediate visual benefit in this resolution task. There was no significant difference in performance between the 3 mm and 5.81 mm AO conditions.

Measurements of the residual aberrations after AO correction showed that optics were not a limiting factor for either AO condition. Although the 3 mm and 5.81 mm conditions perform similarly, there are likely different optical mechanisms that limit visual resolution in each condition. The 3 mm pupil may be limited primarily by low contrast due to diffraction. For the 5.81 mm pupil, the benefits of higher contrast at lower spatial frequencies are offset by the presence of high spatial frequencies beyond the photoreceptor Nyquist limit, which introduce aliasing distortions.

#### **2.2 Introduction**

##### **2.2.1 Rationale**

It is well known that the optical aberrations of the eye impose a fundamental limit to visual resolution (Campbell et al., 1965). The pattern of ocular aberrations is unique for each individual (Porter et al., 2001), and it has been hypothesized that the visual system may have evolved a neural mechanism to optimize perception by minimizing the effects of these persistent aberrations (Artal et al., 2004). This is supported by the finding that the best subjective image quality is experienced when an observer views a stimulus through an aberration profile that is only partially corrected (Chen, Artal, Gutierrez, & Williams, 2007). This has led to the suggestion that some of the visual benefits of the correction of ocular aberrations may not be realized immediately, or may be undone by the nervous systems compensation for the previous aberration state of the eye (Artal et al., 2004). AO correction of the aberrations of the eye has been shown to improve optical quality both for imaging the retina and for delivering high resolution stimuli (Liang et al., 1997). Combined real-time imaging and stimulus delivery in the

AOSLO has the potential to allow the performance of the visual system to be assessed unobstructed by the limitations imposed by the imperfect optics of the eye. However, the question remains as to whether the adult human visual system can take advantage of the unprecedented image quality that is afforded by AO immediately, or if there is some learning period during which a person needs to adapt to the new pattern of aberrations present while viewing an AO corrected image to obtain the best visual resolution possible. It has previously been shown that a visual benefit can be realized immediately after correction of the eyes high order aberrations, improving visual performance in both contrast sensitivity and visual acuity tasks (Liang et al., 1997; Williams et al., 2000; Yoon, Jeong, Cox, & Williams, 2009; Yoon et al., 2002). However, no study to date has examined whether AO corrected performance on a visual resolution task improves with training, or if performance is different when correcting aberrations over a large or a small pupil.

## 2.2.2 Visual Resolution and Perceptual Learning

The adult human visual system is well known to be plastic from the photoreceptors to the extrastriate visual areas of the cortex; sustained learning effects on visual tasks have been shown to take place after 1-2 hours of training (Fine & Jacobs, 2002). However, performance increases from perceptual learning vary considerably between different visual tasks, with low-level tasks such as foveal resolution showing little or no improvement with training (Fine et al., 2002; Johnson & Leibowitz, 1979; Westheimer, 2001). Determining whether a task can be improved with training can provide insight into the neural stages upon which that task relies (Westheimer, 2001). Westheimer has stated that “It can be argued that where there is no learning the processing is of a more primitive kind, more robust and nearer to sensory organs” (Westheimer, 2001). It is generally accepted that foveal visual resolution in the adult has reached an optimal value, has a strong retinal basis, and depends on the spacing of retinal elements in an elementary way (Westheimer, 2001). However, there is large variability in resolution measurements obtained across observers, even when corrected optically using conventional spectacle lenses, with “normal” visual resolution having a range of 0.5 to 1 arcmin in normal observers (Westheimer, 2003). Much of this variability may be due to the wide variability in optical aberrations and their effect on retinal image quality. Although resolution tasks have been shown to exhibit little or no sustained improvements with training (Fine et al., 2002; Johnson et al., 1979; Westheimer, 2001), it has been shown that there exist neural adaptation mechanisms that minimize the effects of optical blur on perception. These fast-adapting mechanisms work to optimize perception based upon the spatial frequency content of the entire visual scene (Georgeson & Sullivan, 1975; Webster, Georgeson, & Webster, 2002).

Since the resolution task itself should not be expected to show any improvement with training, using a visual resolution task to look for threshold reductions with training may gain insight into any effect that adaptation to optical aberrations have on visual resolution. If the visual system continues to compensate for aberrations that are no longer present after AO correction, this would presumably negatively affect AO corrected visual resolution measures (Artal et al., 2004). If there is some residual compensatory mechanism hindering performance in an AO corrected visual resolution task, there may be some improvement if the person is trained in that task. To test whether or not this is the case, a perceptual learning paradigm was implemented in the AOSLO, whereby vision was initially tested both with and without adaptive optics compensation, followed by five consecutive days of training with explicit feedback and then retested following the training period.

### **2.2.3 AO Correction and Visual Resolution for Different Pupil Sizes: the Role of Information Beyond the Cone Nyquist Limit**

In addition to looking at the ability of the visual system to take advantage of the optical improvement afforded by AO, the effect of correction over different pupil diameters was simultaneously examined. To achieve AO compensation of ocular aberrations in AOSLO, it is necessary to induce mydriasis and cycloplegia with drugs. This allows for measurement and correction of aberrations over a large pupil (improving optical quality both for imaging and delivering stimuli), and removes the dynamic aberration changes that occur with accommodation. Although many observers obtain quite large pupil sizes, the AOLSO system configuration allows a maximum pupil diameter over which those aberrations may be measured and corrected of 5.81 mm. However, the pupil size can be adjusted to be smaller than this maximum diameter. Since optical image quality should increase with increasing pupil size (if optical aberrations are eliminated, see Chapter 1), performance was tested and participants were trained on a visual resolution task while aberrations were corrected over both 3 mm and 5.81 mm pupils. Comparing the differences in improvement afforded by training in each condition provides insight into the information observers use to make a decision in the resolution task. Specific interest is in information above the Nyquist limit of the cone mosaic that is expected to result in aliasing by the photoreceptor mosaic (see Chapter 1). It has been shown that this information can provide a cue to the orientation of a grating, allowing some observers to achieve supra-Nyquist resolution (Williams et al., 1987); AO correction over the larger pupil will introduce spatial frequencies into the eye that are twice as high as those in the smaller pupil, well beyond the theoretical Nyquist limit of the cone mosaic, allowing the role of this information to be assessed in this task. This manipulation will also provide insight into the spatial frequencies that are used to make a decision in the tumbling E visual resolution task.

### **2.2.4 Overview**

The purpose of this study was two-fold: 1) to examine if the benefit afforded by AO correction of optical aberrations improves with training and 2) to assess whether there is a significant benefit achieved of correcting aberrations over a large pupil relative to a small pupil. The visual benefit of training was assessed under two AO-corrected conditions: 1) AO correction over a 3 mm pupil and 2) AO correction over a 5.81 mm pupil. Visual resolution was assessed in both eyes prior to training in the two AO-corrected conditions and also without AO-correction. For the tests done without AO correction, visual resolution was measured with spectacle lens correction only. Each observer was then trained in both AO conditions on five consecutive days. A post-training assessment was conducted on the following day that was identical to the pre-training sessions.

## **2.3 Methods**

### **2.3.1 Subjects**

Four observers participated in this study, three emmetropes (S1-S3) and one myope (S4). Informed consent was obtained from the participants after the nature of the study and possible complications were explained verbally and in writing. This experiment was approved by the University of California, Berkeley Committee for the Protection of Human Subjects. Three of the observers (S1, S3 & S4) had extensive experience in visual psychophysical tasks, while one observer (S2) was naive.

### **2.3.2 Stimulus Presentation & Retinal Imaging in AOSLO**

The AOSLO was used to project a high contrast stimulus onto the retina of each observer. The stimulus (a Snellen E) was scanned onto the retina in a raster fashion with a 658 nm (red) diode laser. Scanning was carried out with a resonant scanner – galvanometric scanner combination (Electro-Optics Products Corp, Flushing Meadows, NY). The beam was scanned at 16 kHz in a sinusoidal pattern by the resonant horizontal scanner, which was coupled to the vertical galvanometric scanner that operated in a sawtooth pattern at 30 Hz. Each frame consisted of 525 horizontal lines. Scan amplitude set the imaging field size and could be adjusted manually to be between 0.5 and 3 degrees. A calibration grid placed at the retinal plane during system setup and calibration allowed field size to be precisely set (Grieve, Tiruveedhula, Zhang, & Roorda, 2006; Poonja et al., 2005; Roorda et al., 2002b).

The field size was set to be 48 arcmin x 60 arcmin, with the center 6 arcmin optimized to be over the most linear portion of the scan. Linearization of the central portion of the scan was accomplished by projecting a checkerboard target of known pixel dimensions onto the calibration grid and setting them to be in register. This resulted in the central 6 x 6 arcmin area being approximately linear. Optimization of the central portion of the raster scan was essential for ensuring that the Snellen E stimulus used for resolution testing was not distorted horizontally, which would have been a cue to stimulus orientation and would have invalidated the resolution measurements.

To produce the Snellen E in the raster scan, the beam was modulated using an acousto-optic modulator, or AOM (Brimrose Corp, Baltimore, MD) that was placed in the path of the beam prior to the entrance pupil of the system. The AOM, under computer control, could be set to deflect the beam into or out of the system, acting essentially as a switch that could turn the beam on or off. The beam was switched on during the forward section of the horizontal scan (because of the sinusoidal nature of the horizontal scanner it scans in both a forward and return path, turning it on only during the forward path limited light exposure) (Poonja et al., 2005). On those lines where the Snellen E was present, the AOM switched the beam off to create the desired stimulus features. The stimulus was presented in Maxwellian view (Westheimer, 1966) and appeared to the observer as black on a bright red background (negative contrast). The Weber contrast was approximately -1. Image quality was not degraded by the frequency response of the AOM because of its very high frequency (up to 50 MHz).

Light that was reflected back out of the eye was de-scanned by the scanning mirrors as it was back reflected along the path of the beam. A small portion of that light was directed via a beamsplitter to a Shack-Hartmann wavefront sensor (SHWS), while the rest passed through and was focused onto a confocal pinhole. The light passing through the pinhole was then detected by a photomultiplier tube (PMT) (H7422-20, Hamamatsu, Japan). The PMT signal was sent to a frame grabber board that built a video image of the retina pixel by pixel. Wavefront compensation was provided by a 37 actuator DM (Xinetics, Andover, MA) placed in the path conjugate to the entrance pupil of the eye prior to scanning. Further details of the AOSLO system and stimulus delivery technique are described in detail elsewhere (Grieve et al., 2006; Poonja et al., 2005; Roorda et al., 2002b).

Mydriasis and cycloplegia were induced with 1 drop of 2.5% phenylephrine and 1 drop of 1% tropicamide ~20 minutes prior to the start of the experimental session, and were maintained throughout with an additional drop, if necessary. Head stabilization was maintained with a dental impression bite bar mounted on an X-Y-Z stage. Ocular aberrations were measured using the AOSLO's SHWS, which had 241 lenslets over a 5.81 mm pupil. A digital CCD

camera detected the focused spots, and aberrations were fit to a 10<sup>th</sup> order Zernike polynomial (Grieve et al., 2006; Roorda et al., 2002b). Low-order aberrations (sphere and astigmatism) were corrected using standard trial lenses placed into the AOSLO system near the spectacle plane (~14mm from the entrance pupil). The RMS error from the SHWS was used to optimize this correction objectively to within 0.1D.

Participants were then subjectively refracted while viewing a static 20/20 Snellen E stimulus through their spectacle correction in the AOSLO system. This was done because 1) RMS wavefront error has been shown to be a poor predictor of subjective image quality (Applegate, Marsack, Ramos, & Sarver, 2003b; Applegate, Ballentine, Gross, Sarver, & Sarver, 2003a; Chen, Singer, Guirao, Porter, & Williams, 2005) and 2) even though the AO system corrects ocular aberrations, it does not necessarily focus the corrected image onto the photoreceptor plane. A fixed defocus level was determined by placing small amounts of defocus onto the deformable mirror and asking the participant to report which looked clearer. If a fixed defocus level was needed, it was placed onto the deformable mirror for the experimental trials. This was done separately for each condition. For the AO conditions, aberrations were corrected through the best spectacle lens correction and a second subjective refraction was performed. Subjects usually did not require any additional defocus.

The laser power varied day-to-day, but was always between 14.6 and 19  $\mu\text{W}$ , with a mean power of 16.42  $\mu\text{W}$ , which corresponded to an average retinal illuminance of 6.5 log Trolands (Wyszecki & Stiles, 1982). Although at this light level the photopigment is nearly 100% bleached, there is no indication that this would hinder the subjects performance (Wyszecki et al., 1982). Subjects adapted quickly to the bright field and had no problem performing the task comfortably. This high retinal illuminance was used so that an image could be obtained of the retina during psychophysical testing. During each psychophysical trial a video of the retina was simultaneously acquired. Videos were acquired to determine the preferred fixation locus and cone spacing of the observer. Under the AO corrected 3 mm pupil condition, an aperture stop in the AOSLO system was manually adjusted to limit the size of the pupil to 3mm; a paper target placed at the pupil plane was used to check pupil size. In the AO corrected 5.81 mm condition, the aperture was opened to allow for AO correction over the full 5.81 mm pupil.

### 2.3.3 Pre- and Post-Training Visual Resolution Measurements

Measurements of visual resolution were obtained for each observer, under each condition, and for both eyes, before the start of training (pre) and after five days of training (post). For the AO corrected conditions, an AO correction was performed at the beginning of each training session and then either: 1) after 35 trials, 2) when the observer noticed that the image quality had degraded or 3) after the experimenter, monitoring AOSLO image quality, determined that the quality of retinal imagery had decreased. Measurements of the residual wavefront aberration were stored to computer for offline analysis at several times throughout the experiment. Both eyes were tested in the pre and post stages to test for interocular transfer of any training effects to the untrained eye.

The method of constant stimuli was employed to measure resolution thresholds. Seven different stimulus sizes were used for each measurement, with the gap in the E, corresponding to the MAR for that letter size ranging from 0.25 arcmin to 1 arcmin in 0.125 arcmin steps (corresponding to Snellen sizes of 20/5 to 20/20 in 2.5 Snellen line steps). In a four alternative forced choice task, observers judged the orientation of the Snellen E by indicating the direction of the parallel strokes of the E relative to the orthogonal stroke (either right, left, up or down).

Stimulus duration was one second (30 frames). The observer initiated each trial with a keypress on a computer keyboard. After a short delay (~200 msec) the stimulus appeared in one of four randomly chosen orientations. The observer then responded with a key press on the arrow keys of a computer keyboard. The experiment was controlled using MATLAB (The MathWorks, Natick, MA, USA) and custom software. The measurement consisted of obtaining 10 orientation judgments for each of the 4 orientations and 7 letter sizes, resulting in 280 stimulus trials per measurement (40 trials of each stimulus size). Data were then fit to a Weibull psychometric function, using MATLAB software, which determined the smallest letter size that the observer could correctly judge the orientation of at the 72.4% correct level. Pre and post-training measurements were identical except for the range of stimuli sizes used. Post-training measurements for all but the non-AO condition of observer 4 used one smaller letter, with the gap in the E being 0.125 arcmin (Snellen equivalent of 20/2.5), corresponding to the range of sizes used for the training session.

### 2.3.4 Training

Each observer spent one hour per day training, with the time split equally between each AO corrected condition (~30 minutes spent on each condition). Training sessions were limited to one hour to minimize the effects of fatigue (Beard, Levi, & Reich, 1995) and carried out over multiple days because of the role of sleep in consolidating learning (Karni, Tanen, Rubenstein, Askenasy, & Sagi, 1994). Training was monocular and condition order was alternated on each day. For five consecutive days, ~500 trials were completed in each condition (~1000 total trials per day), with an approximately equal distribution of letter sizes and orientations chosen from the set of 28 stimuli. The largest letter size used for pre-training threshold measurements (1 arcmin, 20/20 Snellen) was not used in the training sessions because it was found in the pre-training session that all observers could correctly identify that letters orientation after AO correction 100% of the time. Therefore, a smaller letter, with 0.125 gap (20/2.5 Snellen) replaced the 1 arcmin (20/20 Snellen) E for the training sessions. This was done so that training could focus on those letter sizes which might improve with training. For one observer, S4, no training was done on training day 1 in the 3 mm condition due to a software malfunction. During the training sessions, auditory feedback was provided after each trial. Feedback consisted of a computer voice stating either “correct” or “incorrect”, and if the latter, also either “up”, “down”, “left”, or “right”. Feedback was controlled using the same MATLAB software that controlled the experiment. Feedback was given after each trial because it has been shown that stronger learning effects can occur when feedback is given (Fine et al., 2002; Herzog & Fahle, 1997).

## 2.4 Results

MAR is plotted versus day for each AO corrected condition in Figure 3. Observers performed quite well immediately in both conditions; prior to training visual resolution was significantly better in both the 3 mm ( $p = 0.00017$ ; paired t-test) and 6 mm ( $p = 0.0016$ ; paired t-test) AO corrected conditions compared to the no adaptive optics condition for both eyes tested. Interestingly, throughout the course of the experiment, there was never a significant difference between the measurements obtained in either AO condition ( $p = 0.9366$ ; paired t-test). A Bland-Altman analysis confirmed that there was good agreement between the measurements obtained in both AO conditions (Figure 4). Post-training thresholds were lower for 3 of the 4 observers in each AO corrected condition; thresholds were worse in the post training session for S1 in the 3 mm condition and S3 in the 6 mm condition. There was not a significant difference between the

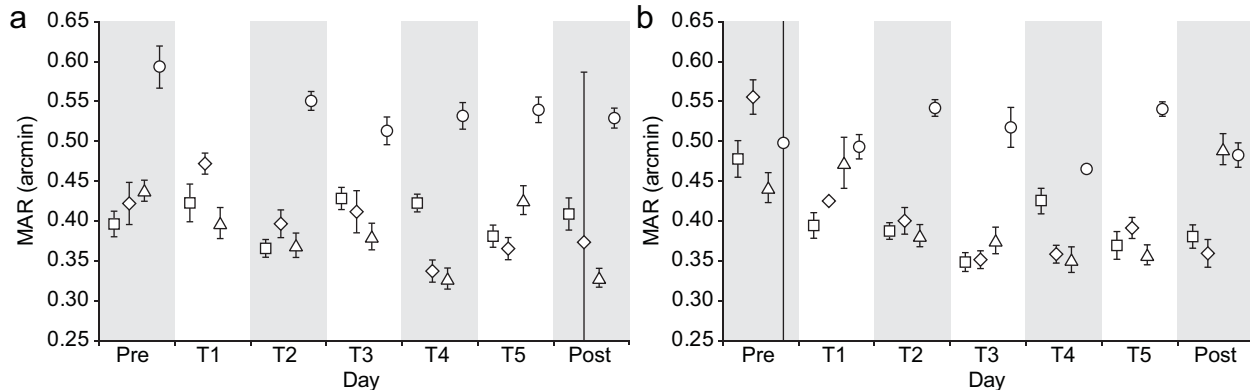


**Figure 3| MAR as a function of time.** MAR for each observer is plotted prior to (Pre), during (T1-T5) and after training (Post) for the 3 mm (a) and 5.81 mm (b) conditions. Observers S1-S4 shown as squares, diamonds, triangles and circles, respectively. Error bars represent  $\pm 1$  SD of the threshold fit.

pre- and post-training thresholds in either the 3 mm ( $p = 0.1306$ ; paired t-test) or 5.81 mm condition ( $p = 0.306$ ; paired t-test). Linear regression lines were fit to the data of each observer individually and averaged. A negative slope would indicate a reduction in threshold across time potentially indicating learning. Individual slopes were negative but close to zero for all but the 3 mm dataset of observer S1. The average slope of all observers was negative, but very close to zero for both the 3 mm condition ( $-0.009$ ; SD = 0.007;  $n = 4$ ) and 5.81 mm conditions ( $-0.01$ ; SD = 0.011;  $n = 4$ ). The mean slope was not significantly different from zero in either the 3 mm ( $p = 0.075$ ) or 5.81 mm ( $p = 0.1525$ ) conditions.

This type of analysis may obscure learning effects that happened during the course of training, so pre-training thresholds were also compared to the best acuities obtained during the course of training. The best acuities were obtained on either the third or fourth day of training for all observers except S1, whose best resolution was obtained on training day 2 for the 3 mm condition. The best resolution overall was obtained by observer S3 on training day 4, with MAR of 0.33 arcmin. The best MAR for observer S1 was 0.35 arcmin obtained on training day 3 in the 5.81 mm condition, while the best MAR for observer S3, of 0.34 arcmin, was obtained in the 3 mm condition on training day 4. Observer S4, the sole myope examined always had the

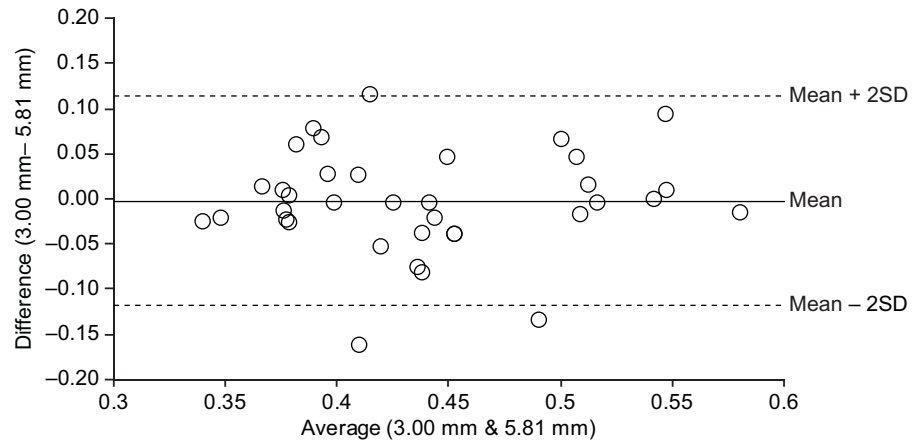


**Figure 4| Bland-Altman plot shows good agreement between results obtained in each AO condition.** The MAR obtained in the 3 and 5.81 mm AO corrected conditions was similar for all observers. The mean difference was close to zero ( $-0.002$  arcmin) and the SD was only 0.0578 arcmin.

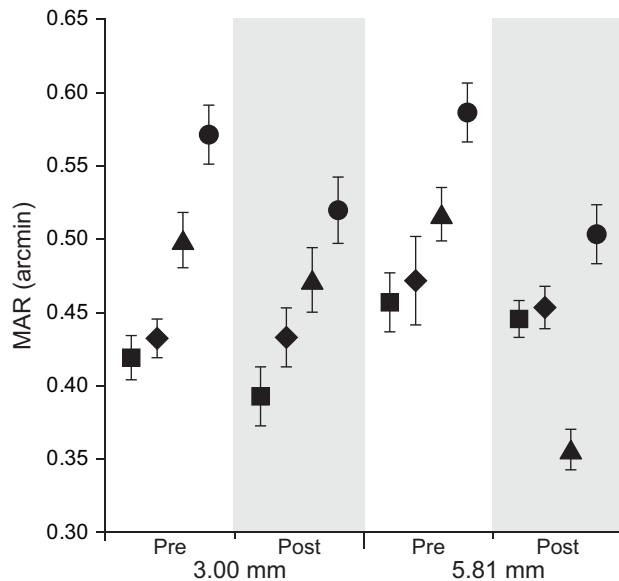


**Figure 5| Pre and post training thresholds for the untrained eye.** Modest threshold reduction was seen in the untrained eyes of each observer for both the 3 and 5.81 mm pupil AO corrected conditions. These improvements were not statistically significant. Observers S1-S4 shown as squares, diamonds, triangles and circles, respectively. Error bars represent  $\pm 1$  SD of the threshold fit.

worst resolution of all subjects, with best resolution of 0.47 arcmin obtained on training day four in the 5.81 mm condition. The best thresholds obtained throughout the course of training were significantly better than the pre-training thresholds in the 3 mm condition ( $p = 0.0193$ ; paired t-test) and very close to being statistically significant for the 5.81 mm condition ( $p = 0.0516$ ; paired t-test).

Pre- and post-training thresholds for the untrained eyes are shown in Figure 5. There were slight improvements in resolution measurements for the untrained eyes of all observers in both conditions. However, the improvement was not statistically significant for either the 3 mm ( $p = 0.0899$ ; paired t-test) or 5.81 mm condition ( $p = 0.1448$ ; paired t-test). Pre- and post-training measurements for the no AO correction condition are shown in Figure 6. For the trained eye there was a slight elevation of threshold in two of the four eyes, while for the untrained eye, all subjects performed worse in the post-training session. However, pre- and post-training measurements made without AO correction were not significantly different ( $p = 0.1845$ ; paired t-test).

Measurements of the residual wavefront aberration after AO correction allowed the modulation transfer function of the eye for each observer in each condition to be calculated

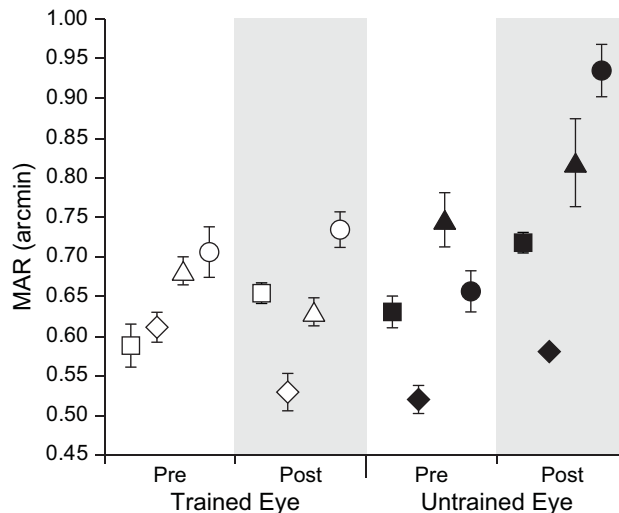


**Figure 6| MAR without AO correction before and after training.** Visual resolution without AO correction improved slightly for two observers for the trained eye (open symbols). Threshold elevations were seen for all observers for the untrained eye (solid symbols). Observers S1-S4 shown as squares, diamonds, triangles and circles, respectively. Error bars represent  $\pm 1$  SD of the threshold fit.

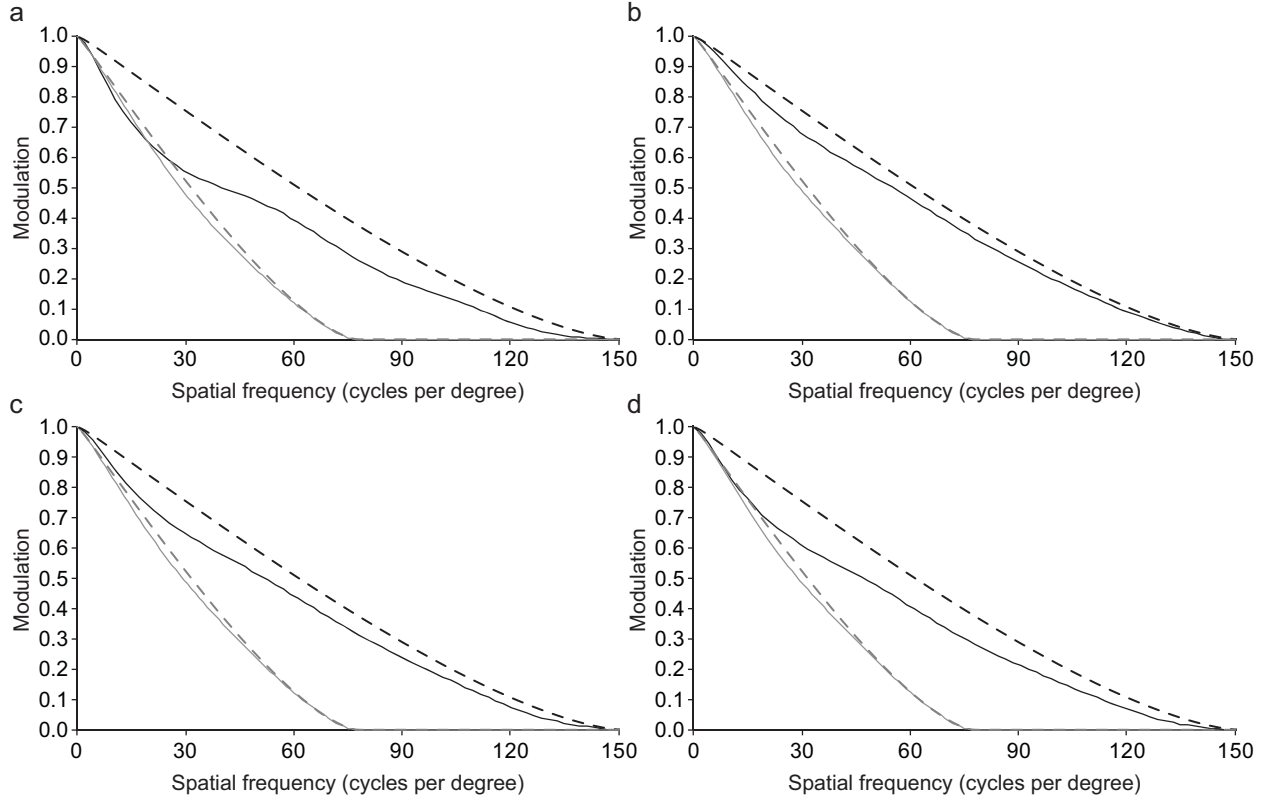


**Figure 7| Modulation transfer functions.** MTFs computed from the residual wavefront aberration for all observers: S1 (a), S2 (b), S3 (c) and S4 (d). MTFs for the 3 mm condition (solid gray lines) were very close to the diffraction limit (dashed gray lines) for all observers. MTFs for the 5.81 mm condition (solid black lines) were worse than the diffraction limit (dashed black lines) and exhibited more variability between subjects.

(Figure 7). For the 3 mm pupil with AO, MTFs closely approach the diffraction limit (dashed gray lines) for each observer (solid gray lines). In the 5.81 mm condition (solid black lines), there was higher contrast than in the 3 mm condition at all spatial frequencies for all observers (except for a small range of spatial frequencies for S1). However, the MTFs in the 5.81 mm condition were not as close to the diffraction limit (dashed black lines), and exhibited more inter-subject variability than in the 3 mm condition.

## 2.5 Discussion

### 2.5.1 Visual Benefit of AO Correction is Immediate

The effect of training on visual performance in this task, if any, was minimal. The visual benefit afforded by AO correction for this task was very rapid, with observers able to take advantage of the improved optical image quality to achieve much better resolution thresholds immediately. This finding is beneficial, for it shows that observers own aberrations do not hinder them from performing extremely well in a visual resolution task after AO correction. The thresholds obtained were excellent, with each emmetropic observer approaching or exceeding Snellen equivalent values of 20/8. Thresholds were slightly better than expected from the theoretical average sampling limit of the cone mosaic, which is thought to be around 0.5 arcmin, but not beyond the range of sampling limits estimated from the data of Curcio (Curcio et al., 1990b). The decision to use a 72.4% correct threshold for this study likely resulted in threshold

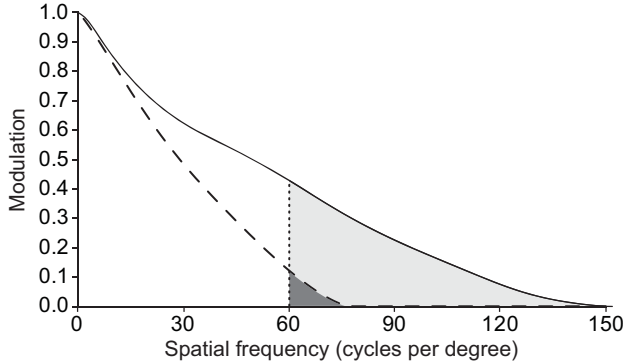


**Figure 8| Information beyond the Nyquist limit.** Average MTFs for the 3 mm (dashed line) and 5.81 mm (solid line) AO conditions. Vertical dotted line marks the theoretical Nyquist limit of the cone mosaic; shaded areas represents aliasing zone. The aliasing zone is much larger for the 5.81 mm (entire shaded area) than 3 mm condition (darker shaded area).

estimates being very low; using a more conservative threshold would increase these values. Since the psychometric functions are quite steep, it is possible that the actual resolution threshold was closer to the average Nyquist limit than these thresholds suggest.

### 2.5.2 Visual Benefit of AO was Similar for Both Pupil Sizes Despite the Optical Benefits of a Larger Pupil

The most interesting finding of the present study was that AO correction over a 3 mm pupil provided the same (or possibly slightly better) visual benefit as AO correction over a 5.81 mm pupil. This was surprising, given the theoretical improvement in optical quality a larger pupil affords after AO correction. Why does such a significant optical improvement not provide a measurable increase in performance? There were likely different limiting factors involved for each condition. For the 3 mm pupil diffraction dominates (Liang et al., 1997) and it can be seen clearly from the MTFs in Figure 7 that the residual wavefront aberration after AO correction yields an MTF that is very similar to that computed for diffraction alone. This results in lower contrast at all spatial frequencies relative to the 5.81 mm condition. This reduced contrast, especially at the highest spatial frequencies, is probably the main optical factor limiting performance in the 3 mm condition.

For the 5.81 mm pupil, the benefits of higher contrast at lower spatial frequencies may be offset by the presence of spatial frequencies beyond the photoreceptor Nyquist limit, which may introduce aliasing distortions. As discussed in Chapter 1, aliasing is the introduction of spurious low spatial frequencies due to under sampling of high spatial frequencies (Williams, 1985a). Figure 8 compares the average MTF computed from the residual wavefront aberration measured for all observers. The shaded region highlights the area of the MTF above 60 cycles per degree, which is the theoretical nominal Nyquist frequency of the cone mosaic (Williams et al., 1987). The entire shaded region represents the aliasing zone for the 5.81 mm pupil while the darker portion of the shaded region denotes the aliasing zone for the 3 mm pupil. Although the 3 mm pupil does introduce a range of spatial frequencies above the nominal Nyquist limit, the contrast of these spatial frequencies is theoretically much higher for the 5.81 mm condition and extends across a larger range including many higher spatial frequencies. Although both conditions are ultimately limited by the Nyquist limit of the cone mosaic and postreceptoral neural processing (Williams et al., 1987), these optical differences are important factors governing visual resolution.

### 2.5.3 What's in an E?

One might ask why use a stimulus such as the tumbling E for measuring visual resolution? This study provides a firm argument for the use of this stimulus. Although it has



**Figure 9| The effect of diffraction blur on tumbling Es and truncated square waves.** Rows a-d show tumbling E; rows e & f show truncated square wave. Stimuli are scaled to be the same size so blur may be examined independent of letter size. Actual size halves in each column from left to right. Distance between two parallel strokes of the E or two bars in grating are, from left to right: 1, 0.5, 0.25, 0.125, and 0.0625 arcmin.

been shown that the difference in amplitude spectra of orthogonal orientations of both the Snellen E and Landolt C (the two most commonly used optotypes) yield a peak in information at spatial frequencies lower than those corresponding to the gap size (Bondarko & Danilova, 1997), it appears that these cues are not utilized. If observers picked up on this low frequency information, either 1) a much larger improvement with training would have been observed, or 2) much lower thresholds would have been measured initially. Figure 9 shows how the blur from diffraction only will affect the light distribution at the retina for a tumbling E of different sizes and orientations. These images were created by convolving the PSF for diffraction only with the light distribution of different sized stimuli. Rows a-d show the effect of diffraction blur (for a 5.81 mm pupil) on the four orientations, each column represents a decrease in letter size of a factor of two. From left to right, the gap in the E is: 1, 0.5, 0.25, 0.125, and 0.0625 arcmin; the Snellen equivalent range is from 20/20 to 20/1.25.

It can be seen from the 0.125 arcmin letters in Figure 9 that even when the information about the parallel strokes of the E have been obliterated by diffraction, the overall pattern looks like a gradient of luminance, being brightest on the side opposite the orthogonal stroke of the E. If observers were using this information, acuities might be expected to approach 0.125 arcmin. However, although this low frequency cue is apparent when looking at the magnified light distribution in Figure 9, it should be remembered that this letter is very small, only 0.625 arcmin high, which is only slightly larger than the spacing between the smallest cones in the center of the fovea. It is more plausible that a larger sized stimulus, such as the 20/5 E in the middle column of Figure 9 might, when sampled by the cone mosaic, more faithfully represent a luminance gradient that might provide a cue to orientation, however if observers were using this information, thresholds would be expected to be much lower than were observed.

Although letters are the most commonly used stimuli for measuring visual resolution (more commonly called visual acuity) in the clinic, the favorite stimulus of the vision science community is a grating or a Gabor patch (which is a grating within a Gaussian envelope). So, why not use gratings and just measure contrast sensitivity? One reason the Snellen E was chosen was practical, due to limitations at the time over control of the modulation of the laser in that the laser could only be turned on or off and not modulated to be at intermediate levels; this ruled out using a sinusoidal light distributions such as a Gabor patches. A truncated square wave stimulus could have been used in a two alternative task, but a pilot study showed that this task could achieve hyperacuity thresholds when observers used low spatial frequency cues. These cues are illustrated in rows e and f of Figure 9, which shows truncated square waves of the same size as the tumbling E's. It can be seen in column four that when information about the grating is lost by blurring due to diffraction, the task reduces to a horizontal versus vertical width judgment, which is a hyperacuity task. The tumbling E task is therefore a powerful tool for studying the limits of visual resolution because it is easy for naïve observers to perform, it is efficient, it does not improve with training and it can be interpreted in a sampling limited framework (Anderson & Thibos, 1999b).

Another interesting result of this experiment, one warranting further study, is the finding that measured thresholds for the myopic observer were never as low as those obtained by the emmetropic observers. Refractive error is an important factor that must be considered when making predictions about the visual benefits of AO correction. There is significant evidence that visual resolution and high spatial frequency contrast sensitivity are reduced in myopia (Atchison, Schmid, & Pritchard, 2006; Coletta et al., 2006; Collins & Carney, 1990; Fiorentini & Maffei, 1976; Jaworski, Gentle, Zele, Vingrys, & McBrien, 2006; Liou & Chiu, 2001; Radhakrishnan,

Pardhan, Calver, & O'Leary, 2004b; Strang et al., 1998; Subbaram & Bullimore, 2002; Thorn, Corwin, & Comerford, 1986). However, it is not known if these differences are due to optical, retinal, or neural causes; the differences between myopes and emmetropes are examined in detail in Chapter 3.

## **2.6 Conclusions**

1. AO correction of ocular aberrations in the AOSLO allows observers to achieve an immediate and significant improvement in visual resolution
2. Training in an AO corrected visual resolution task does not significantly improve performance
3. Any adaptation to ones' own aberrations do not hinder AO correction from providing an immediate visual benefit in this visual resolution task
4. There is no significant difference in resolution when correcting aberrations over a 5.81 mm pupil versus a 3 mm pupil
5. The tumbling E task is a powerful tool for studying the limits of visual resolution

## **Chapter 3**

### **Visual Resolution in Emmetropia and Low-myopia After Adaptive Optics Correction of High-Order Aberrations**

#### **3.1 Abstract**

Myopic observers may not benefit to the same extent as emmetropes from adaptive optics (AO) correction in a visual resolution task. To investigate this, AO-corrected visual resolution was measured in 10 low myopes and 9 emmetropes. Subjects were grouped by refractive error. Mean spherical equivalent refractive error was  $-2.73$  D (SEM:  $0.35$  D) for the myopes, and  $0.04$  D (SEM:  $0.1$  D) for the emmetropes. All subjects had best-corrected visual acuity of 20/20 or better. The AO scanning laser ophthalmoscope (AOSLO) was used to project ultra-sharp stimuli onto the retina of each observer. Visual resolution was measured using a tumbling E test with and without AO correction. AO-corrected MAR was  $0.61$  arcmin (SEM:  $0.02$  arcmin) for the myopes and  $0.49$  arcmin (SEM:  $0.03$  arcmin) for the emmetropes. The difference between groups was significant ( $p=0.0017$ ). The effect was even greater ( $p=0.00013$ ), when accounting for spectacle magnification and axial length, with myopes and emmetropes able to resolve critical features on the retina with a mean size of  $2.87 \mu\text{m}$  (SEM:  $0.07 \mu\text{m}$ ) and  $2.25 \mu\text{m}$  (SEM:  $0.1 \mu\text{m}$ ), respectively. Emmetropes and low myopes both benefited from AO correction in this visual resolution task, but not to the same extent. Optical aberrations did not limit visual resolution in low myopia after AO correction. There was no difference in the high order aberrations of emmetropes and low myopes. Retinal and/or cortical factors limited visual resolution in low myopes after AO-correction.

#### **3.2 Introduction**

##### **3.2.1 Rationale**

It is not known if all eyes, especially those with refractive error, will benefit to the same extent from AO correction. It was shown in Chapter 2 that myopic observers might not benefit to the same extent as emmetropes after AO correction. However, the sole observer in that study might not be representative of all myopes. The two previous studies that examined the benefit of AO correction on visual performance have had a small number of observers (7 or less) and have not been explicit as to the magnitude of ocular aberrations present in these eyes, or their refractive error. Yoon and Williams reported the refractive error of only two of the six observers whose acuities were measured (both slightly myopic) and Poonja et al. made no reference to the refractive error of the subjects they tested (Poonja et al., 2005; Yoon et al., 2002). Refractive error is an important factor to consider when examining the improvements afforded by AO, as there is a large amount of evidence for reduced visual resolution and high frequency contrast sensitivity in myopia (Atchison et al., 2006; Coletta et al., 2006; Collins et al., 1990; Fiorentini et al., 1976; Jaworski et al., 2006; Liou et al., 2001; Radhakrishnan et al., 2004b; Strang et al., 1998; Subbaram et al., 2002; Thorn et al., 1986).

##### **3.2.2 Factors Limiting Resolution in Myopia**

Reduced visual performance in myopia may be attributed to optical, retinal, or cortical factors, or some combination of the three (see Chapter 1); differences might be expected in all three categories in myopia. Some studies have shown that the optical quality of myopic eyes is worse than emmetropic eyes, in that they exhibit increased monochromatic aberrations (Applegate, 1991; Buehren, Collins, & Carney, 2005; Collins, Wildsoet, & Atchison, 1995; He et

al., 2002; Marcos, Berbero, & Llorente, 2002; Paquin, Hamam, & Simonet, 2002), while others have not found a correlation between refractive error and monochromatic aberrations (Artal et al., 2006; Carkeet, Luo, Tong, Saw, & Tan, 2002; Cheng, Bradley, Hong, & Thibos, 2003; Netto, Ambrósio, Shen, & Wilson, 2005; Porter et al., 2001; Radhakrishnan et al., 2004b; Zadok et al., 2005; Charman, 2005). Myopia can be axial or refractive, in that the axial length can be too long for the optics of the eye, or the optics can be too strong for the axial length of the eye; in both cases the myopic eye forms a focused image in front of the retina, and an out of focus image at the retina. Retinal changes due to increased axial length in myopia may also affect visual performance and retinal functioning in myopia.

### **3.2.3 Retinal Stretching in Myopia**

Retinal stretching from increased axial length in myopia has been shown to decrease the neural sampling density of the myopic retina (Coletta et al., 2006; Troilo, Xiong, Crowley, & Finlay, 1996). However, recent evidence suggests that at the center of the fovea there is no correlation between axial length and cone spacing (Li, Tiruveedhula, & Roorda, 2009). Peripheral acuity has been shown to be limited by retinal stretching in myopia, and in some cases been shown to limit foveal acuity in myopes (Chui, Yap, Chan, & Thibos, 2005). Jaworski et al. (Jaworski et al., 2006) found reduced visual sensitivity in a spatial summation task in high myopia but normal contrast sensitivity at low spatial frequencies, implying normal photoreceptor function but dysfunction of postreceptor elements. This would suggest that the photoreceptors maintain their sensitivity but are stretched over a larger area of the retina. Further evidence for altered retinal functioning in myopia comes from multifocal electroretinograms of myopic retinas, which show reduced and/or delayed responses, even in low myopia (Chen, Brown, & Schmid, 2006; Kawabata & Adachi-Usami, 1997).

### **3.2.4 Cortical Sensitivity to High Spatial Frequencies in Myopia**

Differences in cortical sensitivity in myopia may also play a role in limiting the ability of myopes to resolve high spatial frequencies. This impairment may be due to the fact that during the critical early stages of development of the visual system, the cortical neurons responsible for processing fine detail are stimulated less frequently. Neural channels tuned to the highest spatial frequencies that drive resolution of fine spatial detail may require input at the proper spatial frequency range for normal development. The highest spatial frequency channels could be impaired in myopia due to the fact that uncorrected young myopes will only experience clear vision of fine details when objects are very near to them (Fiorentini et al., 1976). Even the best-corrected adult myope may typically experience more chronic blur. This could be a result of their not constantly wearing their correction or from wearing an imprecise correction. However, there is little hard evidence to support this conjecture.

### **3.2.5 Blur Adaptation and Myopia**

It is possible that the effect of chronic blur in myopia might actually improve rather than reduce visual resolution. Blur adaptation studies, in which subjects wore fogging lenses during extended periods of natural viewing (preventing high spatial frequency input to the visual system) have shown that visual resolution improves in both myopes and emmetropes after a couple hours of adaptation (George & Rosenfield, 2004; Mon-Williams, Tresilian, Strang, Kochhar, & Wann, 1998; Rosenfield, Hong, & George, 2004). The underlying mechanism appears to be cortical in locus, as studies have shown that this phenomena exhibits inter-ocular

transfer to the untrained eye (Mon-Williams et al., 1998). Webster and colleagues have shown that a similar effect of neural sharpening can occur in mere seconds after viewing spatially filtered natural images (Webster et al., 2002). It has been proposed that this is related to the spatial frequency specific adaptation shown by Georgeson and Sullivan (Georgeson et al., 1975), whereby the spatial frequency content of the visual world is optimized so as to give the sharpest percept.

Adaptation state therefore is something that must be carefully considered in visual performance studies. Some researchers have suggested that normal persons exhibit some adaptation to their own particular pattern of aberrations (Artal et al., 2004). Neural adaptation after laser eye surgery has been suggested as a possible reason that improvements in visual acuity after laser refractive surgery are not seen for weeks (Pesudovs, 2005). However, as shown in Chapter 2, there is little evidence that adaptation to ones prior aberration state prevents observers from achieving significant resolution improvement after AO correction. It is possible that there may be two different adaptation mechanisms at work: one that is fast-acting and works to optimize the percept based upon the spatial frequency content of the entire visual scene (i.e. Webster et al., 2002) and another that acts over a longer time course (i.e. Artal et al., 2004) to provide the sharpest image by minimizing the effect of persistent optical aberrations.

### 3.2.6 Overview

To examine the extent to which high order aberrations limit visual resolution in myopia, the visual resolution of 10 low myopes is compared to 9 emmetropes. Low myopes were chosen so that any major retinal pathology related to high myopia could be avoided, and for technical limitations, which make it difficult to image high myopes in AOSLO. Furthermore, it may be the case that previous researchers have found reduced visual resolution in myopia due to the fact that the high myopes in their studies may have biased the results. Limiting ourselves to studying low myopes eliminates this possibility.

### 3.3 Methods

#### 3.3.1 Participant Screening & Clinical Testing

Participants were recruited from the student population of the University of California, Berkeley. Informed consent was obtained from the participants after the nature and possible complications of the study were explained verbally and in writing. This experiment was approved by the University of California, Berkeley Committee for the Protection of Human Subjects. Each participant was refracted clinically using monocular subjective refraction (with fogging), and placed into the myopic or emmetropic group. As the intention was to only include persons with low myopia, any potential subjects with more than 4D of myopia and/or more than 1.25 D of astigmatism were excluded. The emmetropic group was defined as those participants having between -0.25 D and +0.75 D of spherical refractive error and no more than 0.25 D of astigmatism.

Mean spherical refractive error was -2.45 D (SEM: 0.34 D, range: -0.5 D to -3.75 D) for the myopes and 0.06 D (SEM: 0.1 D, range: -0.25 D to +0.75 D) for the emmetropes. Mean cylindrical refractive error was -0.55 D (SEM 0.16 D, range: -1.25 D to 0 D) for the myopes and -0.04 D (SEM: 0.03 D, range -0.25 D to 0 D) for the emmetropes. All participants had best-corrected visual acuity of 20/20 (MAR of 1 arcmin) or better, as measured clinically using the Bailey-Lovie chart (Bailey & Lovie, 1976). Mean clinically measured MAR of all subjects was 0.83 arcmin (SEM: 0.02 arcmin). The mean age of the myopic group was 25 years (SD: 4.9,

range: 20–35), and the mean age of the emmetropic group was 29 (SD: 7.5, range: 22–41). Participant screening included a self-report questionnaire about ocular health history. Persons who had undergone refractive surgery and those with a history of eye problems were excluded from this study. For the myopic participants, questions were asked related to their history of myopia, correction type and wearing habits. This data is summarized in Table 1.

	<b>Age of myopia onset</b>	<b>Myopia progressing?</b>	<b>Correction method</b>	<b>Years wearing correction</b>	<b>Frequency of wearing (hrs/day)</b>
M1	8	No	S	17	8
M2	16	No	S	15	16
M3	15	No	S	20	8
M4	16	No	S	5	1
M5	12	Yes	CL(T)	8	10
M6	17	Yes	S	11	15
M7	13	No	CL	11	12
M8	12	Yes	S	6	16
M9	18	Yes	S	1	16
M10	6	No	CL	5	16

**Table 1| History of myopia and correction wearing habits for myopic group.** S: spectacles, CL: soft contact lenses CL(T): toric soft contact lenses.

### 3.3.2 Axial Length Measurements

Axial length was measured using ultrasound biometry (Mentor Scan-A III, Mentor Corporation, California). Axial lengths were measured five times; all measurements reported and used in calculations are the mean of the five measures. Axial lengths were not measured on the same day as the psychophysics experiments, so as to avoid any possible short term deformation or desquamation of the corneal epithelium due to measurement. The myopes had axial lengths ranging from 23.57 mm to 25.48 mm (mean: 24.65 mm, SEM: 0.22 mm). The emmetropes had axial lengths ranging from 21.74 mm to 23.8 mm (mean: 22.91 mm, SEM: 0.19 mm). Axial length as a function of spherical equivalent refractive error is shown in Figure 10. All myopes with a spherical equivalent refractive error greater than -2.5 D had an axial length longer than 24.5 mm. There was a large range of axial lengths for the emmetropes that were classified as plano during subjective refraction, spanning just over 2 mm, from 21.74 mm to 23.8 mm.

### 3.3.3 AOSLO Imaging & Psychophysics

The AOSLO was used to project a high contrast stimulus onto the retina of each observer using methods described in Chapter 2 and elsewhere (Poonja et al., 2005). Only relevant differences between the methods used in Chapter 2 will be discussed herein. The field size was approximately 30 x 30 arcmin, with the central 10 x 10 arcmin area optimized to occur over the most linear section of the sinusoidal horizontal scan. Linearization of the central portion of the

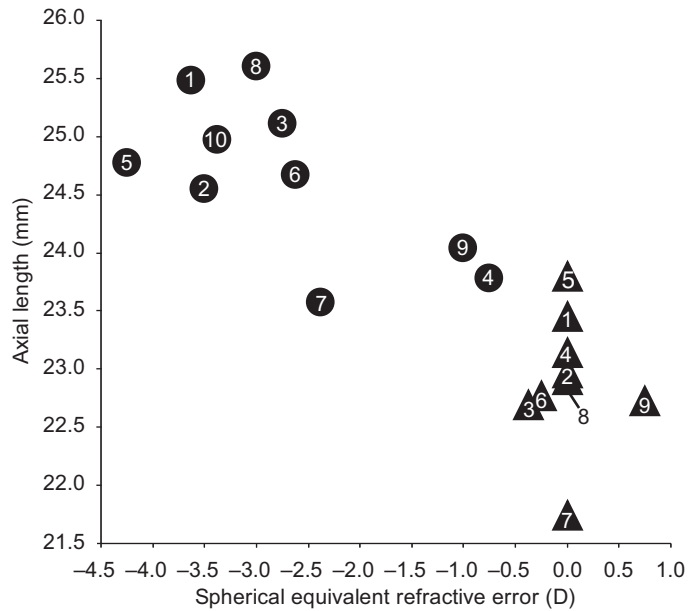


**Figure 10| Spherical equivalent refractive error as a function of axial length.** Myopes shown as circles; emmetropes shown as triangles. Observer number is given inside symbol.

scan was accomplished by projecting a checkerboard target of known pixel dimensions onto the calibration grid and setting them to be in register. This resulted in the central  $10 \times 10$  arcmin section being approximately linear, with  $\sim 16$  pixel lines corresponding to 1 arcmin. This smaller field size was used such that there were smaller steps between different image sizes, allowing for a more refined estimate of the threshold, and so that a larger range of stimuli could be used that still fell within the linear range of the raster scan.

Visual resolution was measured in the following two conditions: 1) spectacle-corrected without AO and 2) spectacle-corrected with AO. Mydriasis and cycloplegia were induced with 1 drop of 2.5% phenylephrine and 1 drop of 1% tropicamide  $\sim 20$  minutes prior to the start of the experimental session, and were maintained throughout with an additional drop, if necessary. If the observer was unable to keep their eye open throughout the duration of the experiment, they were excluded from analysis; one emmetrope was excluded for this reason. Low order aberrations were corrected with spectacle lenses and fixed defocus levels were determined as outlined in Chapter 2. If a fixed defocus level was needed, it was placed onto the deformable mirror for the experimental trials. This was done separately for each condition. For the AO condition, aberrations were corrected through the best spectacle lens correction and a second subjective refraction was performed. Most subjects did not require any additional defocus.

Visual resolution was assessed using a four alternative forced choice (4AFC) tumbling E test. The threshold, as determined by QUEST (Watson & Pelli, 1983), was the MAR that the observer could correctly identify 82.5% of the time. QUEST was implemented in the AOSLO so that resolution measurements could be obtained quickly and so that more stimuli could be presented near the threshold. One eye was imaged for each subject (typically the right eye); the fellow eye was occluded. The stimulus was presented in Maxwellian view (Maxwell, 1860, cited in: (Westheimer, 1966)), at a retinal illuminance of 6.79 log Trolands. Retinal illuminance in Trolands was calculated based upon a laser power of  $10 \mu\text{W}$  over an area of 0.25 degrees<sup>2</sup> (Wyszecki et al., 1982). This power level is less than 1% of the American National Standards Institute (ANSI) maximum permissible exposure for continuous viewing of a 658 nm source of this size (American National Standards Institute, 2000). This high retinal illuminance was used so that high contrast retinal images could be obtained during the psychophysical task.

Each trial was initiated with a keyboard press by the participant. After a brief delay (~200 msec.) the stimulus was presented in one of four randomly chosen orientations and a video of the retina was acquired. Stimulus duration was 500 msec. Video of the retina was acquired for 2 sec. Videos were acquired to determine the preferred fixation locus and cone spacing of the observer. At the end of each presentation the participant indicated the orientation by pressing an arrow key on the keyboard. Experiment control and data acquisition were accomplished through a custom MATLAB (The Mathworks, Natick, MA) graphical user interface (GUI) which controlled custom C++ software developed in this laboratory. QUEST was implemented in MATLAB using the Psychophysics Toolbox extensions (Brainard, 1997; Pelli, 1997).

After one initial practice run, five threshold measurements were made for each condition, with AO and no AO runs interleaved. Runs consisted of 60 trials each. Thresholds presented are the average of five runs. Participants were instructed to rest during the breaks between runs and at their discretion throughout the experiment to minimize fatigue (this was easily accomplished as the observer self-initiated each trial). During the AO condition, an AO correction was done prior to the beginning of a run and again half way through (after trial 30). AO correction was optimized by the experimenter to give the lowest RMS wavefront error. If a defocus level was preferred by the observer it was placed onto the DM. The experimenter monitored AO compensation by viewing the live AO corrected image of the retina on a CRT. If the image quality deteriorated, the subject was instructed to pause and another AO correction was performed. Typically, only two AO corrections were made during each AO condition run.

### 3.3.4 Calculation of Magnification Factor

Due to the fact that low order aberrations (defocus and astigmatism) were corrected using trial lenses in the AOSLO system, slight spectacle magnification effects might tend to exaggerate or eliminate any small differences that may exist between groups. The spectacle magnification factor was calculated from the trial lens power in the system. The axial length was measured. These factors were used to calculate the size of features in the retinal image. This was important for relating the size of a detectable stimulus feature to the size of individual cone photoreceptors in the retina.

The standard thin lens equation was used to calculate the magnification factor due to the spectacle lenses:

$$M = \frac{1}{1 - dP} \quad (1)$$

Where  $M$  is the spectacle magnification factor (a unit-less value),  $d$  is the distance from the entrance pupil to the spectacle lens (in mm) and  $P$  is the lens power (in D). Using a constant value of 14 mm might seem simplistic, as there is indeed some variation in the distance from the lens well to the entrance pupil of the eye. These are due to individual differences in head and face shape, bite bar, and constraints imposed by the optical bench. However, this equation is very insensitive to small variations: for a -4 D myope (the largest in this study), an error in distance of  $\pm 2$  mm would only change the magnification factor by  $\sim \pm 0.007$ , or less than one percent in either direction.

### 3.3.5 Calculation of the Size of Retinal Features

Bennett's adjusted axial length method was used to calculate the size of features in the retinal image (Bennett, Rudnicka, & Edgar, 1994). Bennett's method has the advantage that the only biometry that is needed to convert from degrees of visual angle to mm on the retina is the

axial length. This allows for the calculation of  $q$ , a scaling factor relating the two units. Multiplying a known visual angle by  $q$  gives the size of the corresponding retinal features in mm. The equation for calculating  $q$  is:

$$q = 0.01306(x - 1.82) \quad (2)$$

Where  $x$  is the axial length in mm, 1.82 is the distance from the corneal vertex to the eye's second principal point, in mm (taken from the Bennett-Rabbets model eye), and 0.01306 is a constant that converts radians to degrees and takes into account  $n$ , the refractive index of the eye, which is taken to be 1.336 (Bennett & Rabbets, 1989; Bennett et al., 1994). For a 24 mm emmetropic eye,  $q = 0.289$ , and one degree of visual angle equals 0.289 mm or 289  $\mu\text{m}$  on the retina. Here, again an approximation is made by using 1.82 mm as the distance from the corneal vertex to the eye's second principal point, but confidence may be had that any individual variations will have only a small effect on  $q$ . Bennett states that individual variations in the distance between the corneal vertex and the eye's second principal point are unlikely to exceed  $\pm 0.55$  mm. The resulting maximum error in  $q$  is only the ratio of 0.01306 and 0.55, or 0.007 (Bennett et al., 1994).

### 3.4 Results

#### 3.4.1 Raw MAR with and without AO Correction

Mean raw (unadjusted for spectacle magnification) AO corrected MAR was 0.61 arcmin (SEM: 0.02 arcmin) for the myopes and 0.49 arcmin (SEM: 0.03 arcmin) for the emmetropes. These values correspond to Snellen acuities of 20/12.1 and 20/9.9. The difference between groups is significant ( $p=0.0017$ , t-test, two-tailed). Results for the myopic group are shown in Figure 11 and for the emmetropic group in Figure 12. Mean MAR for all observers before AO

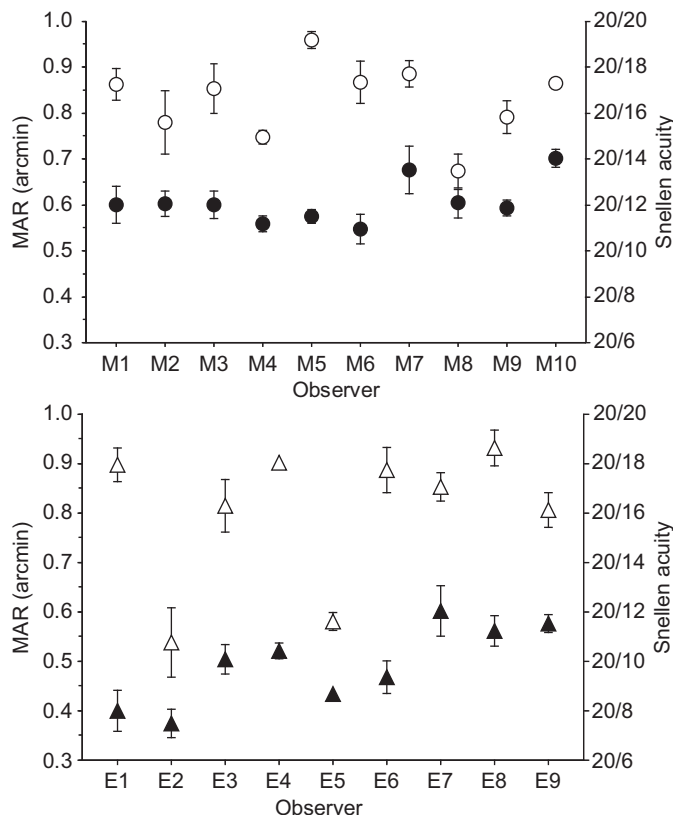


**Figure 11| Raw MAR for the myopic group.** Filled symbols are with AO-correction; open symbols are without AO-correction. Error bars are  $\pm$ SEM.

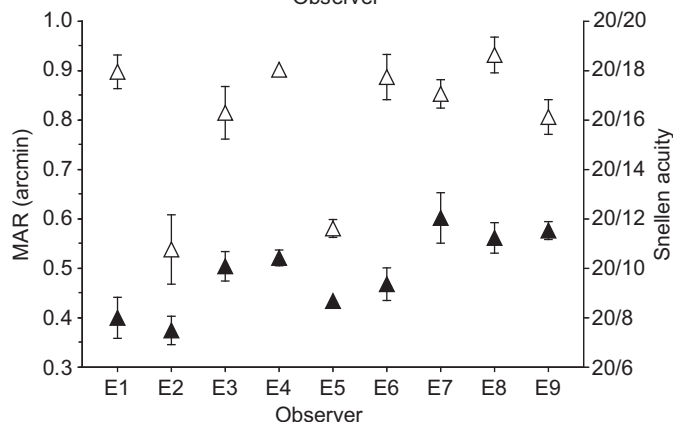


**Figure 12| Raw MAR for the emmetropic group.** Filled symbols are with AO-correction; open symbols are without AO-correction. Error bars are  $\pm$ SEM.

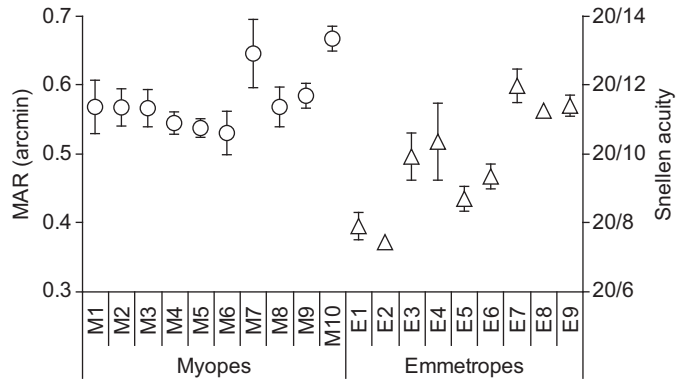


**Figure 13| Spectacle magnification adjusted AO corrected MAR.** Error bars are  $\pm$  SEM. Spectacle magnification slightly reduces the difference between groups.

correction was 0.81 arcmin, which is very similar to the 0.83 arcmin MAR measured clinically with the Bailey-Lovie chart (Bailey et al., 1976). Within each group, there was a significant improvement in visual resolution after AO correction of high order aberrations. The myopic group improved from a mean of 0.83 arcmin in the no AO condition to a mean of 0.61 arcmin with AO, a 27% reduction in MAR. The emmetropes improved to an even greater extent, from a group mean of 0.8 arcmin without AO correction to a mean of 0.49 arcmin with AO, a 39% reduction in MAR. These reductions are consistent with the 33% reduction in MAR found by Poonja et al. (Poonja et al., 2005), and the 37.5% reduction found by Yoon and Williams (Yoon et al., 2002).

### 3.4.2 Spectacle Magnification Adjusted MAR

The difference between groups is less significant when taking into account magnification effects from the spectacle lenses used to correct low order aberrations. The mean spectacle magnification adjusted AO corrected MAR is reduced to 0.58 arcmin for the myopes; it remains essentially unchanged, at 0.49 arcmin, for the emmetropes. Spectacle magnification reduced the angular retinal image size by ~5.2% for the myopes. Spectacle magnification adjusted AO corrected MAR for both groups is shown in Figure 13. Although the groups become more similar after adjusting for spectacle magnification effects, there is still a statistically significant difference between them ( $p=0.0082$ , t-test, two-tailed).

### 3.4.3 Critical Feature Size: Resolution in Retinal Units

The difference between the myopic and emmetropic groups is enhanced over even the raw MAR values when accounting for both spectacle magnification and axial length ( $p=0.00013$ , t-test, two-tailed). Visual resolution (commonly visual acuity) is typically defined as the finest spatial detail that the visual system can resolve. When relating the performance in terms of actual spatial units on the retina, as opposed to MAR, the critical feature size (CFS) of the stimulus must be defined. The CFS is simply the size in  $\mu\text{m}$  of the smallest detectable feature on the retina of the Snellen E that is required to correctly judge its orientation. The CFS for a

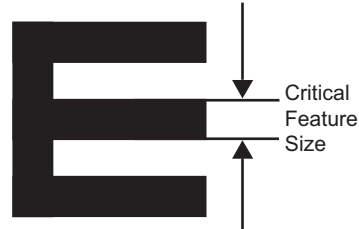


**Figure 14| Critical feature of the Snellen E.** The size of the critical feature is equal to the distance on the retina (in  $\mu\text{m}$ ) of one half cycle of the high spatial frequency square wave component.

Snellen E is defined as the distance on the retina (in  $\mu\text{m}$ ) between two successive bright bars in the strokes of the Snellen E, or one half cycle of the high spatial frequency square wave component embedded in the Snellen E (Figure 14). Myopes are able to resolve a critical feature on the retina with a mean size of  $2.87 \mu\text{m}$  (SEM:  $0.07 \mu\text{m}$ ) and emmetropes a CFS of  $2.25 \mu\text{m}$  (SEM:  $0.1 \mu\text{m}$ ). Acuities in terms of CFS are shown in Figure 15.

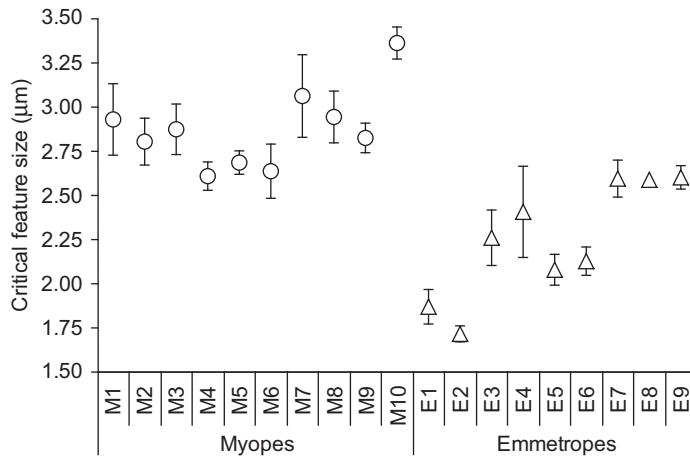


**Figure 15| AO corrected critical feature size.** Critical feature size is the actual size of the gap in the E on the retina (see Figure 14). Error bars are  $\pm\text{SEM}$ .

### 3.4.4 Optical Quality in Emmetropia and Low Myopia

The radial average modulation transfer functions were computed for each observer from the residual wavefront aberration after AO correction and are shown in Figure 16. MTFs after AO correction were quite similar for both groups, showing each group achieved similar levels of AO compensation for their optical aberrations. There was no significant difference in the total RMS wavefront error between the myopes and emmetropes before AO correction (mean myopes:  $0.4 \mu\text{m}$ , SEM:  $0.12 \mu\text{m}$ ; mean emmetropes:  $0.32 \mu\text{m}$ , SEM:  $0.08 \mu\text{m}$ ;  $p>0.5$ , t-test, two-tailed). Nor was there a significant difference between groups in total RMS wavefront error after AO correction (mean myopes:  $0.079 \mu\text{m}$ , SEM:  $0.017 \mu\text{m}$ ; mean emmetropes:  $0.081 \mu\text{m}$ , SEM:  $0.022 \mu\text{m}$ ;  $p>0.9$ , t-test, two-tailed).

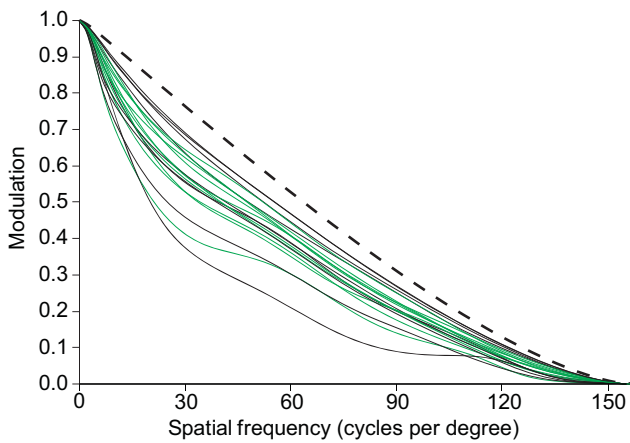


**Figure 16| Modulation transfer functions.** MTFs of myopes (green) and emmetropes (black) were quite similar after AO correction. The diffraction limited MTF (dashed black line) is shown for comparison.

The magnitudes of Zernike modes 3–21, before and after AO correction are shown in Figure 17 and Figure 18, respectively. These were computed by first taking the absolute value of the residual RMS error for each Zernike mode for each observer and then averaging within

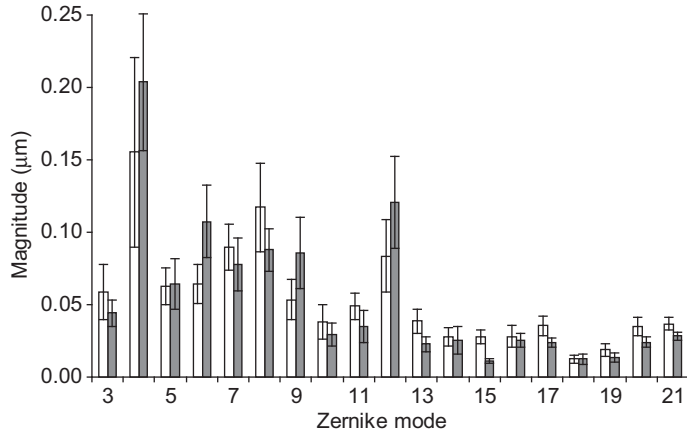


**Figure 17| Zernike modes 3-21 without AO-correction.** Magnitude of Zernike modes 3-21 for myopes (open bars) and emmetropes (shaded bars) after spectacle correction, but without AO correction. Error bars are  $\pm$ SEM.

groups. It can be seen from Figures 17 & 18 that the magnitudes of Zernike modes 3–21 are very similar between groups prior to and after AO correction. Zernike modes above mode 21 are excluded because their magnitudes are so small as to be of little consequence. It is difficult to interpret the impact of individual modes simply by their magnitude, as they tell little about their effect on vision or about the subjective image quality of the observer. This is because not all Zernike modes have the same effect on vision and can have complex interactions with one another that can either enhance or degrade subjective image quality and visual resolution (Applegate et al., 2003b; Applegate et al., 2003a; Chen et al., 2005).

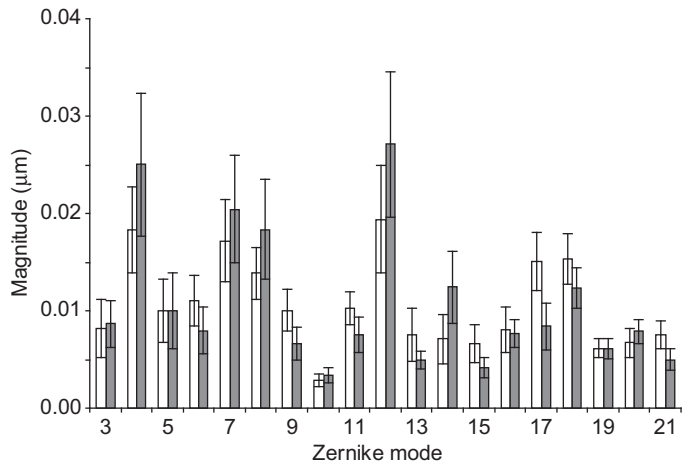


**Figure 18| Zernike modes 3-21 with AO-correction.** Magnitude of Zernike modes 3-21 for myopes (open bars) and emmetropes (shaded bars) after AO correction. Error bars are  $\pm$ SEM. Note the difference in scale from Figure 17.

### 3.5 Discussion

#### 3.5.1 AO Correction Benefits Myopes Less Than Emmetropes Despite Similar Optical Quality After AO Correction

AO correction of the eye's high order aberrations improves visual resolution in both myopes and emmetropes, but not to the same extent. Because both groups received similar levels of optical quality through AO compensation for their aberrations, it is unlikely that this difference was due only to residual optical factors. The MTFs (Figure 16) and residual wavefront RMS for Zernike terms 3-21 (Figures 18) are very similar for both groups after AO correction. Although individual Zernike modes tell us little about subjective image quality, it has

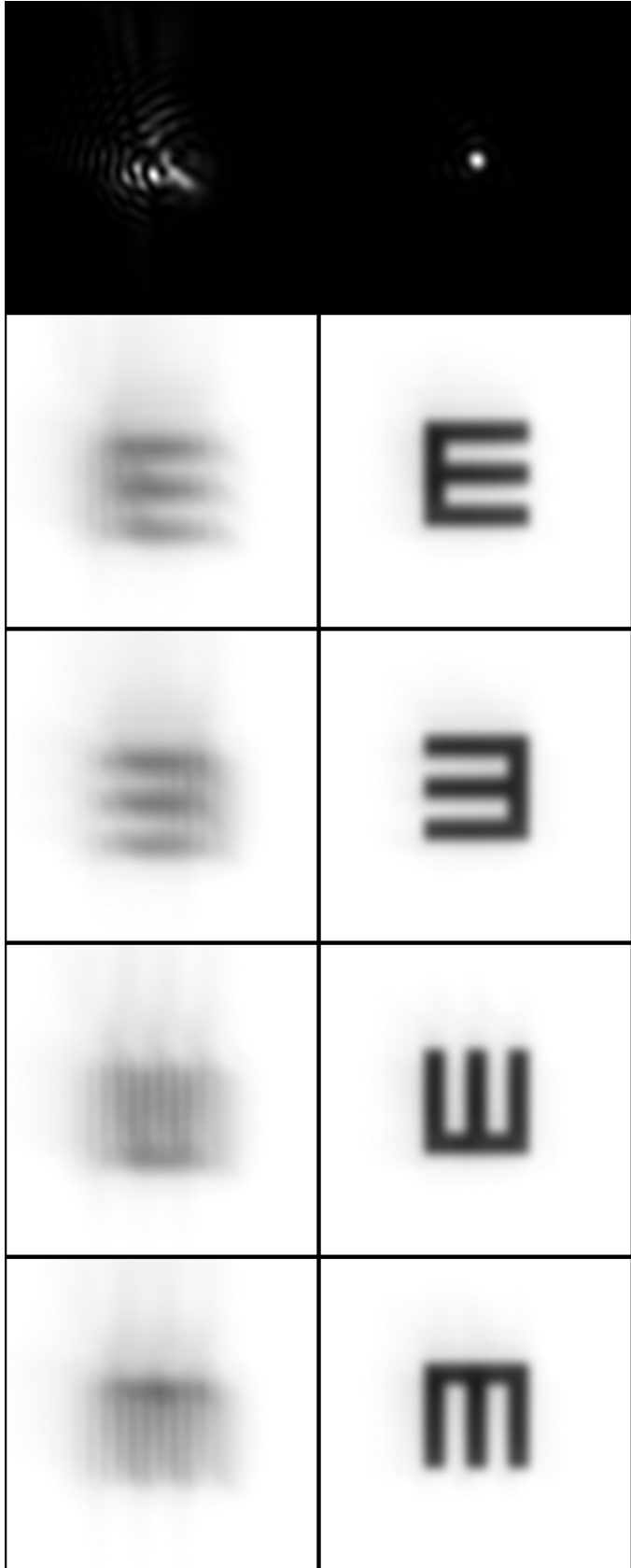


**Figure 19| PSFs and convolved Snellen E's for subject M10.** PSFs are shown in the top row. Convolved threshold sized Snellen E's at each of the four orientations used in the acuity test are shown without (left column) and with AO-correction (right column).

been shown that very low levels of RMS error ( $<0.05 \mu\text{m}$ ) have no significant effect on visual resolution (Applegate et al., 2003a). All aberrations after AO correction fell below this level (Figure 18). The image quality that the observers in this study experienced can be approximated by convolving their individual point spread function (PSF) with a properly scaled Snellen E.

This was performed for all of the participants in this study; the results for M10, the worst performing myope in the AO condition, are shown in Figure 19. The corresponding wavefront aberration maps, MTF and PTF before and after AO correction are shown in Figures 20, 21 & 22, respectively. The right column of Figure 19 shows the AO corrected PSF (top), with the corresponding convolved Snellen Es at the four orientations tested, scaled to be at threshold (0.7 arcmin), shown below. The top left column shows the PSF and convolved Es without AO, again scaled at threshold for that observer (0.87 arcmin). Scaling the letters to be equal size allows the effects of the PSF on the image quality to be examined independent of letter size (in the same way as Figure 9). It is obvious that optical degradations caused by ocular aberrations are minimized in the AO condition such that they no longer are a limiting factor for determining stimulus orientation.

It can be seen from Figure 19 that without AO correction, the PSF of a normal eye has two main effects on a Snellen E. First, it reduces the overall contrast, which can easily be inferred by

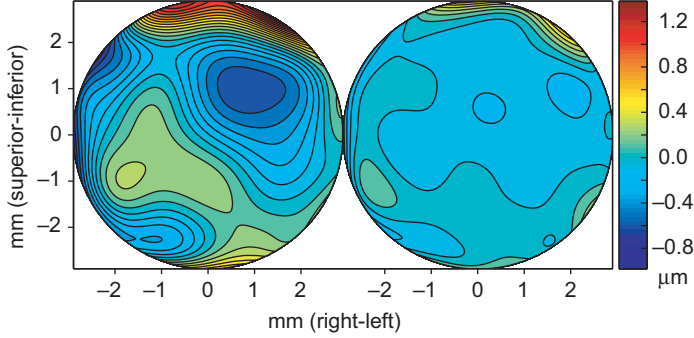


**Figure 20| Wavefront aberrations under each condition for subject M10.**  
Wavefront aberration for subject M10 before (left) and after (right) AO-correction. Contour lines are separated by 0.1 microns; color bar shows size relations in microns.

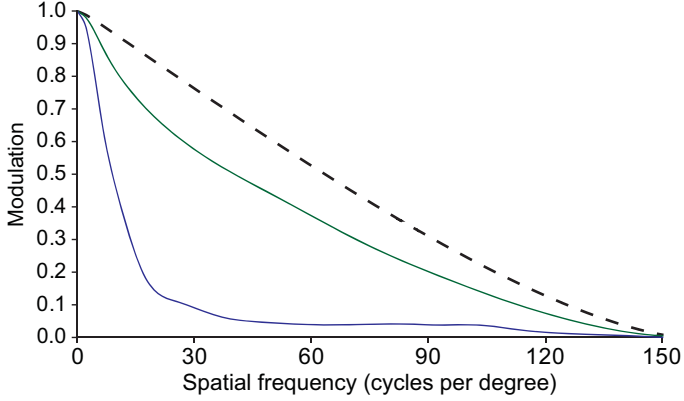


**Figure 21| MTF before and after AO correction for subject M10.** MTF before (blue) and after (green) AO-correction; diffraction limited MTF (dashed black line) is shown for comparison.

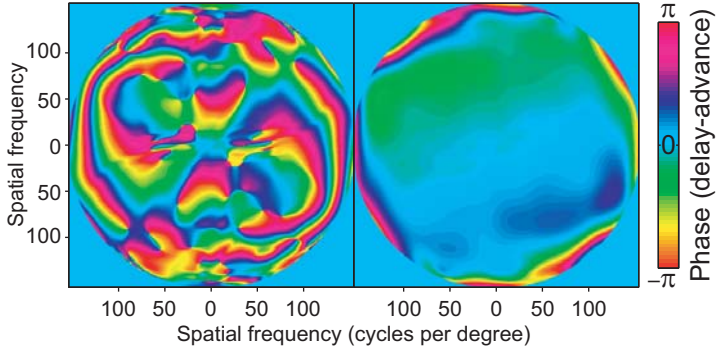


**Figure 22| PTF before and after AO correction for subject M10.** PTFs before (left), and after AO (right). Color indicates phase delay/advance.

looking at the corresponding MTF (Figure 12, blue curve). Secondly, and probably more importantly, it disrupts the relationship between the different spatial frequency components of the Snellen E. Depending upon the orientation of the letter, this effect can be moderate, as in the normally oriented E, or it could be more severe, as it is for the vertically oriented E's. A striking feature of Figure 19 is how much information about the orientation still exists in the stimulus even when a great deal of the high spatial frequency information has been blurred out by the optical aberrations of the eye. This illustrates how over-simplistic the notion of visual resolution based upon Snellen letters (or any optotype) is. As discussed in Chapter 2, it is possible that a trained observer might be able to pick up on the low spatial frequency cues to orientation, such as the gradient of contrast present in the blurred letters of Figures 9 & 19. However, there is little or no evidence that training improves in most foveal resolution tasks (Fine et al., 2002; Johnson et al., 1979; Westheimer, 2001) and evidence presented in Chapter 2 suggests that the tumbling E task is not susceptible to perceptual learning, even when considering the potential for learning these low frequency cues that might be more salient after AO correction (see Chapter 2).

Furthermore, it has been shown by others that the tumbling E task used herein is a sampling limited task (Anderson & Thibos, 1999a). Only one observer in this study, E2 (one of the authors; (AR); subject S1 from Chapter 2), had any significant experience in the task, so it is unlikely that any experience-dependent effects might have biased the results.

### **3.5.2 Increased Photoreceptor Spacing or Decreased Neural Sensitivity in Myopia?**

Taking into account all of the information available about the optical and retinal image quality after AO correction, optics are most likely no longer a limiting factor for this task. It then remains to be determined which of the other possible explanations for the observed differences are the most plausible. To review, the remaining possibilities limiting visual performance in myopia are retinal and/or cortical in nature. The main retinal limitation would be the sampling grain of the photoreceptor mosaic. Changes in the myopic retina may occur at either the photoreceptor level or at a post-receptoral level within the retina. Cortical limitations are more difficult to isolate, but they could be related to adaptational or developmental effects. The question of adaptation state is an interesting one that needs further investigation. If, as Artal and colleagues have suggested, there is in fact some adaptation to aberrations (Artal et al., 2004), then there remains the question of the time course and mechanism of this adaptation. It is possible that in removing the aberrations of the eye, the full potential increase in visual performance was not realized because the previous adaptation state was still in effect (Artal et al., 2004); it was shown in Chapter 2 that this is highly unlikely for this task.

However, might myopes be more susceptible to this? Or is it possible that the adaptation effect is merely subjective and does not really have a bearing on visual resolution measurements? In natural viewing conditions the eyes aberrations change, both with accommodation (e.g. spherical aberration) and light level (ie. pupil size) (Cheng et al., 2004) making the notion of adaptation to one's own aberrations quite complex. Presumably the brain would have to either have an infinite number of adaptation states to cover all of these conditions, or the adaptation mechanism would only apply to those aberrations that are static. Even the latter situation would seem to require multiple adaptation states, because the complex interaction of aberrations with one another in different viewing conditions would have different effects on retinal image quality. Artal and colleagues suggest that there may be a rough adaptation to the general shape of the PSF, which does not change too drastically in different viewing conditions (Artal et al., 2004). However, even this explanation seems tenuous as the aberrations in each eye are different, and although usually mirror symmetric (Porter et al., 2001), the “shape” of the PSF is different in each eye, since most cortical neurons are binocular it is unclear how this mechanism would be implemented and at what level in the visual system it would occur. Whether or not significant differences in the adaptation states of myopes and emmetropes would result in the differences that were measured remains unclear but probably is an unlikely explanation for the observed difference.

The value of 0.49 arcmin MAR obtained with AO correction for the emmetropic group is precisely what would be predicted from the photoreceptor spacing at the fovea, which ranges from 0.42 arcmin to 0.54 arcmin (mean 0.51 arcmin) (Yoon et al., 2002). This value is equivalent to those obtained with interferometric methods, which are considered to be an accurate approximation of the cone spacing in the center of the fovea (Williams, 1985a; Williams, 1985b). Therefore, it is probable that a rough estimate of the sampling grain of the photoreceptor mosaic was achieved with this AO corrected tumbling E resolution task. If so, the results from the myopic group, MAR of 0.58 arcmin (spectacle magnification adjusted), may predict an

increase in photoreceptor spacing. In retinal units, if this difference is purely a function of retinal changes, these results suggest a difference in the Nyquist limit of the cone mosaic of  $0.62 \mu\text{m}$  (a 28% increase over the emmetropes). It is not clear whether this magnitude of stretching is plausible for the low myopes in this study, however current evidence suggests this is unlikely (Li et al., 2009). Further data on the relationship between photoreceptor spacing and visual performance in myopia is required. Attempts were made to measure foveal cone spacing in these observers with low coherence infrared light, but the cones were not resolved at the center of the fovea. The relationship between cone spacing and visual performance across the fovea, including areas near the foveal center where cones are well resolved is the focus of Chapter 4. If photoreceptor spacing is similar in emmetropia and myopia, then there must be some post-receptoral differences in sensitivity between myopes and emmetropes, either within the retina, or at a later stage in visual processing. This neural insensitivity might be considered a sub-clinical form of amblyopia.

### **3.6 Conclusions**

1. Observers with low myopia perform worse than emmetropes in a visual resolution task after AO correction in both angular (MAR) and retinal (CFS) units.
2. Residual optical aberrations after AO correction do not limit visual resolution in emmetropia or low myopia.
3. There is no difference between high order aberrations in low myopia and emmetropia.
4. Retinal and/or cortical factors limit visual resolution in low myopia after AO correction.

## **Chapter 4**

### **The Relationship Between Visual Resolution and Cone Spacing in the Human Fovea**

#### **4.1 Abstract**

Visual resolution decreases rapidly outside the foveal center. The anatomical and physiological basis for this reduction is unclear. Neural sampling of the retinal image is thought to limit human visual resolution at all locations in the visual field except the central fovea, where optical aberrations usually impose a fundamental limit. When aberrations are minimized it is thought that the spatial sampling limit of the cone mosaic limits resolution at the center of the visual field while the spatial sampling limit of the mosaic of midget retinal ganglion cells limits visual resolution in the periphery. This is because cones in the central retina are thought to have a so-called “private line” through the midget bipolar cell to midget retinal ganglion cell network, preserving the resolution afforded by cone spacing across the central retina. In the periphery, signals from multiple cones converge on mRGCs, compromising resolution and so at some eccentricity visual resolution no longer matches  $N_c$  but matches the Nyquist limit of the mosaic of midget retinal ganglion cells ( $N_{mRGC}$ ). However, the eccentricity at which multiple cones begin to converge on single mRGCs is unclear and consequently the relationship between visual resolution and the sampling limit of the foveal cone photoreceptor mosaic remains unknown. Combined psychophysical testing and real-time retinal imaging in AOSLO simultaneously measured the minimum angle of resolution, the cone spacing, and the precise location and motion of the stimulus across the retina. This study shows that cone spacing limits resolution in a much smaller area of the visual field than previously thought. Only at the precise foveal center did visual resolution closely match estimates of  $N_c$ . Across the fovea, resolution fell off much more rapidly than predicted by  $N_c$  and more closely matched  $N_{mRGC}$ .

#### **4.2 Introduction**

Since Wertheim’s classic study it has been known that visual resolution decreases rapidly outside the center of the fovea (Wertheim, 1894). Neural sampling of the retinal image plays an important role in limiting human visual resolution at all locations in the visual field except the fovea, where optical aberrations usually impose a fundamental limit (Enoch et al., 1973; Green, 1970; Marcos et al., 1997; Thibos, Cheney, & Walsh, 1987; Williams et al., 1987; Campbell et al., 1965; Weymouth, 1958). When aberrations are minimized, the instantaneous postreceptoral information is believed to be limited by the spatial sampling of the cone photoreceptor mosaic in the fovea and possibly beyond (Enoch et al., 1973; Green, 1970; Marcos et al., 1997; Thibos et al., 1987; Williams et al., 1987). To the first order, this limit can be considered to be  $N_c$ . Foveal cones each connect via a cone bipolar cell to at least two RGCs and since the majority of the RGCs in the central retina are of the midget class, it is presumed that each cone in the central fovea connects to both an ON- and OFF-center mRGC (Curcio et al., 1990b; Dacey, 1993). This is the so-called “private line” hypothesis (see Chapter 1), which forms the basis of the argument that cone spacing should limit resolution wherever this retinal circuitry is in place (Polyak, 1941). At some point outside the fovea, signals from multiple cones converge onto single mRGCs, compromising resolution, and thus at some point visual resolution no longer matches  $N_c$  but instead matches  $N_{mRGC}$ .

The eccentricity where convergence in the mRGC network begins is not clear, with anatomical evidence suggesting between 3.5 degrees to 6 degrees from the foveal center (Curcio et al., 1990a; Dacey, 1993; Kolb et al., 2003; Wässle et al., 1989; Wässle et al., 1990).

Psychophysical studies which sought to compare  $N_c$  to visual resolution vary considerably, with estimates of the match between  $N_c$  and resolution persisting to anywhere from 2 degrees to 10 degrees from the foveal center (Enoch et al., 1973; Green, 1970; Marcos et al., 1997; Merigan et al., 1990; Thibos et al., 1987; Williams et al., 1987). The sampling theory of vision suggests that it is neural spatial sampling of the retina that limits resolution across the visual field (see Chapter 1). According to this theory spatial information is encoded by the identity of stimulated RGCs (Thibos, 1998). Evidence that human visual resolution is sampling limited at the center of the fovea comes from the perception of aliasing distortions by observers viewing supra-Nyquist frequency grating stimuli (see Chapter 1) (Byram, 1944; Campbell et al., 1965; Charman et al., 1997; Williams, Sekiguchi, & Brainard, 1993; Williams, 1985a; Williams, 1986; Williams et al., 1987). However, the relationship between visual resolution and  $N_c$  across the visual field remains unknown. Table 1 summarizes the findings from the anatomical and psychophysical literature and shows that there is large variability in the evidence obtained through different methods.

Eccentricity	Reference	Source
6	Dacey (1993)	Anatomy (human, 46 eyes)
3.5	Curcio & Allen (1990)	Anatomy (human, 8 eyes)
7	Kolb & Marshak (2003)	Anatomy (human & monkey, several)
3-4	Wässle, Grünert, Röhrenbeck, & Boycott (1990)	Anatomy (monkey, 3 eyes)
2	Green (1970)	Psychophysics (human, 2 subjects)
2(FT), 7(JE)	Enoch & Hope (1973)	Psychophysics (human, 2 subjects)
10	Thibos, Cheney, & Walsh (1987)	Psychophysics (human, 3 subjects)
10	Williams & Coletta (1987)	Psychophysics (human, 3 subjects)
≥1	Marcos & Navarro (1997)	Psychophysics (human, 4 subjects)
10	Merigan & Katz (1990)	Psychophysics (monkey, 2 subjects)

**Table 1| Eccentricity to which so-called “private-line” between cones and mRGCs is thought to persist.** The eccentricity at which convergence in the mRGC mosaic begins is unclear. Anatomical evidence suggests between 3 and 7 degrees, while psychophysical estimates put the estimate at anywhere between 2 and 10 degrees.

The large variability in psychophysical investigations stems in part from the difficulty in directly measuring both  $N_c$  and optically optimal visual resolution in the same individuals (Marcos et al., 1997; Williams et al., 1987), forcing comparisons of resolution measurements with sampling limits derived from different eyes, primarily from histological reports (Enoch et al., 1973; Green, 1970; Thibos et al., 1987). It is now well established that cone spacing, especially at the center of the fovea, is highly variable between individuals (Curcio et al., 1987; Curcio et al., 1990b), making these comparisons susceptible to error. The AOSLO (Roorda et al., 2002b) overcomes these limitations, allowing simultaneous measurement of the minimum angle of resolution (MAR), the cone spacing, and the precise location and motion of the stimulus across the retina.

To examine the relationship between  $N_c$  and MAR across the fovea, an AOSLO (Roorda et al., 2002b) was used to project an adaptive optics (AO) corrected tumbling E stimulus onto the retina at several locations within the central fovea ( $0\text{-}2.5^\circ$  from the foveal center (Polyak, 1941)) of five observers. AO minimizes blur by measuring ocular aberrations and compensating for them with an adaptive element, improving optical quality for imaging (Roorda et al., 2002b) and high resolution stimulus delivery (Liang et al., 1997; Poonja et al., 2005; Roorda et al., 2002b; Rossi, Weiser, Tarrant, & Roorda, 2007; Yoon et al., 2002). As shown in Chapters 2 & 3, AO correction significantly improves visual resolution, reducing the MAR at the preferred retinal locus of fixation (PRLF) by ~33% in normal observers (Liang et al., 1997; Rossi et al., 2007; Yoon et al., 2002). For this study, resolution was examined across the fovea, including areas outside the foveal center where continuous arrays of cone photoreceptors were unambiguously resolved, allowing  $N_c$  to be measured directly. A laser source with a wide optical spectrum allowed images to be obtained closer to the foveal center than previously possible in the studies presented in Chapters 2 & 3. Where cones were well resolved, AOSLO imagery was used to precisely localize all of the cones that interacted with the stimulus over the course of psychophysical testing. This information was combined with cone spacing measurements obtained from the AOSLO imagery to compare  $N_c$  and MAR at resolution test locations. A model of mRGC density was used to compare resolution to estimates of  $N_{mRGC}$  across the fovea.

### 4.3 Methods

#### 4.3.1 Subjects

Two experienced observers (S1 & S2) and three naïve observers (S3-S5) with normal visual acuity participated. S1 & S2 were slightly hyperopic, while observers S3 and S4 were low myopes. Observer S5 was 5 years post-LASIK (previously myopic with -3.75D spherical equivalent refractive error). All observers had normal color vision as assessed by the Neitz Test of Color Vision. Informed consent was obtained in accordance with the procedures approved by the University of California, Berkeley Committee for the Protection of Human Subjects.

#### 4.3.2 Apparatus and Stimuli

The AOSLO (Roorda et al., 2002b) and stimulus presentation method are explained in detail in Chapters 2 and 3 and elsewhere (Poonja et al., 2005; Rossi et al., 2007). Relevant differences will be highlighted. As in Chapters 2 and 3, the stimulus, a Snellen E was presented in negative contrast (appearing as black on a red background). AO correction afforded a high contrast image at all test locations, with contrast increasing with stimulus size and thus eccentricity. Stimulus duration was 1 second (30 frames), exceeding the critical duration for optimal resolution at all test locations (Baron & Westheimer, 1973). Retinal illumination was with a super luminescent diode laser (Superlum BroadLighter, S840-B-I-20); mean wavelength 840 nm and spectral FWHM of 50 nm. Field size was 48 arcmin (V) x 60 arcmin (H) for all locations and subjects except for the PRLF of S4 and S5 which was 24 arcmin (V) x 30 arcmin (H); retinal illuminance was ~2.1 and ~2.7 log Trolands (Wyszecki et al., 1982) for the two field sizes, respectively.

#### 4.3.3 Psychophysical Testing & AOSLO Imaging

The psychophysical test was the same as described in Chapter 3. Each observer was tested at retinal locations temporal to the PRLF; one (S4) was also tested at superior, inferior and nasal locations. A video of the retina was acquired on each trial, encoding the exact location of

retinal stimulation. As in Chapter 3, threshold estimation was performed by QUEST (Watson et al., 1983) with threshold set at the 82.5% correct level. A few initial thresholds for subject S2 were determined after 100 trials; since the threshold changed little after ~40 trials, all subsequent measurements were obtained with 60 trial runs. This minimized experiment duration, observer fatigue and light exposure. Only two measurements were obtained for S5 at the most eccentric test location; all other thresholds shown are the average of 3-6 measurements.

#### 4.3.4 Image Analysis

To build continuous maps of the retinal mosaic across all test locations, several videos were acquired prior to psychophysical testing. The field size and other imaging parameters were the same as those listed above for the psychophysics portion of the experiment. The PRLF was imaged first and then a fixation target was moved to image neighboring regions. In this way, a map of the photoreceptor mosaic was built up, extending temporally from the PRLF out to between 2 and 3 degrees, depending upon the observer. Videos were stabilized at 480 Hz using custom map seeking circuit (MSC) based algorithms implemented in C++ (Arathorn et al., 2007) or at the frame rate (30 Hz) using custom written FFT-based methods in MATLAB. Stabilized videos were averaged to produce high signal to noise ratio images. Several of these high S/N images, taken at the same retinal location at different times, were then registered in another custom MATLAB program which calculated the displacement and rotation between images. These images were then summed and normalized to give even higher signal to noise ratio images.

These images also had the advantage of removing distortions due to reference frame selection. A drawback of the MSC algorithm stabilization method is that even stabilized images will contain distortions from the reference frame used to stabilize the image. As the reference frame is different for each stabilized video, averaging the resulting images from several stabilized movies has the effect of minimizing differences due to distortions in the reference frame. In many cases this final step of processing was unable to correlate images created from different videos, as the small distortions introduced from the differing reference frames resulted in images which differed too much to be correlated with the simple FFT based cross-correlation method used to calculate the translational and rotational differences between images. In those cases where this method was successful, the best images of the retina were revealed. High signal to noise ratio images were then combined into large montages manually in Photoshop (Adobe Systems, Inc., San Jose, CA, USA). These large retinal mosaic images were then used to localize the center of each resolved cone using a combination of automated (Li & Roorda, 2007) and manual methods.

#### 4.3.5 Cone Localization

To compute cone spacing and cone density and to explore the arrangement of the cones in the photoreceptor mosaic, the location of each well resolved cone in the retinal map was determined. Thousands of cone positions were determined for each subject. Cone positions were found by first applying an image processing algorithm in MATLAB to several regions of the photoreceptor mosaic (Li et al., 2007). Rectangular subregions of retinal mosaics were selected for cone counting, which contained the foveola and horizontal temporal test locations. These images contained too much variation in spacing to be processed simultaneously by the automated cone counting algorithm because large variations in spacing affected the ability of the filtering mechanism to reject false cones. Each mosaic was therefore typically divided into

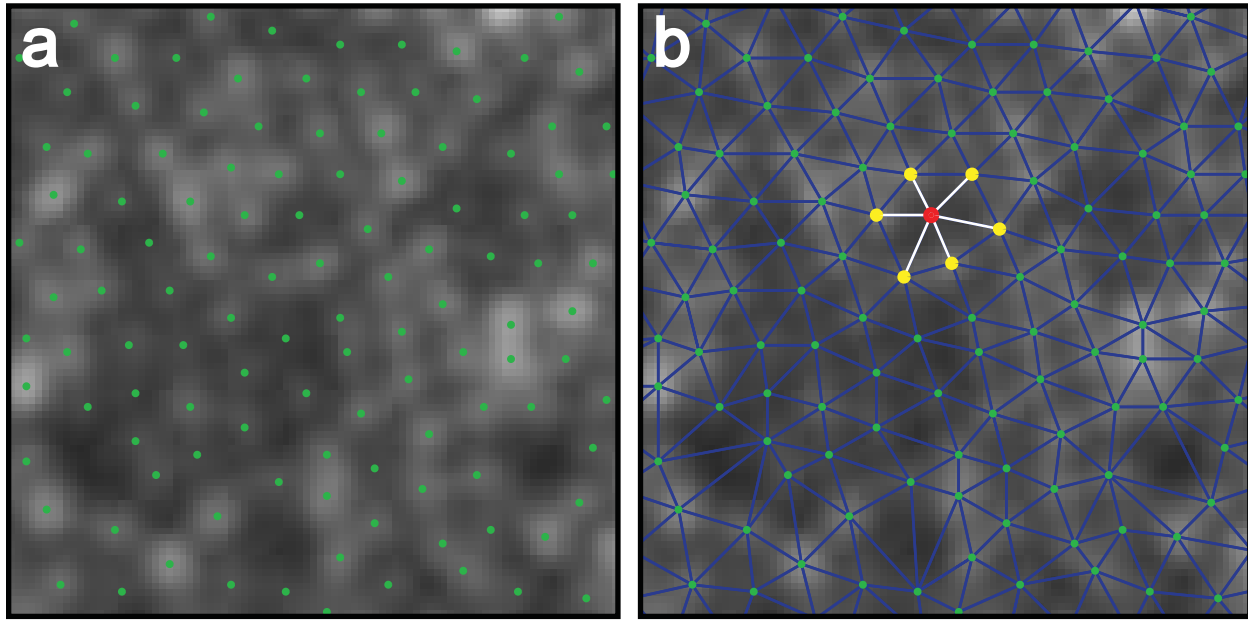


**Figure 23| Cone positions are triangulated to find cone neighbors for spacing and regularity measurements.** a) A small patch of retina from the 1.06° test location for observer S1 with cone positions marked with green circles. b) Triangles shown in blue are the result of the Delaunay triangulation. A single cone is marked in red with its neighbors marked in yellow. The white line segments mark the distances between the cone (red dot) and its neighbors (yellow dots). The mean length of these line segments is the inter-cone distance (ICD).

regions of between 0.25-1 degree<sup>2</sup> and processed section by section until cones were localized algorithmically for the entire area of interest. The output of the algorithm resulted in the x, y location of the pixel that defined the center of each cone. If the cone center resided between two pixels, then the nearest pixel was chosen. Errors in cone locations, usually caused by variations in the brightness of individual cones, were modified manually in a MATLAB GUI, until most of the cone position errors were corrected. The x, y positions were then used to generate a binary image, which had ones at the location of a cone and zeros elsewhere.

Binary images of each analyzed patch were then reassembled in Photoshop as layers on top of the continuous retinal mosaic for each observer. Cone locations found by the algorithm were visually inspected and errors were corrected by manually editing the binary image. This is similar to the manual methods used to localize cone centers from histological sections (Hirsch et al., 1987; Yellott, 1983). Cone locations nearest to the foveola, where the visualization of the cones was most difficult, were the hardest to determine using the automated method, and it is these areas that required the most manual cone localization. It is also these areas that are most sensitive to errors in the manual method of cone localization, as the pixel size to cone size relationship was closest. A 2.4 μm foveal cone for example, would be only about four to five pixels across (depending on the size of a pixel in microns), making the error in finding its center relative to its spacing greater. Many hundreds of cones had to be localized manually and many hundreds of false cones were deleted manually or had their location modified in Photoshop. Due to the fact that brightness of individual cones varies (Pallikaris, Williams, & Hofer, 2003), there were likely locations in the retinal imagery where there were cones that were not localized using either method. Care was used in determining cone locations manually, but the determination was subjective and there were likely more errors in cone locations near the foveal center where the

cones were poorly resolved and tend to be less reflective on average.

Following cone localization, each cone's spatial relationship with its neighbors was quantified. All of this processing was done in MATLAB using custom software and is outlined in Figure 23. First, a Delaunay triangulation was performed on the x,y positions of each cone (a small patch of retinal imagery with cone positions marked is shown in Figure 23a). The Delaunay function returned a set of triangles such that no data points were contained in any triangle's circumcircle (blue triangles, Figure 23b). For each cone, the triangulation was searched to find the triangles which that cone was a vertex of. The other two vertices of each triangle to which a cone belonged were two of that cones neighbors. The unique vertices of each triangle to which a cone belonged were all of the x,y positions of the neighboring cones (this relationship is shown in Figure 23b, cones marked in yellow are the neighbors of the cone marked in red). For each cone a list of points was generated which were the neighbors of that cone. It should be noted that using this method for determining the relationships between cones can be problematic at edges of the triangulation.

This was avoided by computing the triangulation over a large area of the mosaic and only using data that fell well within the bounds of the triangulation. For each cone, the distance to each of its neighbors was calculated geometrically (white line segments in Figure 23b). The average distance from a cone to each of its neighbors is the mean center-to-center inter-cone distance (ICD). The size of retinal features was determined using Bennett's adjusted axial length measurement (Bennett et al., 1994), from axial lengths measured optically with an IOLMaster (Carl Zeiss Meditec, Inc., Germany). These measurements were adjusted for magnification effects due to spectacle lens correction of low order aberrations as explained in Chapter 3.

#### 4.3.6 Estimating Cone Spacing at the Foveal Center

For locations at the foveal center where cones were not well resolved, cone spacing was estimated by using simple linear regression analysis of the points between where cones became well resolved and  $\sim 400 \mu\text{m}$  from the PRLF. Examination of the equivalent  $N_c$  for cone densities reported in the literature has revealed that the reduction in cone spacing within this area is approximately linear (Curcio et al., 1990b; Curcio et al., 1987). The data of Curcio (Curcio et al., 1990b) were used to test this method; using those published measurements for the temporal fovea between  $150 \mu\text{m}$  ( $\sim 0.5^\circ$ ) and  $400 \mu\text{m}$  ( $\sim 1.4^\circ$ ) to predict  $N_c$  at the foveal center resulted in an RMS error of  $\sim 0.043$  arcmin. Using more data improved the estimate slightly; using the published measurements between  $100 \mu\text{m}$  ( $\sim 0.35^\circ$ ) to  $400 \mu\text{m}$  ( $\sim 1.4^\circ$ ) resulted in an RMS error of  $\sim 0.041$  arcmin. Decreasing the number of points, using only those between  $200$  and  $400 \mu\text{m}$  resulted in an RMS error of  $0.054$  arcmin. For one observer, S4, estimates were taken from the data points at eccentricities between  $0.7^\circ$  and  $1.4^\circ$ . Estimates of spacing at the PRLF are expected to be accurate to within  $\sim +/- 0.05$  arcmin.

#### 4.3.7 Analysis of Mosaic Regularity

Mosaic regularity was assessed with several simple geometric methods. All assessments were based on the locations of cone centers identified from retinal imagery that were then triangulated using the Delaunay triangulation implemented in MATLAB. As cone neighbors were found for measuring ICD, each neighbor was known. The number of neighbors gives an indication of mosaic regularity, with the expectation that in a triangular packing arrangement each cone should have 6 neighbors. Furthermore, the angle between a cone and each of its neighbors can be calculated, for a perfect triangular lattice of cones the angle between a cone and

each of its neighbors is  $60^\circ$ . Since mosaic regularity over the entire area stimulated during the resolution test is of interest, a larger averaging window was used to assess regularity in the mosaic than was used to calculate spacing. The averaging window for mosaic regularity assessment was  $85 \mu\text{m} \times 85 \mu\text{m}$ , or roughly  $17.4 \text{ arcmin}$ , which is  $\approx \pm 2 \text{ SD}$  of the mean eye position for all observers.

#### 4.3.8 Identifying Stimulated Areas from AOSLO Videos

To find stimulated areas, each video of the stimulus on the retina was stabilized at the frame rate using custom algorithms in MATLAB resulting in a 30 Hz motion trace of eye position. All images from a given run were correlated using FFT based cross-correlation methods in MATLAB and averaged to produce a high signal to noise ratio image of the stimulated area. The resulting image was then used as a proxy between the larger continuous retinal mosaic and the first frame of each individual trial video. This was done because single frames have a much lower signal to noise ratio than the high signal to noise ratio images of the retinal mosaic and correlating single frames with these images proved difficult. To relate each motion trace with the large retinal mosaics: 1) the location of the proxy image on the larger mosaic was determined and then 2) the location of the first frame on the proxy image was found. Both of these steps were accomplished using FFT based cross-correlations implemented in MATLAB. Finally, the location of the stimulus on the first frame was found using the normalized two dimensional cross-correlation functions in MATLAB. In this way the location of the stimulus at the beginning of each motion trace was localized on the larger mosaic. This location data, combined with the motion traces, stimulus sizes, and cone spacing parameters allowed for cone interactions to be modeled (for stimuli delivered during resolution tests) or simulated (to estimate cone interactions for threshold or Nyquist sized stimuli) as explained below. For most observers, motion traces were computed for all thirty frames. A delay between stimulus presentation and recording occurred for two observers (S4 & S5), which resulted in just the final 21-23 frames being available for motion analysis. Some videos from all observers were excluded due to poor quality of the retinal imagery, blinks, or large eye movements. Of 7,580 total trials for all observers, 93.7% were successfully analyzed and localized on the retinal imagery. This data was used to calculate the mean position stimulated at each test location, in addition to a standard deviation in both the x and y directions. These values were used to define an elliptical area in which the stimulus fell at each test location, over which  $N_c$  was averaged for comparison to MAR at test locations.

#### 4.3.9 Modeling Cone Interactions and Mapping Stimulated Cones

To accurately determine cone-stimulus interactions, cone position and spacing data were used to develop a simple model in MATLAB of the spatial sampling characteristics of the retina. Each cone has an associated aperture whose size is based upon the spacing between a cone and all of its neighbors. The shape of the aperture was assumed to be a 2-dimensional Gaussian, with full width at half maximum of 34% of ICD (Williams et al., 1993; Chen, Makous, & Williams, 1993; MacLeod, Williams, & Makous, 1992). For each cone mosaic, defined by the cone positions and spacing information, a digital two dimensional model of the cone apertures was created (shown in Figure 24 for cone positions marked and measured in Figure 23). To examine

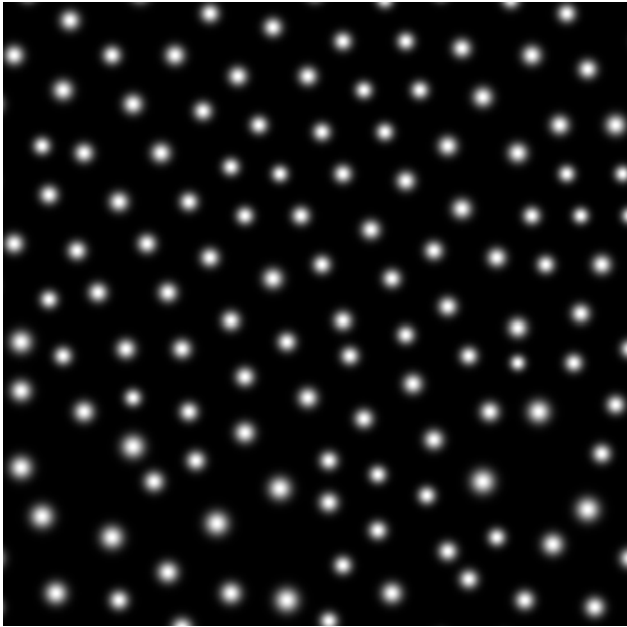


**Figure 24| Model of cone apertures.** A model of the cone apertures created from the cones shown in Figure 1a. Cone apertures are considered to have the shape of a 2D Gaussian whose full width at half maximum is equal to 34% of the ICD. Cone models such as this are used to create cone interaction maps (see Figures 26, 27 & 45) for finding cones stimulated during psychophysical testing and to model the pattern of cone stimulation for threshold sized stimuli (see Figures 32, 33 & 47).

the interaction of the stimulus with the model of cone apertures, the light distribution of the stimulus (Figure 25a) was convolved with the point spread function due to diffraction at 840 nm (Figure 25b) to create a model of the light distribution on the retina (Figure 25c). For each trial, the stimulus was scaled appropriately based upon the actual stimulus that was delivered to the retina. Using the motion and location information obtained from calculated frame rate traces, the motion during each trial was simulated by moving the stimulus with respect to the model of cone apertures, and the pattern of cone interaction was estimated for each frame. For each cone, the light distribution was integrated across the entire cone aperture. This value was then normalized to the degree to which the aperture was filled. If the entire aperture was filled, that cones stimulation was considered to be maximal. In this way cone stimulation maps were created for each observer to determine precisely which cones were stimulated over the course of the psychophysical testing. For areas where the cones were not well resolved, interactions were not modeled on a trial by trial basis. However, models were created to estimate the number of cones

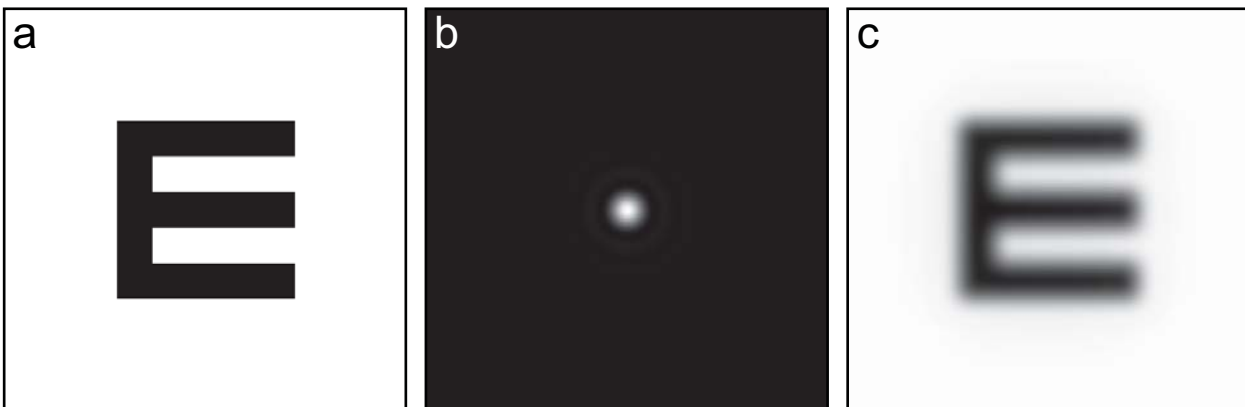


**Figure 25| Stimulus modeling.** The tumbling E stimulus (a) is convolved with the point spread function (b) to model the light distribution on the retina (c).

that interacted with the stimulus. These models were created by using the estimated  $N_c$  for each location to create a perfect triangular matrix that matched the estimated Nyquist limit for that location. This was accomplished in MATLAB using the HEX\_GRID library (Burkardt, 2005).

#### 4.3.10 Calculation of the Nyquist limit of mRGCs

The model of midget ganglion cell receptive field density ( $D_{mgcrf}$ ) in the human visual field from Drasdo and colleagues was used to estimate the Nyquist limit of midget ganglion cell receptive fields ( $N_{mRGC}$ ). Using equation 6 from Drasdo et al. (Drasdo et al., 2007),  $D_{mgcrf}$  was calculated at all test eccentricities for all observers. Parameter values for their general model were used. By dividing  $D_{mgcrf}$  by two at all locations, the density of either the ON- or OFF-center subclass of mRGCs was estimated. For these purposes it was assumed that the ON- and OFF-center sub mosaics were symmetric and tiled the visual field completely at all test locations. It has been suggested that there is considerable asymmetry in the ON and OFF mRGC mosaics in the periphery, but this has not been demonstrated within 5° from the foveal center (Dacey, 1993). Density was converted to spacing between rows of ON- or OFF-center mRGC receptive fields ( $N_{mRGC}$ ) using the following equation:

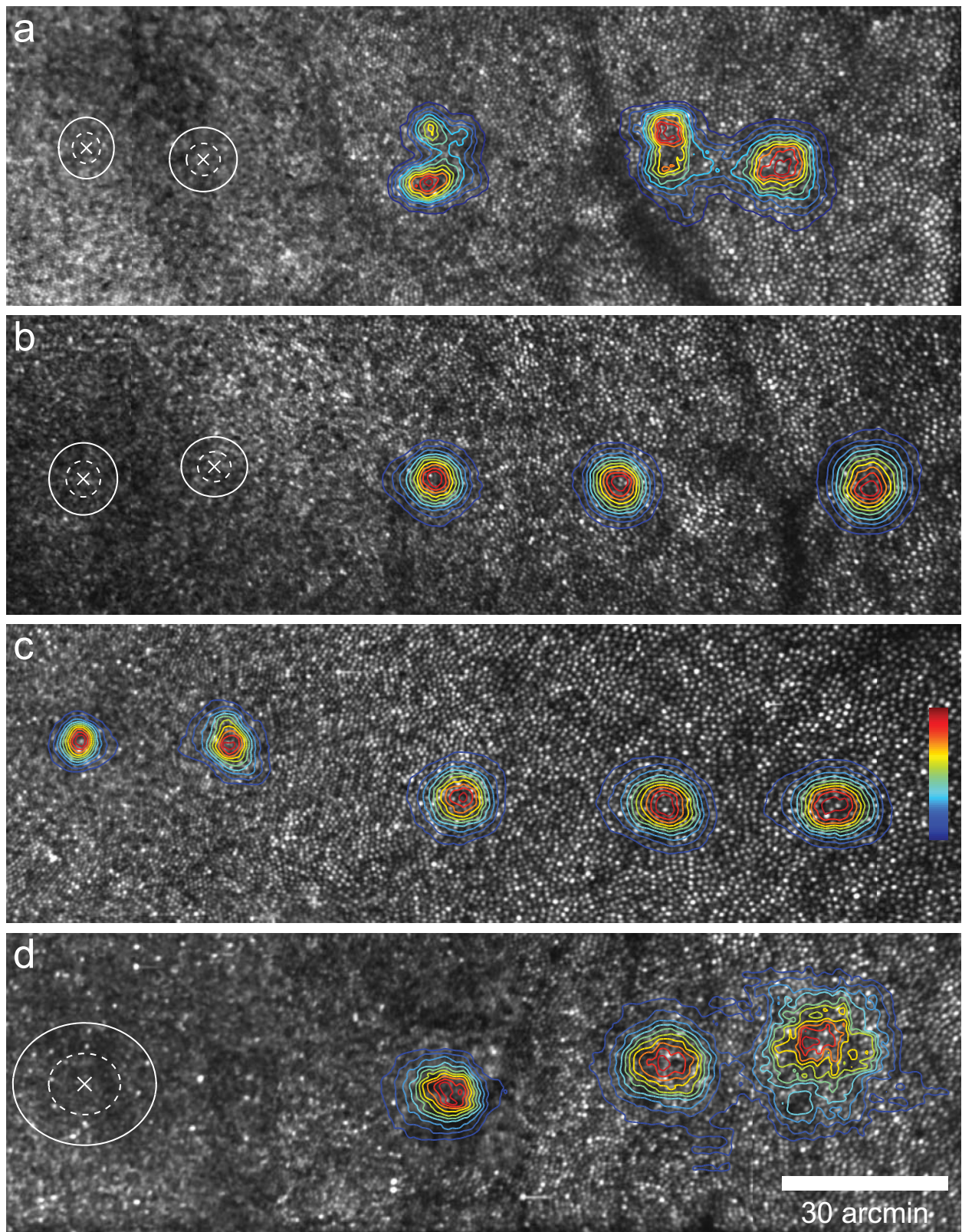
$$N_{mRGC} = \sqrt{\frac{\sqrt{3}}{2 \times D_{mgcrf}}} \quad (3)$$

This conversion assumed that the mRGC receptive fields tile the visual field in a triangular packing arrangement, in the same way as the cone photoreceptors. The value of  $E_2$  for  $N_{mRGC}$  (the eccentricity at which spacing between ON- or OFF- mRGC receptive field centers doubles) predicted from the model of Drasdo and colleagues (Drasdo et al., 2007) was 1.209°.

#### 4.4 Results

Retinal imagery is overlaid with a topographic map of stimulated cones in Figure 26 for observers S1-S3 and S5, and in Figure 27 for observer S4. Where cones were not well resolved in the AOSLO imagery, the mean location of the stimulus over the course of the psychophysical test is marked with an x and one and two standard deviations of 2D stimulus location are denoted with dashed and solid ellipses, respectively. MAR is plotted with respect to eccentricity in Figure 28a. The expected falloff in MAR with increased distance from the PRLF was observed. Fixational variability caused some test locations to deviate slightly from the horizontal meridian (see Figures 26 & 27), so actual linear distances from the PRLF are shown in Figure 28a. The magnitude and rate of reduction in MAR match the performance reported in the literature from studies that measured resolution across the fovea using high contrast laser interference fringes (Enoch et al., 1973; Green, 1970). An important value to note is the  $E_2$  value (the eccentricity in

**Figure 26| Cone stimulation map for subjects S1, S2, S3 & S5.** (Following page) Topographic maps of stimulated cones. a) S1; b) S2; c) S3; d) S5. Cones appear as bright circles arranged in a triangular lattice pattern. Stimulated cones are shown as topographic maps overlaid in color. Color bar shows normalized level of cone stimulation. For the five locations where cones were not well resolved, an X marks the PRLF, with the solid and dashed white ellipses drawn to show  $\pm 1$  and  $\pm 2$  SD of stimulated area, respectively.



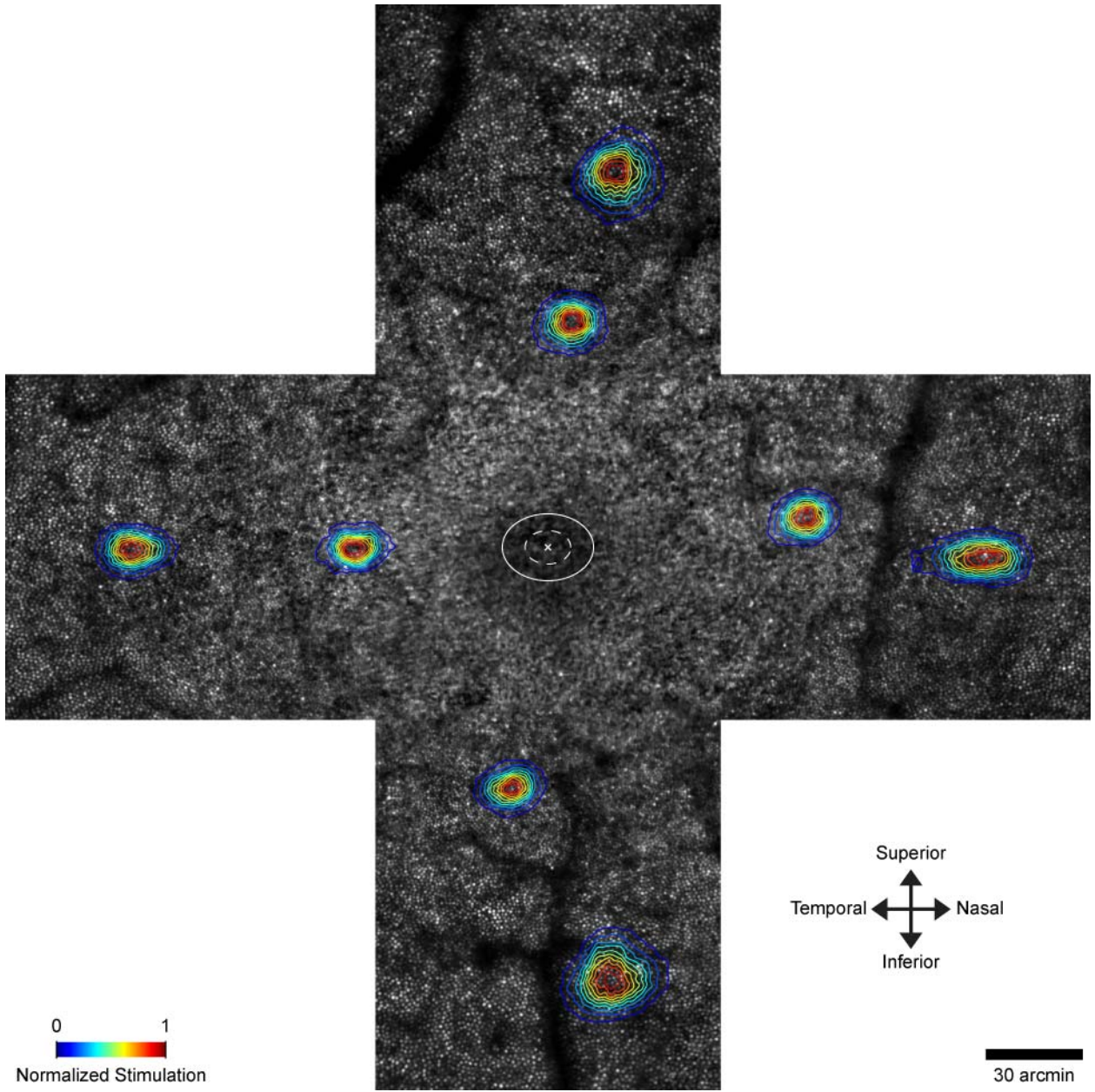


**Figure 27| Cone stimulation map for subject S4.** Symbols are the same as in Figure 26. Compass shows directions in retinal coordinate space; color bar shows normalized level of stimulation.

degrees at which the threshold doubles (Levi, Klein, & Aitsebaomo, 1985)); the mean  $E_2$  of the MAR ( $E_{2m}$ ) for all observers is  $\sim 1.275^\circ$  ( $n = 5$ ).  $N_c$  along the horizontal temporal retina is plotted in Figure 28b. To ease comparison with other published reports (Curcio et al., 1987; Curcio et al., 1990b),  $N_c$  in Figure 28b was calculated over a  $36.5 \mu\text{m} \times 36.5 \mu\text{m}$  ( $\sim 1332 \mu\text{m}^2$ ) sliding window from the PRLF. Where cones were well resolved, ICD was used to calculate  $N_c$ , where:

$$N_c = \frac{\sqrt{3}}{2} \times ICD. \quad (4)$$

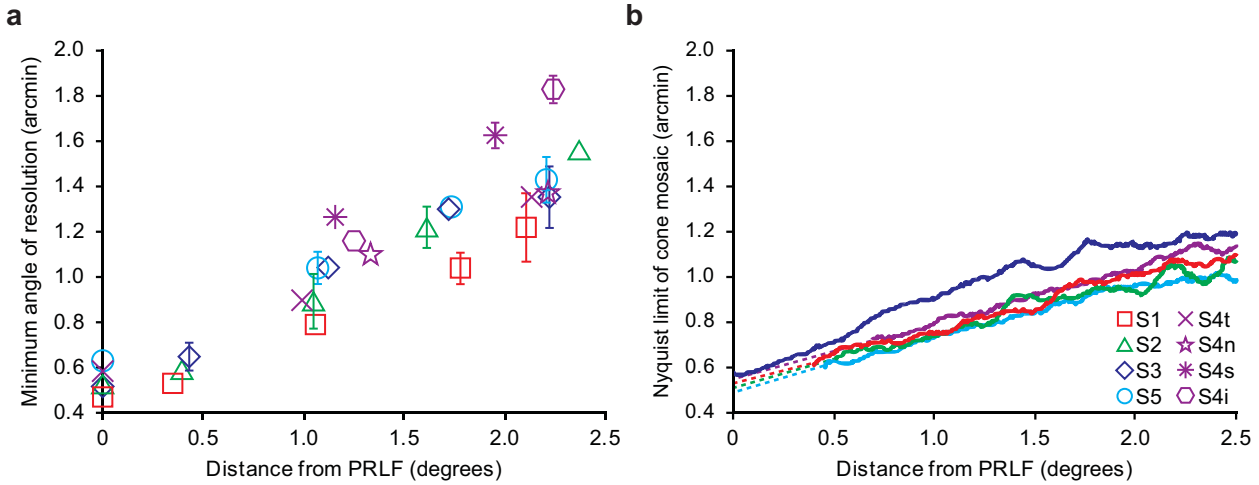


**Figure 28| Visual resolution and the Nyquist limit of the cone mosaic.** **a)** Visual acuity as a function of eccentricity. Symbol relationships are provided in the inset legend. Error bars are  $\pm$ SEM and omitted when smaller than the symbol. **b)** Cone Nyquist limit across the horizontal temporal retina. Lines colored after symbols in (a). Solid lines are measurements; dashed lines are predictions.

This conversion was required because the Nyquist limit for a triangularly packed cone photoreceptor mosaic is based upon the spacing between rows of cones (Snyder et al., 1977). Cones were resolved at the PRLF for one observer (S3), who had the largest cone spacing of all observers examined; cones became resolved for other observers between  $0.14^\circ$ - $0.5^\circ$  from the PRLF.  $N_c$  at the PRLF for these observers (and S2 at  $0.4^\circ$ ) was therefore estimated from retinal imagery as explained in the section 4.3.6. Similar to  $E_{2m}$ ,  $E_{2c}$  was computed (the value at which  $N_c$  doubles); mean  $E_{2c}$  was  $\sim 2.224^\circ$  ( $n = 5$ ), nearly double  $E_{2m}$ .

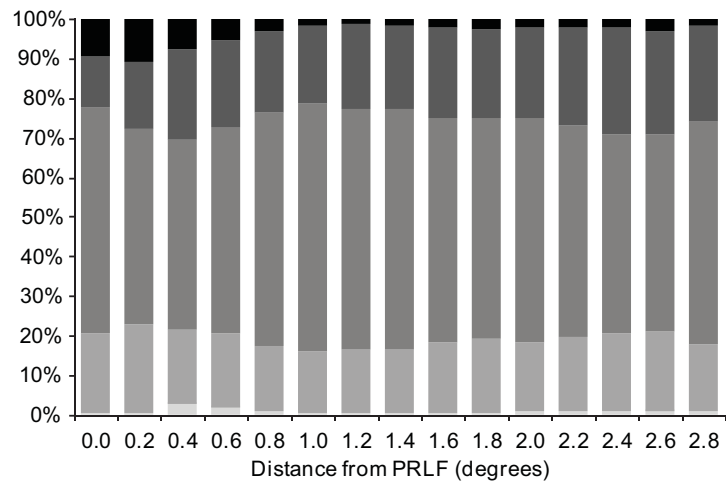


**Figure 29| Mosaic regularity.** The regularity of the mosaic is plotted by showing the percentage of cones falling into different bins depending upon the number of neighbors. The stacked bar at each location is an average of more than one observer. Only two observers are averaged for the bars at 0, 0.2 and 2.8 degrees; four observers are averaged for the bars at 0.4 and 2.6 degrees; all 5 observers are averaged at all other locations. The number of cones having less than 4 neighbors is shown as the lightest grey level, with increasingly darker values representing 5, 6, or 7 neighbors, and with black representing 8 or more neighbors.

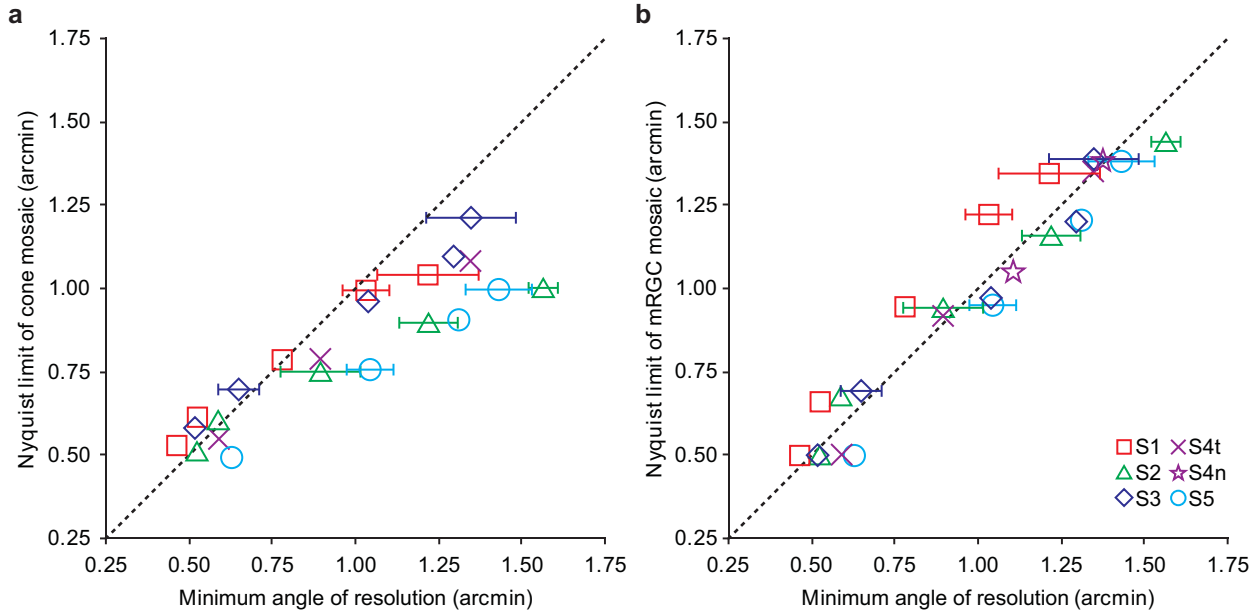


**Figure 30| Visual resolution matches the Nyquist limit of the mRGC mosaic, not the cone Nyquist limit.** **a)** Cone Nyquist limit and MAR for temporal test locations. Cone Nyquist limit is mean of cones within an elliptical area subtending  $\pm 2$  SD of mean stimulated position. Error bars are  $\pm$ SEM and omitted when smaller than symbol. Dashed black line is the 1:1line. **b)** Nyquist limit of mRGC and MAR. Symbol relations are shown in legend inset; only results along horizontal meridian are shown for S4. Dashed black line is the 1:1 line.

At each location where cones were well resolved, the average number of neighbors was 6 ( $SD = 0.7$ ), and the average angle between cones was  $\sim 60^\circ$  ( $SD = 7.5$ ). Another way to consider the regularity of the mosaic is to compare the percentage of cones having six neighbors to those having more or fewer neighbors. This is shown in Figure 29, averaged for all observers across the temporal horizontal retina. On average, most cones have six neighbors (50-60%), the majority of the rest have 5 or 7 (~15-20% each), and only a small percentage have fewer than four or more than eight neighbors. This indicates that there was indeed a fairly regular triangular lattice of cone photoreceptors across test locations and that packing geometry did not change much with eccentricity, in agreement with findings for normal human fovea (Curcio et al., 1992; Li et al., 2007). These findings indicate that the conversion used to calculate  $N_c$  was appropriate across test locations.

MAR is plotted against  $N_c$  at test locations in Figure 30a. MAR agreed well with estimates of  $N_c$  at the PRLF, in accord with findings from previous researchers (Enoch et al., 1973; Green, 1970; Marcos et al., 1997; Thibos et al., 1987; Williams et al., 1987). However, MAR decreased at a greater rate with increasing eccentricity than was predicted by  $N_c$ . If MAR exactly matched  $N_c$ , data points would be expected to fall on the dashed 1:1 line of equality shown in Figure 30a. The slope is the important factor in this comparison, as a slope of 1 demonstrated that MAR was governed by  $N_c$ . Linear regression lines were fit to the data of each observer independently. The mean slope was 0.6355 ( $SD = 0.1058$ ;  $n = 5$ ). This value was significantly different from 1 (t-test; one sample;  $p = 0.00153$ ), indicating that MAR was worse than predicted by  $N_c$  at locations eccentric to the PRLF. Choosing a different threshold for resolution (i.e. 75% vs. 82.5%) would have only resulted in horizontal translations of the regression line fits. Choosing a different metric to represent  $N_c$  would have changed the slope;

for the most extreme case, of a square mosaic, the slope would still only be ~0.73.

Bland-Altman analysis (Bland & Altman, 1986) confirmed poor agreement between MAR and  $N_c$  across test locations (Figure 31). Bland-Altman analysis is a simple and easy to interpret method for assessing agreement between two measurements (Bland et al., 1986). Since the differences between MAR and  $N_c$  vary systematically across the range of measurement (i.e. the difference increases as MAR and  $N_c$  increase) and are proportional to the mean, a logarithmic transformation is appropriate (Bland et al., 1986) and was performed. The Bland-Altman plot clearly illustrates that the difference between MAR and  $N_c$  can be quite large. The mean difference (bias) is 0.0679 on a log scale and the limits of agreement are -0.0766 and 0.2125. Taking the antilog of these limits gives 0.84 and 1.63; since the antilog of the difference between two values on a log scale is a dimensionless ratio (Bland et al., 1986), this shows that the values differ by between ~16% below and ~63% above, demonstrating poor agreement between MAR and  $N_c$ .

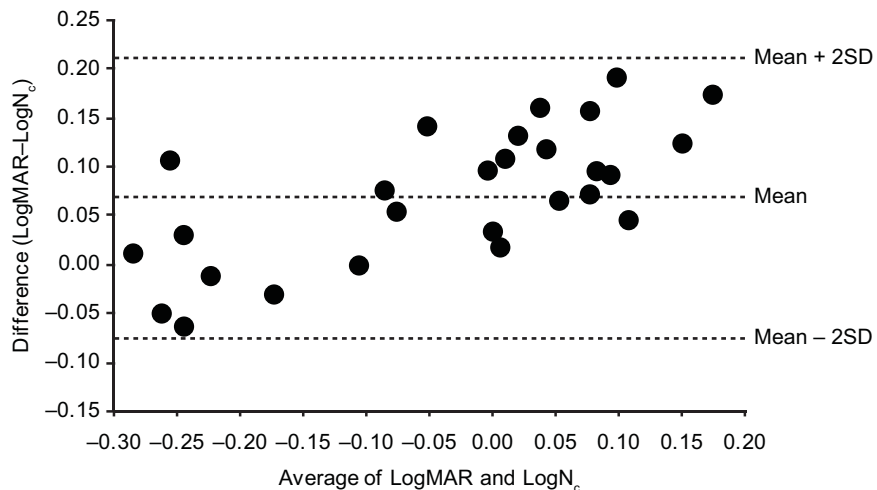


**Figure 31| Bland-Altman Plot shows poor agreement between MAR and  $N_c$ .** Bland-Altman analysis shows that the difference between  $N_c$  and MAR can be quite large. Values differ by between ~16% below and ~63% above.

## 4.5 Discussion

### 4.5.1 Anatomical Considerations and Comparison to mRGC Nyquist Limit

The area where visual resolution most closely matched  $N_c$  (0–0.5°) corresponded well with the anatomically distinct foveola, the nearly flat floor of the foveal pit (Polyak, 1941). This retinal area has several features that are seemingly optimal for high spatial resolution, including: maximum cone density, elongated waveguides, the absence of rods and S-cones, and the lack of overlying vasculature and nerves (Curcio et al., 1990b; Polyak, 1941). However, the discord between resolution and  $N_c$  seen outside the foveola is probably primarily due to differences in retinal circuitry across the fovea. Since the fibers of Henle displace RGCs from the photoreceptors of the central retina to which they form connections, foveal circuitry has historically been difficult to characterize (Curcio et al., 1990a; Dacey, 1993; Drasdo et al., 2007; Kolb et al., 2003; Wässle et al., 1989; Wässle et al., 1990). A careful study of these fibers by Drasdo and colleagues leads to new predictions of mRGC receptive field density across the visual field (Drasdo et al., 2007). Using their theoretical model, the Nyquist limit of the mRGC mosaic (the spacing between neighboring ON- or OFF-center mRGC receptive fields) at the resolution test locations along the horizontal meridian was estimated (see section 4.3.10) and is compared to MAR in Figure 30b. Individual regression lines were fit for each observer. The mean slope was 1.0111 (SD = 0.1105; n = 5), this value was not significantly different from 1 (t-

test; one sample;  $p = 0.8333$ ), indicating that MAR is governed by the Nyquist limit of the mRGC mosaic across the fovea. Another indication that MAR is governed by the  $N_{mRGC}$  is that the  $E_2$  values are quite similar for both MAR and  $N_{mRGC}$ . Cortical mechanisms ultimately utilize the information provided by the earliest stages of visual processing in the retina to make a decision in a visual resolution task; that those decisions so closely match the theoretical sampling limits imposed by the first stages of retinal processing is remarkable.

#### 4.5.2 The Pattern of Cone Stimulation

Further insight into the relationship between MAR and  $N_c$  is gained by examining the pattern of cone stimulation with cone aperture models. Figure 32 plots the cone-stimulus interaction profile at the level of the cone apertures for observers S1, S2, S3 & S5; observer S4 is

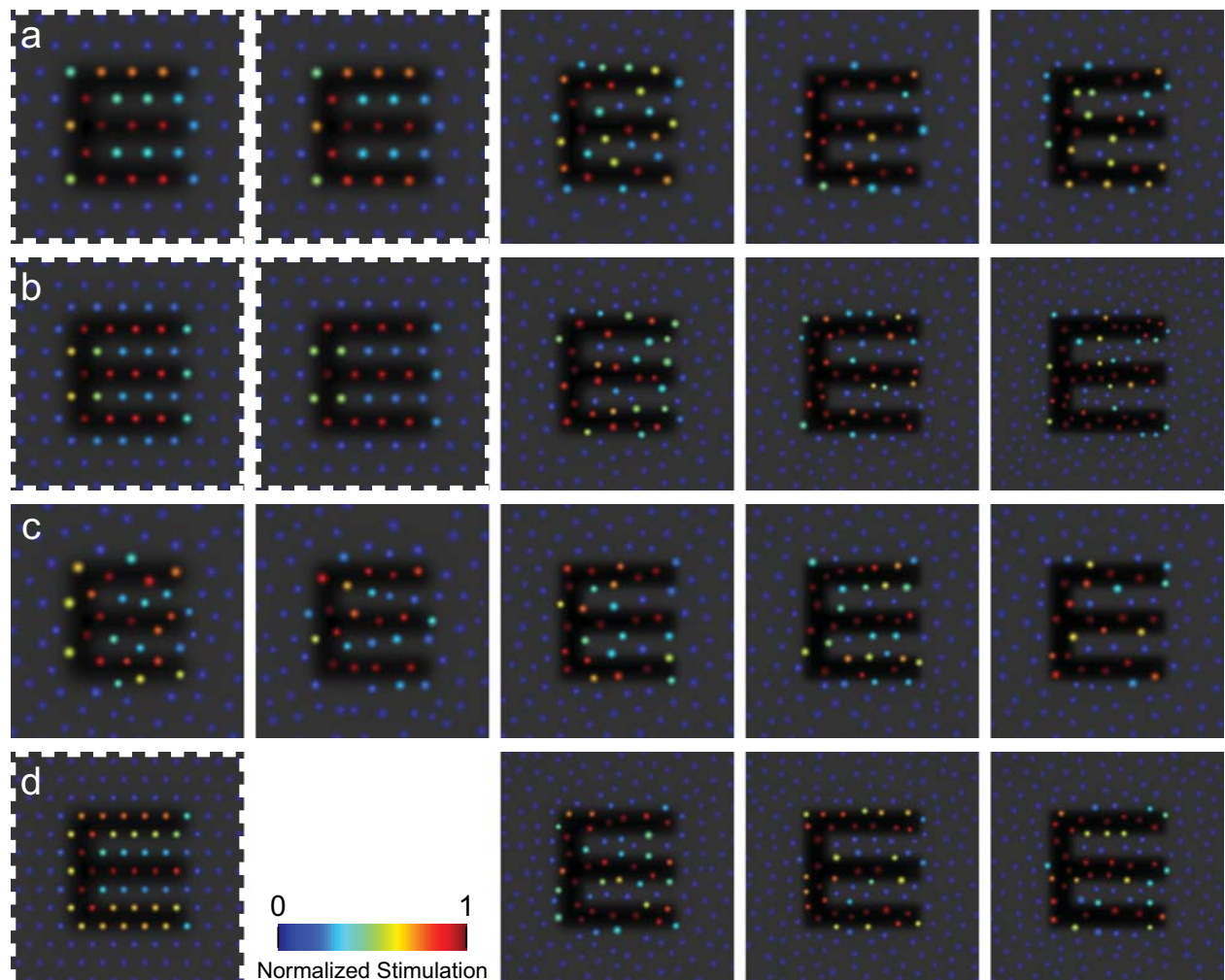


**Figure 32| Cone stimulation patterns of threshold sized stimuli for subjects S1, S2, S3 & S5.** Cone models show the pattern of cone interaction at the center of each test location. S1: (a); S2: (b); S3: (c); and S5 (d). Each panel is scaled to be twice the size of the threshold sized stimulus for that location and observer. PRLF locations are shown in the first column with panels corresponding to the center of each test location in Figure 26. Panels outlined with a dashed line are theoretical triangular sampling arrays; all other panels are based on actual cone locations from retinal imagery. Color bar shows normalized level of cone stimulation (aperture filling), with blue representing cones that were filled with the background imaging light, while red represents cones that were filled with the stimulus.

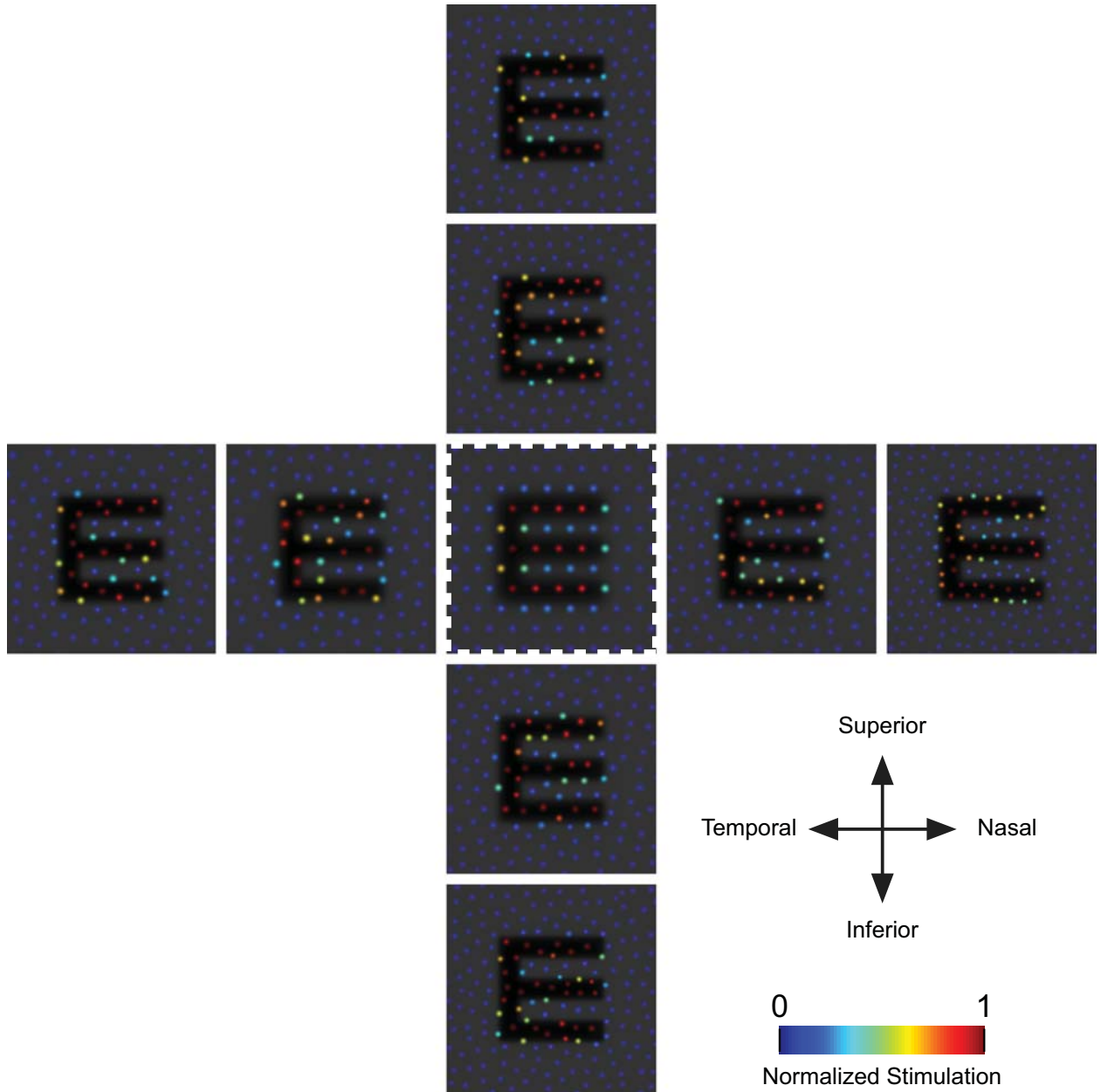


**Figure 33| Cone stimulation patterns of threshold sized stimuli for subject S4.** Cone models show the pattern of cone interaction at the center of each test location for observer S4. Pattern at PRLF (center) is estimated from  $N_c$  for a perfect triangular lattice (outlined with dashed line). Compass shows directions in retinal coordinate space; color bar shows normalized level of stimulation in the same way as Figure 32.

shown in Figure 33. All panels are scaled to the size of a threshold sized stimulus, so the pattern of cone interactions changes in each panel, but the size of each stimulus appears constant. This allows cone-interactions to be examined without having to consider the differences in stimulus size (as was done in Figures 9 & 19). The model of the light distribution is overlaid as a transparency mask on top of each pattern. For the six locations where cones were not well resolved in the retinal imagery (PRLF of observers S1, S2, S4 & S5, and  $\sim 0.375^\circ$  locations for observers S1 & S2), the sampling array was modeled as a perfect triangular array with the

spacing based on the estimated  $N_c$  for that location (as explained in section 4.3.9). This modeling work demonstrates that the number of cones a threshold sized stimulus would encounter increased with eccentricity. This is further evidence that  $N_c$  did not match MAR outside the PRLF.

#### 4.5.3 Comparison to the Results of Green and Enoch & Hope

As already noted, the MAR results obtained in this study are in close agreement with the studies of Green (Green, 1970) and Enoch & Hope (Enoch et al., 1973) which used laser interferometry to measure resolution across the range of test locations examined here (0-2.5°). Figure 34 compares the MAR results from these studies to ours and shows that they are in good agreement across the range of test locations that were examined. Results from Enoch & Hope (Enoch et al., 1973) were converted from the reported “line pair separation” to an equivalent value of MAR, assuming that MAR was equal to  $\frac{1}{2}$  the line pair separation (i.e. a line pair separation of 1 arcmin is equal to a MAR of 0.5 arcmin or a Snellen equivalent of 20/10). Laser interferometry effectively bypasses the normal optics of the eye, allowing for resolution measurements to be obtained that are free from the limitations imposed by the normal optics of the eye (Chapter 1) (Enoch et al., 1973; Green, 1970; Thibos et al., 1987; Williams et al., 1987).

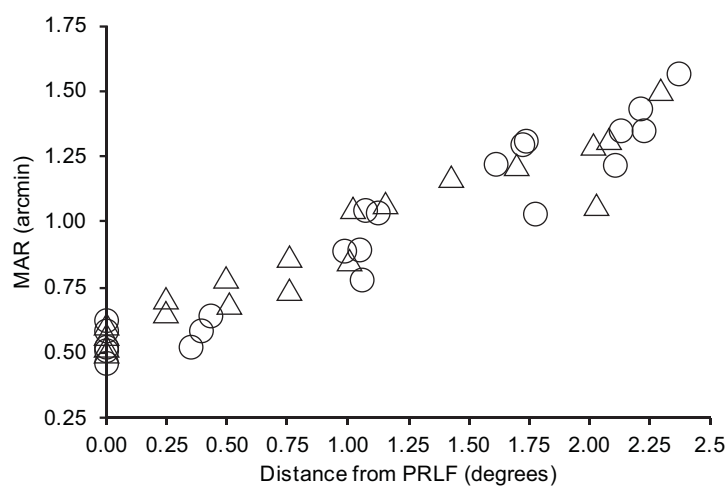


**Figure 34| Tumbling-E resolution measurements matched results obtained with laser interferometry.**  
Interferometry results of Green (Green, 1970) and Enoch & Hope (Enoch & Hope, 1973) (triangles) are plotted with our measurements of MAR (circles).

#### 4.5.4 Stimulus Considerations

If resolution measurements were worse than those obtained by laser interferometry, the discord seen between the MAR and  $N_c$  measurements could have been due to the retinal illuminance of the stimulus, which was beyond the level where grating resolution is believed to be independent of illuminance, but slightly below the level where Landolt C resolution is believed to be optimal (Shlaer, 1937). However, since the resolution measurements were in such good agreement with those obtained using bright high contrast laser interference fringes (Figure 34), a stimulus based explanation for the difference found between  $N_c$  and MAR is highly unlikely. Additionally, the mean MAR obtained at the PRLF of 0.544 arcmin ( $n = 5$ ) was nearly identical to the average MAR of 0.537 arcmin ( $n = 19$ ) obtained in Chapter 3, which used the same instrument and experimental protocol, but delivered stimuli at a wavelength of 658 nm with a much brighter retinal illuminance (6.8 log Trolands).

#### **4.5.5 Differences in the Results of Green and Enoch & Hope**

The results of Green (Green, 1970) and Enoch & Hope (Enoch et al., 1973) diverge from each other beyond the range of testing examined in this study, with the two observers in the Enoch & Hope study achieving better resolution than Green's observers at eccentricities beyond  $\sim 3^\circ$  from the PRLF (Enoch et al., 1973). Both studies used estimates of cone spacing from the classic study of Østerberg (Østerberg, 1935) for comparison and drew different conclusions. It should be noted that the peak cone density reported by Østerberg (Østerberg, 1935) at the foveal center is lower than 6 of the 8 eyes examined by Curcio and is more than one SD unit lower than Curcio's mean of 8 eyes between 0.15 mm and 1 mm ( $\sim 0.5^\circ$  to  $\sim 3.5^\circ$ ), which have become the gold standard for cone density measurements in humans (Curcio et al., 1990b); lower cone density results in higher estimates of cone spacing. Because the results of observer JE fell along the estimates of cone spacing from Østerberg (Østerberg, 1935) out to the most eccentric location tested ( $7^\circ$ ), Enoch & Hope concluded that resolution and cone spacing agreed over this range (Enoch et al., 1973). However, Green's observers diverged from the spacing measurements of Østerberg (Østerberg, 1935) at around 2 degrees so they came to a different conclusion (Green, 1970). This discrepancy is likely to be partially accounted for in differences in methodology, and in particular the size of the test field (Enoch et al., 1973). Enoch & Hope showed that using a small test field (17 arcmin versus 44 arcmin) reduced performance; resolution was better with the larger test field (Enoch et al., 1973). However, the fact remains that there is a large discrepancy in the resolution measurements obtained outside the anatomical fovea.

#### **4.5.6 Comparison to the Results of Williams & Coletta and Thibos et al.**

More recently, the region of equivalence between  $N_c$  and visual resolution has been shown to persist over a greater range, out to about  $10^\circ$  from the center of the fovea. Both Williams & Coletta (Williams et al., 1987) and Thibos et al. (Thibos et al., 1987) also used interference fringes to test vision over a range of retinal eccentricities. Using the method of adjustment, Thibos found resolution agreed with spacing measurements derived from the Østerberg report (Østerberg, 1935) out to  $\sim 10^\circ$  from the foveal center (Thibos et al., 1987). In a second experiment from the same report, Thibos et al. also employed a detection task, whereby observers "reduced spatial frequency until the presence of spatial contrast was evident" (Thibos et al., 1987). With this task, they showed that gratings above the Nyquist limit could be detected (or at least contrast could be detected, as Thibos et al. note that "there was no requirement that the percept be of a grating") when the spatial frequency was much higher than  $N_c$  and also of the Nyquist limit of the RGCs to which they compared their measurements (Thibos et al., 1987).

A similar finding was made by Williams & Coletta (Williams et al., 1987). However, they had previously obtained psychophysical estimates of the  $N_c$  for their observers (Coletta et al., 1987) and so were the first researchers that were able to compare resolution measurements directly to estimates of  $N_c$  obtained for the same observers. Their estimates of  $N_c$  were in reasonable agreement with estimates of  $N_c$  based upon Østerberg (Østerberg, 1935) and Curcio's density measurements (Curcio et al., 1987), but their resolution measurements were much better than predicted by the  $N_c$ , with their observers able to guess the correct orientation of the grating (either horizontal or vertical) when it was  $\sim 1.5$  times the Nyquist limit (Williams et al., 1987).

In a separate experiment in the same report, Williams and Coletta also employed a forced-choice orientation discrimination task to measure contrast sensitivity for a range of spatial frequencies at  $3.8^\circ$  and stated that their results "provide no support for the notion that postreceptoral mechanisms restrict visual resolution to values below the cone Nyquist

frequency” (Williams et al., 1987). They showed that their supra-Nyquist performance persisted to  $\sim 10^\circ$ , and only at their next test location ( $20^\circ$ ) did performance finally fall below the Nyquist limit. They conclude: “thus the present data support the generally held belief that, beyond  $10^\circ$  deg at least, the limitations on visual resolution in the peripheral retina are mainly postreceptoral” (Williams et al., 1987). It should be noted that the results of Williams & Coletta (Williams et al., 1987) and Thibos et al. (Thibos et al., 1987) are supported by evidence from macaque which suggests monkey acuities are in close agreement with cone Nyquist frequencies out to  $\sim 10^\circ$  and ganglion cell Nyquist limits beyond (Merigan et al., 1990).

#### 4.5.7 Field Size Considerations

The field size used for the resolution measurements made by Thibos et al. and Williams and Coletta (Williams et al., 1987) were larger than those used by either Green (Green, 1970) or Enoch & Hope (Enoch et al., 1973). The field size employed by Thibos et al. was  $2.5^\circ$  in diameter at the  $5^\circ$  eccentric test location, and  $3^\circ$  in diameter all other locations (Thibos et al., 1987). As was shown by Enoch & Hope, increasing the size of the test field can improve resolution (Enoch et al., 1973). Increasing field size increases both the number of cycles of the grating that are visible, as well as the length of the fringes (Enoch et al., 1973) but also (and possibly more importantly) results in a larger area of retinal stimulation. It is well known that contrast thresholds improve when the length of bars in a grating or the number of cycles in a grating is increased by increasing the size of the stimulus (Howell & Hess, 1978; Robson & Graham, 1981). Larger stimuli also introduce the possibility that observers may use the edge of the stimulus closer to the foveal center, which falls on cones that are more closely spaced than on the more eccentric edge of the field, to make their determination (Enoch et al., 1973; Williams et al., 1987).

For example, the smallest test field used by Thibos et al. ( $2.5^\circ$  in diameter), at the eccentricity of  $5^\circ$  (Thibos et al., 1987) would stimulate a retinal area (if fixation was perfect) extending from  $3.75^\circ$ – $6.25^\circ$ . Cone spacing increases rapidly in this area, from  $\sim 1.6$  to  $\sim 2$  arcmin in the data of Østerberg (Østerberg, 1935), an increase in spacing of  $\sim 25\%$ , making the comparison here subject to a considerable amount of error. Field sizes used by Williams & Coletta (Williams et al., 1987) were progressively larger at each retinal area, scaled to be  $\sim 80$  times the cone spacing (as measured by Østerberg (Østerberg, 1935)) at each eccentricity (Williams et al., 1987). It is possible that some of the supra Nyquist performance was therefore due to the larger field sizes stimulating areas closer to the foveal center, however, as noted by Williams & Coletta, this hypothesis does not account for much of the discrepancy found between resolution and the Nyquist limit of the cone mosaic (Williams et al., 1987).

#### 4.5.8 Comparison to Findings of Marcos & Navarro

The final psychophysical study it is important to discuss herein is that of Marcos and Navarro (Marcos et al., 1997). This is the only other study aside from the present one that compared objectively measured cone spacing and visual performance in the same eyes. The major drawback of this study that prevents direct comparison to the present results is that they measured visual performance through the normal optics of the eye. Their main finding was that visual resolution matched the Nyquist limit of the cone mosaic across the fovea (they tested only from  $0$ – $1^\circ$ ), except at the precise foveal center, where optical aberrations were the limiting factor (Marcos et al., 1997); this finding is in agreement with the other studies considered (Enoch et al., 1973; Green, 1970; Thibos et al., 1987; Williams et al., 1987). Although it is shown in Figure 7

of their study that all four of their observers performed worse than the Nyquist limit of the cone mosaic at their most eccentric test location of  $1^\circ$ , it is mentioned only briefly in the text, and in that case regarding the significance with respect to one observer (Marcos et al., 1997). It appears that the difference was therefore not significant for the other 3 observers, although there appears to clearly be a trend toward underperformance at  $1^\circ$  from the foveal center. However, since the optical aberrations of the eye were uncorrected, it is impossible to rule out whether optical factors were still limiting performance to some extent at this location, as Green (Green, 1970) showed optical factors to be a limiting factor out to an eccentricity of  $\sim 5^\circ$ .

#### 4.5.9 Different Tasks Utilize Different Mechanisms

Clearly the different tasks employed in these studies utilize different mechanisms, as is evidenced by their drastically different visual thresholds. Williams and Coletta offer an aliasing hypothesis as one possible explanation for the supra Nyquist resolution observed in their study: since aliasing noise below twice the Nyquist frequency is slightly anisotropic, the correct orientation of the grating may be determined even if the signal from the grating alone was too weak for the observer to properly guess the orientation (Williams et al., 1987). The aliasing hypothesis probably provides some explanation for the supra Nyquist performance seen with gratings. Because the stimuli used in this study are blurred by diffraction, and the interference gratings are not, high spatial frequencies will be much higher contrast for gratings than for tumbling E's, increasing the chance that aliasing noise will provide more information about orientation. Furthermore, Williams and Coletta state that: "the sampling theorem correctly specifies the highest frequency possible for image reconstruction without aliasing. However, it does not necessarily prevent an observer from extracting enough critical features of a supra-Nyquist grating to be confident that he sees it" (Williams et al., 1987). This statement is very important and points to an explanation that may elucidate the differences seen between the data of the present study and that obtained by Thibos et al. (Thibos et al., 1987) and Williams & Coletta (Williams et al., 1987).

#### 4.5.10 Changes in Retinal Circuitry Across the Fovea May Explain the Different Thresholds Measured for Extended Gratings and for Tumbling E's Outside the PRLF

Although the model of Drasdo and colleagues (Drasdo et al., 2007) suggests that there are on average fewer than 2 cones per mRGC outside the foveal center, and thus the argument has been made that this circuitry suggests that resolution should no longer match  $N_c$ , it has been shown that there exist mRGCs at eccentricities well beyond the foveola (at  $\sim 7^\circ$ ) which connect to single cones (Kolb et al., 2003). Logic dictates that although one, two or more cones may connect to an ON- or OFF-center mRGC, a fraction of a cone cannot (ie. 1.5 cones). That is not to say that an ON- or OFF-center mRGC cannot be driven primarily by a single cone, with weak input coming from one or more surrounding cones, in fact this has been shown to be the case in the retina of macaque (McMahon et al., 2000; Sincich et al., 2009). However, the Drasdo et al. model (Drasdo et al., 2007) clearly suggests a smooth transition (on average) from single cone centers in the foveola to multi-cone centers in the periphery. For this relationship to exist there must be a fraction of mRGC receptive fields that are driven primarily by single cone input to the center of their receptive fields out to at least the eccentricity where the average rises to 2 cones per mRGC and perhaps beyond. As eccentricity increases, the proportion of single cone center mRGCs decreases, while the proportion having multiple cone centers increases. Information provided by single cone center mRGCs at eccentric locations may thus provide the visual system

with enough information about the critical features of the grating stimulus for an observer to correctly specify the orientation. This could also partially explain the reduction in MAR seen with increased field size, as a larger field would presumably encounter more single cone centered mRGCs (due to the larger area stimulated) and thus provide a stronger signal to the orientation or presence of the grating than would a smaller field. This can be considered to be the retinal analog to the probability summation that likely occurs in the cortex when large stimuli are used (Howell et al., 1978; Polat & Tyler, 1999; Robson et al., 1981).

#### **4.6 Conclusions**

1. Visual resolution at the PRLF closely matches estimates of  $N_c$ .
2. Outside the PRLF visual resolution falls off at a greater rate with increased eccentricity than is predicted by  $N_c$ .
3. Visual resolution outside the PRLF is governed by  $N_{mRGC}$ .
4. The extent of the retina over which the so-called “private line” exists is much smaller than previously thought.

## **Chapter 5**

### **Photoreceptor Development, Visual Resolution, and Retinal Organization in Carriers of Blue-Cone Monochromacy**

#### **5.1 Abstract**

Blue cone monochromacy (BCM) is a rare X-linked condition caused by mutations in the L and M opsin gene array that is characterized by a total loss of L and M cone function in affected males. However, little is known about how the structure and function of the visual system is disrupted in female carriers of this genetic mutation. These carriers generally appear normal on most clinical tests of visual function. However, due to the process of X-inactivation, on average half of the cone photoreceptors in the carrier should be destined to express the mutant opsin gene. Combined psychophysical testing and retinal imaging in AOSLO simultaneously examined cone photoreceptor topography and visual resolution across the fovea in BCM carriers. Retinal imaging revealed that, on average, peak cone density was 50% lower than normal in the carrier. Cones destined to express the mutant opsin gene had no functioning photopigment and degenerated early in development resulting in retinas with relatively normal cone packing but with reduced density and increased spacing relative to normal eyes. Resolution testing revealed that cone loss likely led to loss of mRGCs in the carrier retina, with resolution falling off much more rapidly than predicted by the  $N_{mRGC}$  of normal eyes. However, a similar relationship between MAR and  $N_c$  was seen in the carrier, suggesting that retinal circuitry is largely governed by cone spacing. These results suggest that cone density governs ganglion cell density in development of the human retina.

#### **5.2 Introduction**

##### **5.2.1 Rationale**

Understanding how constraints imposed at the retinal level affect the downstream capabilities of the visual system is important for understanding both normal vision and for understanding vision in disease. As has been demonstrated thus far, by combining psychophysical testing with retinal imaging in AOSLO, insight can be made into the optical, retinal and cortical limits to visual resolution. It was shown in Chapter 2 that resolution testing in AOSLO could reveal a sub-clinical resolution deficit in low myopia. This demonstrated that with AO correction, small differences in visual resolution between otherwise normally appearing observers may be assessed. This technique also allowed the neural limits to visual resolution set by the retina across the human fovea to be determined for normal observers (Chapter 4). It was shown in Chapter 4 that visual resolution across the central retina falls off at a greater rate away from the foveal center than had previously been thought (Rossi & Roorda, 2009), closely matching the  $N_c$  in the PRLF (consistent with results obtained by other researchers) (Marcos et al., 1997; Thibos et al., 1987; Williams et al., 1993; Williams et al., 1983; Williams, 1985b; Williams, 1985a; Williams, 1986; Williams et al., 1987). However, outside the PRLF, resolution decreased at a greater rate than predicted by  $N_c$ , and closely matched  $N_{mRGC}$ . Following the theme throughout this dissertation of testing visual resolution in both normal and diseased eyes, the cone photoreceptor mosaic and visual performance of a group of carriers of a genetic mutation that causes blue cone monochromacy (BCM) is now examined. Little prior knowledge exists as to the structure and function of the visual system in carriers of this genetic mutation; however the existence of the mutation suggests that there should be retinal disruptions. Combined psychophysical testing and retinal imaging in AOSLO allowed insight into not only

the anatomy and physiology of the BCM carrier retina, but the structure, function, and development of the normal visual system.

### **5.2.2 Blue-cone monochromacy (BCM)**

Blue-cone monochromacy is a rare X-linked condition characterized by the total absence of L and M cone function (Pokorny, Smith, Verriest, & Pinckers, 1979; Nathans, Davenport, Maumenee, Lewis, & Hejmancik, 1989; Sharpe, Stockman, Jägle, & Nathans, 1999). BCM is a consequence of mutations in the L and M opsin gene array, which are highly homologous and reside in a head-to-tail tandem array within the X chromosome (Nathans, Thomas, & Hogness, 1986). Two classes of mutations in the L and M opsin gene array have been shown to result in most cases of BCM (Nathans et al., 1989). In ~40% of cases, a normal L and M opsin gene array is inactivated by deletion in the locus control region (LCR) (Gardner et al., 2009; Nathans et al., 1989). The LCR, located 5' of the L opsin gene transcription initiation site, is essential for expression of both the L and M opsin genes (Nathans et al., 1993; Wang et al., 1992). In ~60% of cases a two step mutation mechanism causes BCM, whereby homologous recombination first eliminates one of the genes in the array and then a point mutation deactivates the remaining gene. A small number of BCM cases have also been shown to occur as a result of deletion of an entire exon of one of the genes in the L and M opsin array (Gardner et al., 2009; Nathans et al., 1989). Affected males with BCM have no functional L or M cones and rely solely on S cones for vision under photopic conditions (Pokorny et al., 1979). BCM is characterized by severely impaired color discrimination, poor visual acuity, pendular nystagmus, photophobia, and in many cases myopia (Nathans et al., 1989; Gardner et al., 2009).

### **5.2.3 The BCM Carrier**

Female carriers of BCM are usually indistinguishable from normal observers on most clinical tests of visual function. However, upon careful examination, some carriers have been shown to have abnormal color vision, delayed dark adaptation (Krill, 1977; Spivey, Pearlman, & Burian, 1964), and macular changes outside the normal spectrum (Ayyagari et al., 1999). In addition, some BCM carriers have also been shown to have abnormal cone ERG amplitudes (Spivey et al., 1964; Berson, Sandberg, Maquire, Bromley, & Roderick, 1986) and abnormal fixational eye movements (Gottlob, 1994). Due to the process of X inactivation, which occurs early in development, each cell that is destined to become either an L or M cone selectively inactivates one X chromosome (Pokorny et al., 1979). Since the process of X inactivation is random, the BCM carrier will, on average, inactivate the X chromosome containing the mutation in 50% of cells destined to become L or M cones. Thus a proportion of cells will inactivate the healthy L and M opsin gene array. It is not clear if the cone cells expressing the non-functioning photopigment remain intact, as the outer segment is relatively fragile, degenerating in response to many genetic perturbations (Sharpe et al., 1999). If the inactivated cones do degenerate, the carrier retina will have fewer cones than normal; based on X-inactivation, the average amount of cone loss is expected to be 50% and expected to range from ~10% to ~90%. AO retinal imaging of the carrier cone photoreceptor mosaic should allow us to examine whether cones expressing the mutant opsin gene are lost in BCM and if so, the extent of cone loss and its implications for retinal organization and visual function.

However, the large range of variability exhibited in the normal visual system may make this evaluation difficult. Peak cone density in the normal retina has been shown to range over a factor of 3, from between 100,000 to 330,000 cones per square millimeter (Curcio et al., 1990b).

The relative distribution of L and M cone types also varies considerably among those with normal color vision, ranging between 1:1 to 17:1 (Carroll, Neitz, & Neitz, 2002; Hofer, Carroll, Neitz, Neitz, & Williams, 2005). Best corrected visual acuity is also highly variable and can range over a factor of 2, with the minimum angle of resolution (MAR) ranging from 30 arcsec to 1 arcmin (Westheimer, 2003). Most of the large range in resolution measurements is a function of optical constraints (Chapters 1-4), which can be minimized with AO. Because of the widely varying range of what is accepted as normal, it is often difficult to detect small disruptions in the visual system with most standard clinical tests. This is exacerbated by the fact that the visual system exhibits a high degree of plasticity, with the brain compensating for small disruptions as they occur.

#### **5.2.4 Revealing Differences in the Visual System of the BCM carrier with AOSLO**

It was shown in Chapter 3 that a sub-clinical visual resolution deficit in low myopia (<3.75 D) could be revealed by comparing the AO corrected visual resolution of a group of low myopes with a group of emmetropes (Rossi et al., 2007). It was speculated that some degree of the observed difference between groups could be due to increased cone spacing (and thus  $N_c$ ) resulting from the myopia; however this hypothesis could not be confirmed, as the cones in the central fovea of those observers were too small to be revealed with AOSLO (Chapter 3). Although BCM carriers appear within the normal range when tested with standard clinical resolution tests, AO corrected resolution testing may be sensitive enough to reveal a functional deficit in visual resolution compared to normal observers, just as it was for low myopia in Chapter 3. Psychophysical resolution tests at foveal locations away from the preferred retinal locus of fixation (PRLF) can further reveal differences that may exist downstream of the photoreceptors. AO imaging will examine the fate of non-functional cones expressing the mutant photopigment gene and provide insight into the development of the carrier retina.

#### **5.2.5 Hypothesis Concerning the BCM Carrier Retina**

If carrier retinas exhibit lower cone density than normal, it can be concluded that the cones that inactivated the healthy cone photopigment gene degenerated. The anatomical appearance of the retina and topographical arrangement of the cone photoreceptors should allow insight into whether this degeneration occurs, and may indicate whether this degeneration occurs early or late in development. If the non-functional cones degenerate, and do so early in development, a relatively normal appearing retina should be observed, with closely packed cone photoreceptors arranged in a fairly triangular lattice, but with fewer total cones than found in normal retina. Fewer cones will result in reduced cone density and increased cone spacing relative to normal. This would indicate that the non-functional cones degenerated early, before receptor migration, because the normal functional cones would then migrate to tile the retina completely. Alternatively, if the degeneration happens late in development, or if the non-functional cones do not degenerate, AOSLO imaging should reveal a retinal mosaic that appears much differently. Since the non-functional cones would not have a normal outer segment, their optical properties would be greatly affected and would not be expected to waveguide as normal cones do (Enoch, 1963). Since the waveguide nature of the cones is the foundation for the retinal images obtained with AOSLO (Roorda et al., 2002a), cones that do not waveguide would be expected to appear as dark spaces between the bright functional cones in the retinal imagery. Thus gaps would be expected to be observed in the AOSLO imagery of the cone mosaic, corresponding to the positions of the non-functional cones (Baraas et al., 2007; Yoon et al.,

2009). Voronoi analysis of the mosaic can possibly reveal when the degeneration occurred relative to retinal development.

### 5.2.6 Consequences of Cone Loss in the BCM Carrier

Non-functional cones, either lost or remaining, should reduce  $N_c$  and consequently AO corrected MAR. Further insight into the retinal circuitry downstream of the cone photoreceptors may be obtained by comparing  $N_c$  and MAR outside the center of the fovea. It was shown in Chapter 4 that  $N_{mRGC}$  predicted the reduction in visual resolution seen outside the foveola (Rossi & Roorda, 2009).  $N_{mRGC}$  is set by the density of mRGC receptive fields. The transition from  $N_c$  limited visual resolution in the foveal center to  $N_{mRGC}$  limited resolution across the visual field is a consequence of eccentricity-dependent changes in retinal circuitry in the cone to midget bipolar cell to mRGC network. When the ratio of mRGCs to cones is 2 or greater, the expectation is that each cone will have a so-called private line connection to each of an ON- and OFF- centered mRGC, resulting in  $N_c$  limited visual resolution. The density of both mRGC receptive fields and cones decrease with eccentricity, as does the mRGC to cone ratio. When the ratio falls below 2, the centers of mRGC receptive fields begin to receive input from more than one cone. This compromises resolution resulting in the MAR no longer matching  $N_c$  but rather matching  $N_{mRGC}$  (see Chapter 4). Comparing results obtained in Chapter 4 for normal observers to those obtained with BCM carriers will allow insight into changes in this circuitry in the carrier.

### 5.2.7 Consequences for Retinal Circuitry in BCM Carriers

There are at least two possible hypotheses that resolution tests combined with retinal imaging across the BCM carrier fovea should allow us to test. Hypothesis one is that a reduced number of functional cones in the carrier retina will be combined with a normal number of RGCs downstream from the cones. This may be the case if the RGCs developed independently from the cone photoreceptors. The anatomical prediction would then be that the carrier retina would have a higher cone to ganglion cell ratio across the retina than is found in normal eyes. Because this ratio governs the eccentricity at which the transition from  $N_c$  limited resolution to  $N_{mRGC}$  resolution occurs, this hypothesis makes the functional prediction that the transition will occur at a larger eccentricity in the carrier retina than in the normal retina. If cone density were 50% of normal, and mRGC density remained unchanged in the carrier retina (assuming that the proportion of all RGCs that were mRGCs remained similar), the mRGC to cone ratio would not be 2:1 at the center of the fovea, as it is predicted to be for normal eyes in the Drasdo et al. model, but rather 4:1. This would lead to a great deal of redundancy in the mRGC sub-mosaics, and it is not clear if this type of circuitry is physiologically plausible. However, assuming that it is, the ratio of mRGCs to cones would not fall below 2:1 immediately outside the foveal center as it does in the normal retina, but would remain above 2:1 out to an eccentricity of ~5 degrees (where it is 1:1 in normal eyes), falling below 2:1 beyond. Under this scenario,  $N_c$  is expected to match MAR across the range of test locations examined herein (0-2.5° from the PRLF).

Hypothesis two is that a loss of functional cones will be coupled to a concomitant loss of RGCs in the carrier retina. This would be the case if normal RGC development (ie. the total number of RGCs) depended upon normal cone development (ie. the total number of functional cones). The anatomical prediction that this hypothesis makes is that the RGC to cone ratio would be identical to normal across the carrier retina. This hypothesis makes the functional prediction that the transition from  $N_c$  limited resolution to  $N_{mRGC}$  resolution will occur just outside the PRLF in both the normal and carrier retina (assuming that the proportion of all RGCs

that are mRGCs is similar to that found in the normal retina). Furthermore, MAR is not expected to match the estimated  $N_{mRGC}$  from the model of Drasdo because that model is based upon normal mRGC receptive field density, which would be reduced in the carrier.

### 5.3 Methods

#### 5.3.1 Participants

Four observers participated in this experiment (three female BCM carriers, and one normal male myope who served as a control). Each carrier had a large deletion in the LCR region of the L and M opsin gene array as determined through genetic analysis (Carroll et al., 2009). Informed consent was obtained from all participants after the nature of the study was explained verbally and in writing. This experiment was approved by the University of California, Berkeley Committee for the Protection of Human Subjects.

#### 5.3.2 Dual-Beam Imaging & Stimulus Delivery in AOSLO

The AOSLO used in this experiment was different from the system used in the previous studies in Chapters 2-4. This experiment used the second generation microelectromechanical systems (MEMS) deformable mirror (DM) based instrument (AOSLO2), which is explained in detail elsewhere (Zhang, Poonja, & Roorda, 2006; Zhang & Roorda, 2006). This AOSLO has the ability to simultaneously image and stimulate the retina with multiple wavelengths of light and to correct ocular high order aberrations with a compact MEMS-DM. The multi-wavelength capability of the AOSLO was used to project a high contrast AO corrected tumbling E stimulus onto the retina with visible light, while simultaneously imaging the retina with infrared (IR) light. The stimulus was scanned onto the retina in a raster fashion with a 680 nm diode laser while the surrounding retina was imaged with a super luminescent diode laser (Superlum BroadLighter, S840-B-I-20) with mean wavelength of 840 nm and spectral FWHM of 50 nm (this source was identical to the one used in Chapter 4).

Although in principle both AOSLO systems are quite similar, there are many technical differences in the 2<sup>nd</sup> generation AOSLO that are important to note. Scanning was accomplished in an identical way as explained for the previous AOSLO system in Chapter 2, but with the following differences: 480 horizontal scans are completed before the galvanometric vertical scanner shifts the beams upward to begin the next frame; only 16 horizontal scans are completed during the upward scan. Vertical scan amplitude was set with a digital computer control; horizontal amplitude was set manually. Field size was 48' (H) x 54' (V) with the central 20' x 20' optimized to be within the most linear portion of the scan. The central 20' x 20' section consisted of ~8 stimulus lines (or pixels) per arcmin, with linearity over the entire extent to within ~1 pixel. Beam intensity was controlled with acousto-optic modulators (AOM), of which there was one for each laser source (Brimrose Corp., Baltimore, MD). A dual-beam light delivery mode was employed whereby both lasers were modulated to be on during the forward pass and off during the return pass. At those pixel locations within the field where the stimulus was present, the AOM switched both beams off simultaneously.

The retinal illuminance of the 680 nm stimulating light was ~4.5 log Trolands (laser power of 0.7  $\mu$ W over an area of 0.72 deg<sup>2</sup>). The retinal illuminance of the background imaging light was ~2.4 log Trolands (laser power of 160  $\mu$ W over an area of 0.72 deg<sup>2</sup>) (Wyszecki et al., 1982). The stimulating light, although appearing bright to the observer, was far too dim to form an image at the detector, so simultaneous modulation of the imaging beam resulted in a fiducial mark being placed into the IR imagery. This allowed for localization of the exact cones

stimulated during a given trial (after correcting for a translational shift in the focus of each wavelength due to transverse chromatic aberration, see below). Because the visual system is much more sensitive to the stimulating wavelength (680 nm) and adapted quickly to the level of retinal illuminance, the observer could not detect the background IR light or the stimulus fiducial mark.

Since two different wavelengths were used in this experiment, the chromatic aberration of the eye must be considered, a topic that has not been addressed thus far. Transverse chromatic aberration (TCA) caused the visible stimulus and the fiducial mark to be slightly offset, such that the retinal location of the stimulus in the visible wavelength was filled with IR light (see TCA correction, below). This did not interfere with the extremely high contrast of the AO corrected stimulus, because the ratio of retinal illuminance between wavelengths was such that the Weber contrast was approximately -0.99. Observers adapted quickly to the bright field and had no problem performing the task comfortably. Although it was shown in Chapter 4 that normal observers do not perform differently at either wavelength, 680 nm stimulating light was chosen for this study because of the multi-wavelength capability of this system, and to eliminate any possibility of the stimulus being too dim for the BCM carriers to achieve their best performance on the psychophysical test.

### 5.3.3 Threshold Estimation

High-contrast photopic letter acuity was measured using a four alternative forced-choice (4AFC) tumbling E test at the preferred retinal locus of fixation (PRLF) and at several locations along the horizontal temporal meridian of the central fovea (0-2.5°) (Polyak, 1941). For testing of eccentric locations, observers viewed a fixation target off a pellicle beam splitter placed into the AOSLO between the spectacle lenses and first system mirror. Both eyes of one carrier (BCMc1) were tested, while one eye was examined for all other observers (typically the right eye; see table 1). During imaging and psychophysics, the fellow eye was occluded. Test locations were slightly different for each observer, but in most cases were along the horizontal temporal meridian (allowing comparison to normal eyes tested in a previous experiment). Threshold estimation was performed by QUEST (Watson et al., 1983) with threshold set at the 82.5% correct level. QUEST was implemented in MATLAB using the Psychophysics Toolbox extensions (Brainard, 1997; Pelli, 1997). Each threshold measurement was obtained with a run of 40 trials. Each subject was given a practice run at their PRLF, and then between three and six threshold measurements were made at foveal locations along the temporal horizontal meridian. Thresholds shown are the average of all measurements made at each location.

Experiment control was accomplished using the same MATLAB GUI that was developed for the other AOSLO system. Since this software only interacts with the low level software through a custom library developed in C++ few changes were required to implement the same AOM control software used in the studies reported in Chapters 3 & 4 in the MEMS-based AOSLO. Stimulus duration was 500 ms. It should be noted that this stimulus duration is shorter than the 1000 ms trials used in Chapter 4, but identical to the duration used in Chapter 3 (Rossi et al., 2007; Rossi & Roorda, 2009). This duration was chosen because it reduced the amount of light exposure to the retina, decreased total imaging session time (as limited time was available for imaging and psychophysics on these observers), and reduced observer fatigue. Pilot testing with normal observers showed no difference in measured thresholds with the 500 ms duration. Westheimer tested the effect of stimulus duration on visual acuity and determined that resolution acuity improved with durations up to 400 ms and perhaps longer (Baron et al., 1973). The

stimulus duration used herein (500 ms) therefore exceeds the critical duration of all areas tested (Westheimer, 1982).

### 5.3.4 AO Correction of Ocular Aberrations

Low order aberrations were corrected with spherical and cylindrical lenses placed into the system at the spectacle plane (~14 mm from the entrance pupil). AO correction is achieved by measuring the wave aberration of the eye with a Shack-Hartmann wavefront sensor (SHWS) and compensating for it with a MEMS-DM. Wavefront compensation is provided by the 144 actuator MEMS-DM, placed into the system conjugate to the entrance pupil of the eye prior to scanning (Zhang et al., 2006). The MEMS mirror used in this system results in a much more compact optical configuration optimal for clinical deployment, and achieves modest improvements in imaging performance over the previous generation AOSLO (Zhang et al., 2006).

An AO correction was performed at the beginning of each threshold measurement and then again whenever the experimenter (monitoring image quality and RMS wavefront error) or observer (viewing the stimulus) noticed that the image quality had degraded. To ensure that the stimulus was focused on the outer segments of the cone photoreceptors, the DM was used to subjectively refract each subject after AO correction but prior to threshold measurement, as explained previously in Chapter 2 (Rossi et al., 2007). Most subjects required no fixed defocus compensation. Locations were consecutively (not randomly) imaged, due to the requirement of a chromatic aberration calibration for each observer at each test location (explained in detail below). An AO correction was typically stable for around 10-30 trials, depending upon the observer.

### 5.3.5 Imaging of Surrounding Retinal Areas

To build a continuous map of the retina across the areas tested, several videos acquired prior to and during psychophysical testing were combined. For images taken prior to resolution tests, the field size and other imaging parameters were the same as those listed above; retinas were imaged solely in 840 nm light for videos acquired prior to psychophysical testing. The PRLF was imaged first and then the fixation target was repositioned such that overlapping retinal areas could be imaged, extending temporally from the PRLF out to between 2 and 3 degrees, depending upon the observer. The temporal retina was chosen to facilitate comparison to the study of normal observers presented in Chapter 4.

### 5.3.6 Chromatic Aberration Compensation and Measurement

For multiple wavelength imaging in AOSLO, the chromatic aberration of the eye must be carefully considered, as it causes different wavelengths of light to focus at different lateral and axial locations on the retina (Grieve et al., 2006; Wildsoet, Atchison, & Collins, 1993; Thibos, Bradley, Still, Zhang, & Howarth, 1990). To deliver an optimally focused stimulus after AO correction (when stimulating with 680 nm light and imaging the retina with 840 nm light) longitudinal chromatic aberration (LCA), the difference in focus between wavelengths, must be compensated for. This was accomplished through manual adjustment of the 680 nm source in a calibration phase prior to the combined imaging/psychophysics session; published estimates of the LCA of the eye between these two wavelengths were used as a starting point (Grieve et al., 2006). The AOSLO has a dedicated PMT detector for each wavelength, allowing video imagery of the same retinal area to be acquired simultaneously in each wavelength. To accomplish LCA

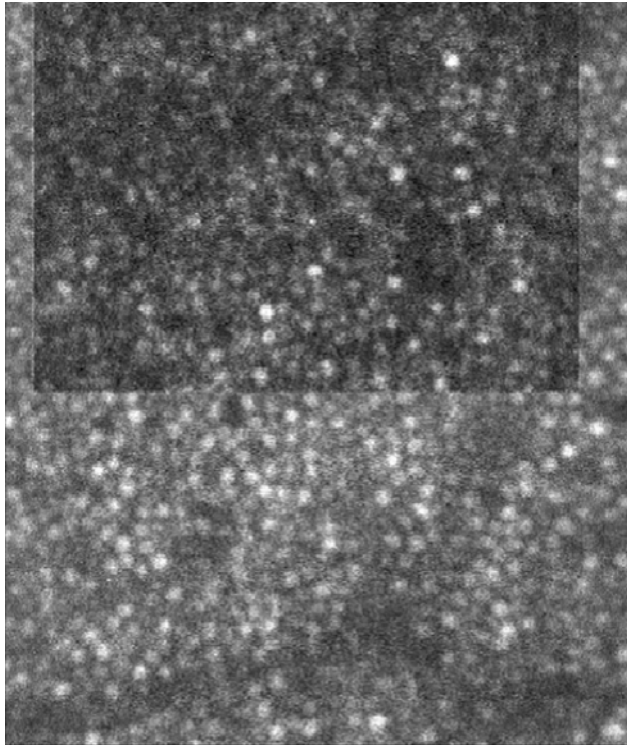


**Figure 35| TCA measurement.** Single frame from TCA calibration video; the upper rectangular region (appearing darker) is imaged with 680 nm light while the surrounding area is imaged with 840 nm light. Upper region position translates with wavelength alternation, allowing TCA to be measured.

compensation, the AO loop was first closed on the 840 nm imaging wavelength alone, bringing that image into sharp focus. The 680 nm source was then activated (at a power level sufficient to form an image at its detector;  $\sim 30\mu\text{W}$ ; retinal illuminance of  $\sim 6.2$  log Trolands;  $< 1\%$  ANSI maximum permissible exposure) (American National Standards Institute, 2000). Both video streams were simultaneously presented to the experimenter on a CRT computer monitor in real time. Using image quality as a subjective metric, the 680 nm source was adjusted to come into sharp focus at the same focal plane as the 840 nm image.

The other type of chromatic aberration, transverse chromatic aberration (TCA) results in a lateral shift of the retinal image formed by each wavelength (Simonet & Campbell, 1990). Since a fiducial mark placed into the 840 nm image was used to precisely determine which cones were stimulated with the 680 nm light, TCA was measured. This was accomplished by acquiring a special calibration video of the retina to use for offline calculation of the transverse shift. A stimulus was delivered to the retina that alternated at 2 Hz between a full field of 840 nm light and a field with a window of 680 nm light within a frame of 840 nm light. This resulted in a video in which a patch of the retinal imagery alternated between wavelengths, while the surrounding area was continuously imaged with 840 nm light. The area alternately imaged with both wavelengths appeared to shift as the imaging wavelength alternated, due to TCA, while the region imaged with the single wavelength appeared normally (a single frame from one of these calibration videos is shown in Figure 35). TCA was calculated from videos using custom MATLAB software that read in the digital video file and prompted the user to manually select first the IR only region, and then the alternating red/IR region. The user then selected the first red frame, which set the phase of the alternation. The video was then stabilized at the frame rate with respect to the IR only region. Stabilization was performed by taking the peak of the FFT cross-correlation function. This resulted in a new video that was stabilized at the frame rate with

respect to the IR imagery. The stabilized video was then reprocessed using the same methodology, but the stabilization area was chosen to be the area that alternated between red and IR. The difference between the two motion traces encoded the TCA shift. Vertical and horizontal shifts were each averaged with respect to the phase of the wavelength alternation. Due to unavoidable errors in the stabilization process that arose due to large eye movements or blinks, the raw TCA traces contained errors. These errors were compensated for by averaging several cycles of the TCA shift and removing those spurious shifts which fell beyond two standard deviations of the mean. The result was two square wave traces (one horizontal and one vertical) which encoded the TCA and thus the translation required to bring the red and IR regions into register. The compensatory translational shifts were then applied to the imagery and displayed to the observer with the two (now overlapping) images alternately presented such that the experimenter could visually inspect the calculated TCA shifts and confirm that the calculated

Subject Code	Eye	Distance from PRLF (degrees)	Horizontal (min)	Vertical (min)
BCMc1	(OS)	0	2.576	0.499
		2.047	2.244	0.748
	(OD)	0	2.305	0.854
		0.941	2.305	0.854
BCMc2	(OD)	0	3.082	1.627
		0.861	2.911	1.798
		2.649	3.767	0.685
BCMc3	(OD)	0	2.752	0.500
		0.864	2.585	0.334
		1.92	2.585	0.417
		2.50	2.585	0.417
CTRL	(OD)	0	2.704	0.082
		1.103	2.377	0.025
		2.439	3.852	0.029

**Table 3| Transverse chromatic aberration.** Measured difference in lateral focus (TCA) between imaging and stimulating wavelengths.

shifts put the two images in register. Measured TCA for each subject imaged is listed in Table 3. The measured TCA was a combination of ocular and system TCA, but is likely dominated (especially in the horizontal direction) by a lateral misalignment between the red and IR light sources. It should be noted that chromatic aberration also causes a chromatic difference in magnification (CDM). The effect of CDM is very small (< 1% between 400 and 700 nm) and considered to be negligible with respect to these results (Grieve et al., 2006; Bennett & Rabbetts, 1989; Zhang, Thibos, & Bradley, 1991; Zhang, Bradley, & Thibos, 1993).

### 5.3.7 Spectacle magnification and the size of retinal features

Spectacle magnification was calculated and applied to all measurements as explained in Chapter 3. Bennett's adjusted axial length method was used to calculate the size of retinal features (Bennett et al., 1994). The only biometric measurement required for this method is the axial length of the eye, which was measured optically with an IOLMaster (Carl Zeiss Meditec, Inc., Germany). Further details on calculations and inherent error estimates are given in Chapter 3. Axial lengths, spherical equivalent of spectacle lenses used during retinal imaging, resulting

spectacle magnifications, microns per degree of visual angle and microns per pixel of retinal imagery are listed in Table 4.

<b>Subject Code</b>	<b>Eye</b>	<b>Axial Length</b>	<b>Spectacle Lenses (SE, Diopters)</b>	<b>Spectacle Magnification (%)</b>	<b><math>\mu\text{m}/\text{degree}</math></b>	<b>Image Resolution (<math>\mu\text{m}/\text{pixel}</math>)</b>
BCMc1	(OS)	22.66	-0.5	99.3	270.278	0.37977
BCMc1	(OD)	22.57	-0.5	99.3	269.111	0.38881
BCMc2	(OD)	22.51	-0.25	99.7	269.295	0.38697
BCMc3	(OD)	23.84	-3.375	95.5	274.606	0.4186
CTRL	(OD)	27.46	-4.25	94.4	316.029	0.48409

**Table 4 | Biometry and Imaging Parameters.** Axial length, spherical equivalent (SE) of spectacle lenses, magnification, distance relations, and image resolution.

### 5.3.8 Post-Processing of Retinal Imagery

Digital video of resolution test locations and neighboring retinal areas were processed using methods described in Chapter 4. In some of the best retinal images, the blind deconvolution function in MATLAB was used to better resolve cone centers near the PRLF. A simple Gaussian PSF was used as the initial PSF for the iterative blind deconvolution process; the size was set to roughly match to the size of the theoretical PSF. This method was useful only when the cones were almost fully resolved and the S/N ratio was very high in the retinal imagery. To ensure that cones were not falsely identified based on amplified noise or other artifacts, deconvolved images were carefully compared to non-deconvolved images and only used to guide the localization of cone centers when they were revealed as a continuous and closely packed array.

### 5.3.9 Measurement of Anatomical Properties of the Cone Mosaic and Determining Stimulated Areas from AOSLO Imagery

Cone positions were localized on the large retinal mosaics using a combination of automated (Li et al., 2007) and manual methods. ICD and  $N_c$  were measured from localized cones using methods described in Chapter 4. Cone density was calculated either directly, by simply counting cone centers that fell within a set area, or by calculating a measurement of density at each cone using the Voronoi diagram. The Voronoi diagram was created in MATLAB. The inverse of the area of each Voronoi polygon gives an extremely local measurement of density (from a single cone) (Curcio et al., 1992). When cone centers fall near the edges of a counting box, cone density will be artificially inflated with a direct counting method. The Voronoi density calculation method reduces these errors. To ease comparison with other published reports and Chapter 4 (Curcio et al., 1987; Curcio et al., 1990b), a  $36.5 \mu\text{m} \times 36.5 \mu\text{m}$  bounding box ( $\sim 1332 \mu\text{m}^2$ ) was used when calculating spacing and density across the horizontal meridian. Mosaic regularity was assessed using a larger  $85 \times 85 \mu\text{m}$  bounding box, to ease comparison with the results obtained for normal observers in Chapter 4. The areas of retinal stimulation were determined using methods described in Chapter 4. As in Chapter 4, for comparing  $N_c$  and MAR at resolution test locations,  $N_c$  was averaged over an elliptical window subtending  $\pm 2$  SD of the position of the stimulus on the retina during the resolution test at that location.

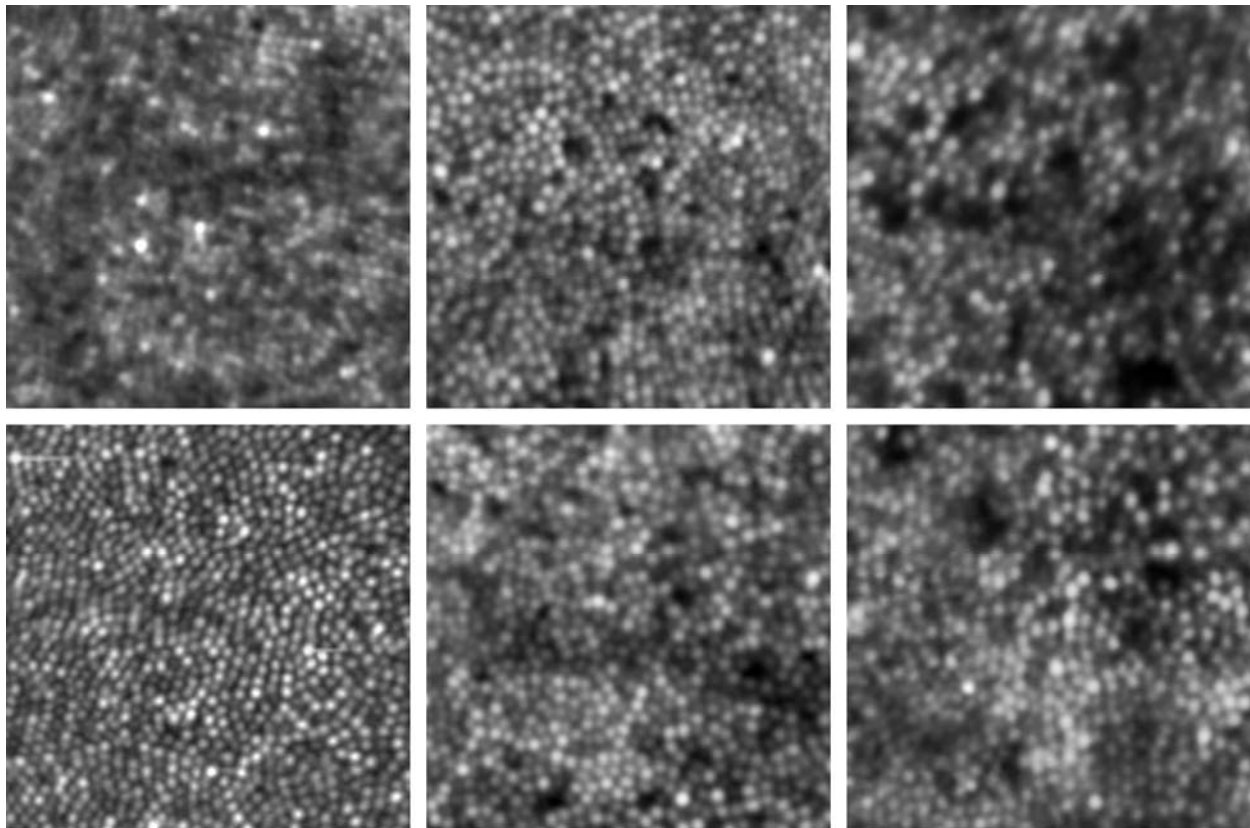


**Figure 36| Appearance of carrier cone mosaic.** Image dimensions are  $0.5^\circ \times 0.5^\circ$ , centered  $1^\circ$  from the PRLF. Left column (top) is the control eye and left column (bottom) is a normal retina with large spacing from a previous study. Center column (top) is BCMc1 (OS) and right column (top) is BCMc1 (OD). Center column (bottom) is BCMc2; right column (bottom) is BCMc3.

## 5.4 Results

### 5.4.1 Gross Appearance of Cone Mosaic

The gross appearance of the photoreceptor mosaic in the BCM carrier eyes was similar to normal eyes. However, cones appeared larger in the carrier eyes at equivalent eccentricities relative to normal eyes. Areas of the cone photoreceptor mosaic at one degree from the PRLF for the four carrier retinas and the control retina are shown in Figure 36. Since there is large variability in normal eyes, a region from a normal retina imaged in a previous study that had exceptionally large cone spacing is also shown for comparison (observer S3 from Chapter 4). It can be seen that the cones appear much larger in the carrier images than in either normal image. There were not large gaps in the carrier mosaic. There were hypo-reflective areas, sometimes the size of single or multiple cones, but this was also seen in the control eye, and is typically seen in normal eyes. These areas often contain cones. This can usually be confirmed by comparing AOSLO imagery obtained on different days. It has been shown that the reflectance of individual cones in adaptive optics imagery is a dynamic process that changes over varying time intervals ranging from minutes to hours; it has been suggested that this process is related to disc shedding in photoreceptor outer segments (Pallikaris et al., 2003).

### 5.4.2 Comparing AOSLO Images to AO Images Previously Obtained with a Flood Illuminated AO Fundus Camera

Since images were previously obtained for one of the subjects in this study with the Rochester 2<sup>nd</sup> generation AO ophthalmoscope (Hofer et al., 2001), the imagery obtained from these two different AO instruments were compared. Two 0.5° x 0.5° patches of retina, centered at 0.5° and 1° from the PRLF from observer BCMc2, obtained with the different ophthalmoscopes, are compared in Figure 37. The AOSLO image is shown in the left panel, while the flood illuminated AO ophthalmoscope image is shown in the middle panel. Cone locations were obtained by manually marking cone centers in each image and are compared in the third column (AOSLO centers are marked with an X; Rochester AO ophthalmoscope images are marked with an O). Four colored circles mark equivalent areas in the retinal imagery. The yellow circle shows a cone that is visible in both systems. The red circle marks a location where a cone is absent in each system. The green circle marks a location where a cone is visible in the Rochester AO ophthalmoscope but is not visible in the AOSLO. The blue circle marks a cone visible in the AOSLO image but not visible in the Rochester AO ophthalmoscope image. It should be noted that due to the scanning nature of the AOSLO system, there are small distortions in the AOSLO imagery due to errors in stabilization. This is illustrated in Column 3 of Figure

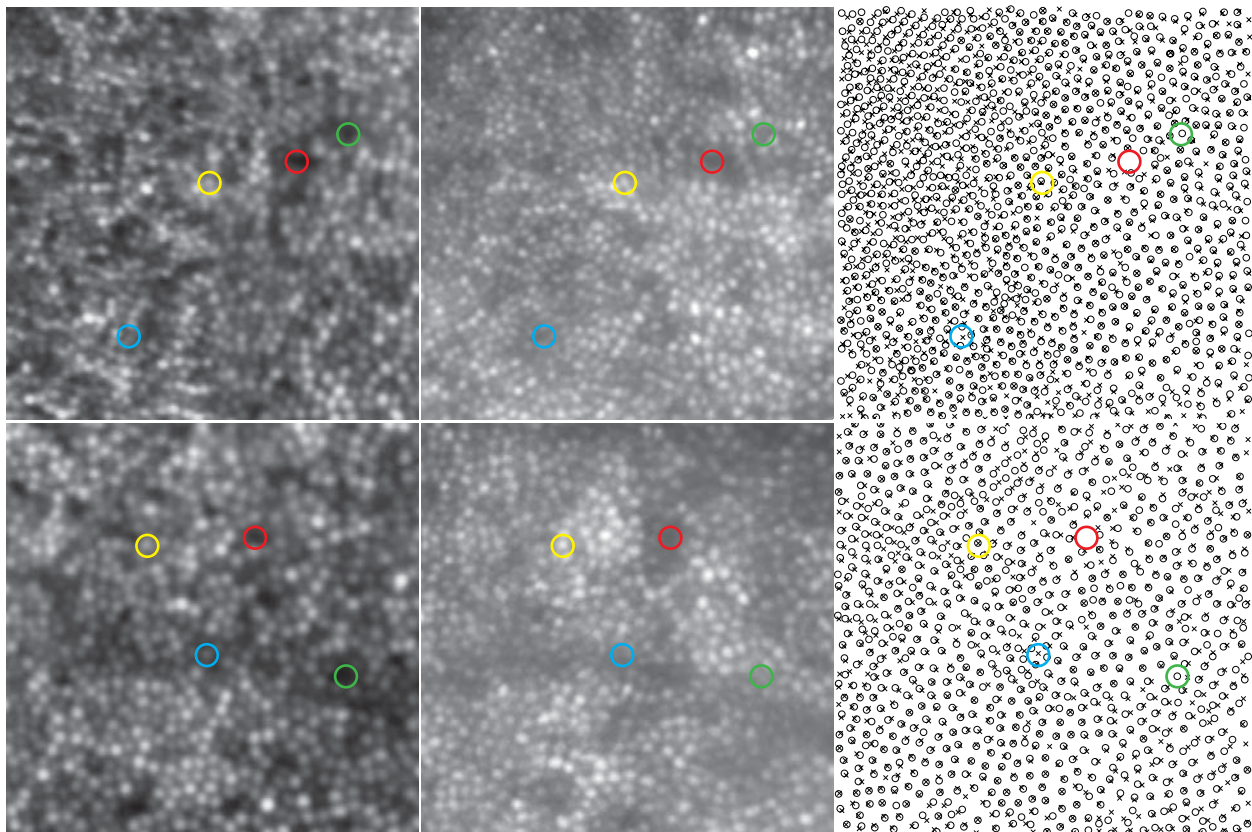


**Figure 37| Comparison of retinal images from different AO imaging systems.** Images obtained of BCMc2 on different imaging systems; dimensions are 0.5° x 0.5°. Top row is 0.5° from the PRLF; bottom row is 1° from the PRLF. Left column are AOSLO images; middle column are Rochester AO ophthalmoscope images; right column compares cone locations obtained from the two different images (AOSLO cone positions are marked with an X, Rochester AO ophthalmoscope image cone positions are marked with circles). Colored circles mark cones found in both systems (yellow), cones appearing only in the Rochester image (green), cones appearing only in the AOSLO image (blue), and locations where cones are absent in both images (red).

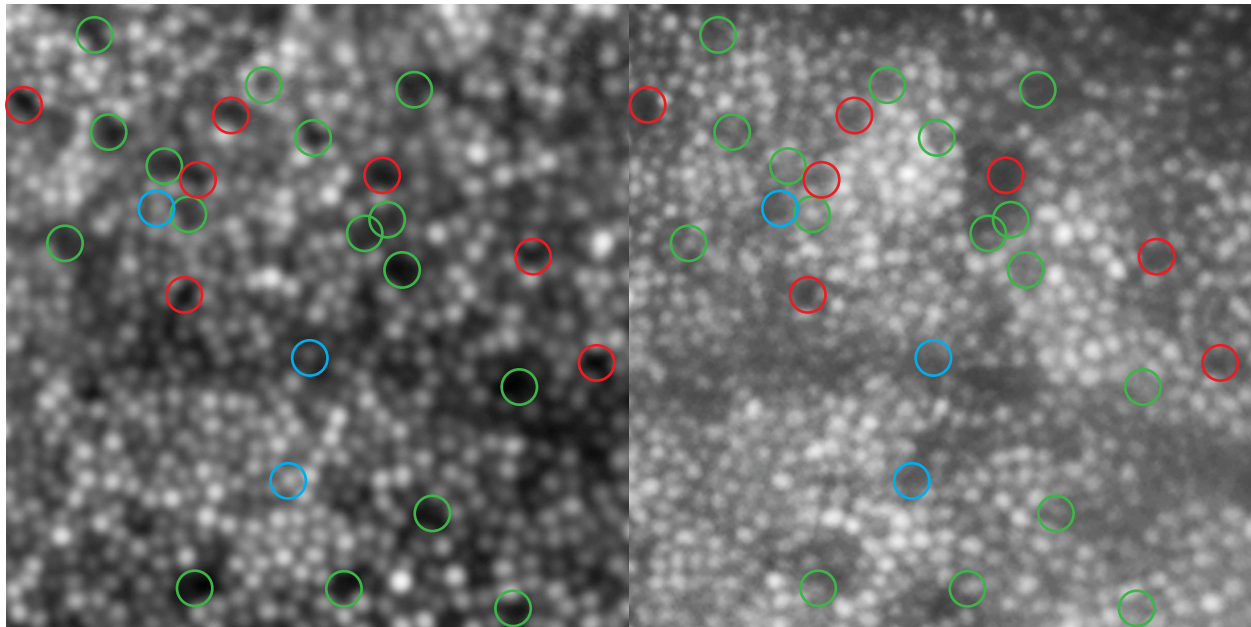


**Figure 38| Full comparison of 1° location from different AO imaging systems.** Comparison of images obtained from BCMc2, from figure 37. Dimensions are  $0.5^\circ \times 0.5^\circ$ . Colored circles mark cones appearing only in the Rochester image (green), cones appearing only in the AOSLO image (blue), or locations where cones are absent in both images (red). 23 more cones were found in the Rochester AO ophthalmoscope image than in the AOSLO image. 16 cones (green) were hypo-reflective in the AOSLO image, while 3 cones (blue) were hypo-reflective in the Rochester image, a net difference of 13 cones. The remaining 10 cone difference is due to edge effects resulting from distortions in the AOSLO imagery that make the two images not entirely coincident.

37, which compares cone locations found in the two different systems for the same patches of retina.

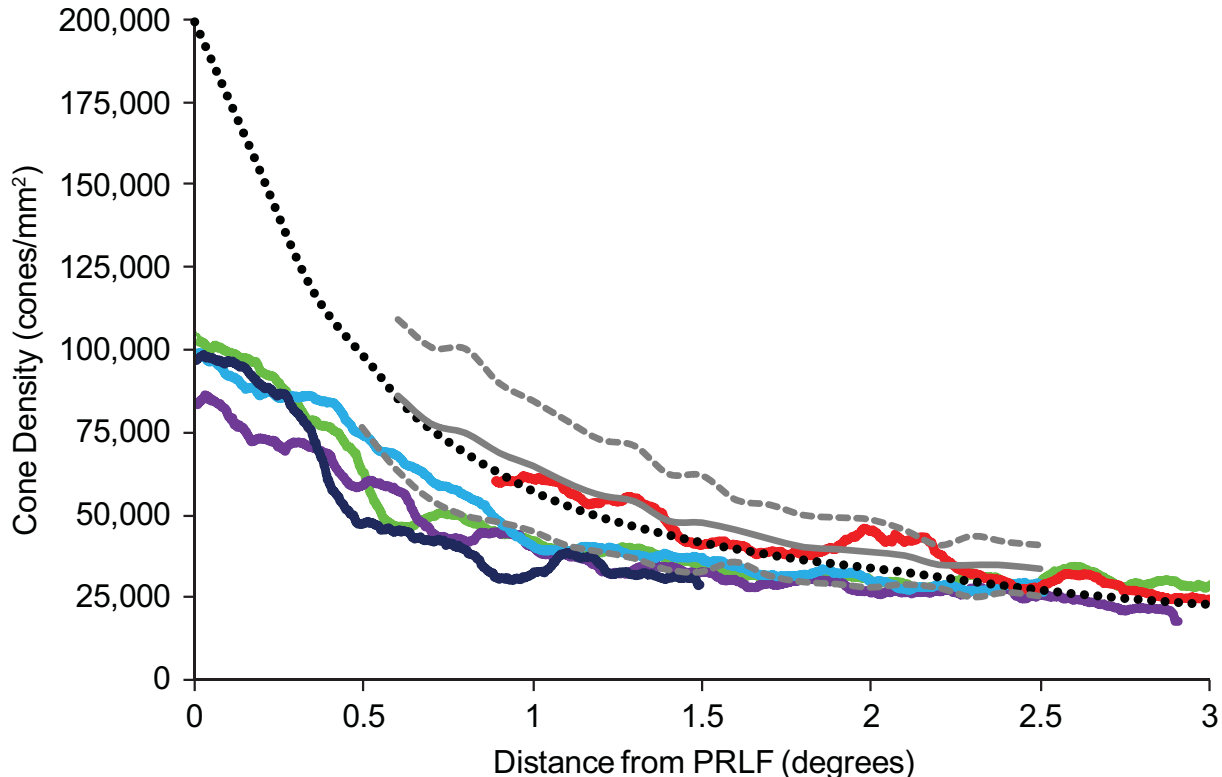
Careful comparison reveals that the hyporeflective areas in the AOSLO imagery often contain cones in the Rochester AO ophthalmoscope images. 1,065 cones were located in the  $0.5^\circ$  patch for the AOSLO image, while 1,108 cones were identified in the Rochester AO ophthalmoscope image, a difference of 43 cones. 787 cones were found in the AOSLO image for the  $1^\circ$  patch, while 810 cones were found in the Rochester AO ophthalmoscope image, a difference of 23 cones. These differences are small, around 4% fewer cones in the AOSLO image relative to the Rochester AO ophthalmoscope image at the  $0.5^\circ$  location, and 2.9% at the  $1^\circ$  location.

Figure 38 compares the  $1^\circ$  location in detail, marking all cones that did not appear in the imagery obtained from both systems, using the same color coding as Figure 37. Cones that were not localized on the retinal imagery will cause errors in spacing and regularity measurements. These errors are small but will have the following effects: increased cone spacing, reduced cone density, and decreased mosaic regularity. Mean  $N_c$  estimates from measured ICD are 1.016 arcmin for the AOSLO image and 0.997 arcmin for the flood-AO image; a spacing increase of less than 2% in the AOSLO image, which is about a fourth of the size of a single pixel. It should be noted that some methods of measuring cone spacing, such as the density recovery profile method, which is based on distance histograms, would not reveal this difference. This difference arises from both the spatial distortions in the AOSLO imagery and the different number of cones identified in each image. Spatial distortions give rise to edge effects around the bounding box of

each image, making some cones not visible in both windows. A direct (counting) measure of density results in measurements of 43,417 and 44,686 cones/mm<sup>2</sup> for AOSLO and Rochester AO ophthalmoscope images, respectively, a difference of less than 3%. Figure 38 shows 16 cones in the flood image that were hypo-reflective in the AOSLO image and 3 cones in the AOSLO image that were hypo-reflective in the flood illuminated image, a net difference of 13 cones. This shows that about half of the difference in the density and spacing measurements noted above is probably due to the images not be entirely coincident (due to spatial distortions only). The measurement errors that arise due to hypo-reflective cones are therefore probably smaller than those that arise when different humans manually localize cones in AOSLO images (Li et al., 2007).

### 5.4.3 Cone Density

Cones were resolved at or near the foveal center for all carrier eyes although the quality of the retinal imagery varied considerably between subjects. Cone densities across the horizontal temporal retina are shown in Figure 39. Density shown was calculated using the Voronoi patch method. For comparison, the mean density from Curcio (Curcio et al., 1990b) is plotted as the black dotted line, and the mean and  $\pm 2$  SD from the normal observers in Chapter 4 are shown as the solid and dashed gray lines, respectively. There was some difficulty in identifying every cone at the PRLF in all of the images, with cones being most difficult to resolve in carrier BCMc2, who had the highest cone density. Her estimated peak cone density was 105,930 cones/mm<sup>2</sup>. Deconvolution helped to resolve cone centers near the PRLF in BCMc2. Some



**Figure 39| Cone density along the horizontal meridian.** BCMc1(OS), BCMc1(OD), BCMc2, BCMc3, and control eye are shown respectively in light blue, dark blue, green, purple, and red. Solid and dashed grey lines show the mean  $\pm 2$  SD for the 5 observers from Chapter 4. The dotted black line shows the average density of the nasal and temporal meridians from the data of Curcio et al. (Curcio et al., 1990b).

cone locations were estimated, so her peak density may be a slight underestimate. For the carrier with the lowest density, BCMc3, all of the cones in the central fovea were resolved without requiring the aid of any deconvolution; her peak density was 86,635 cones/mm<sup>2</sup>. BCMc1 had both of her eyes imaged and showed intermediate peak densities. Peak densities were 99,448 and 99,571 cones/mm<sup>2</sup> in her right and left eyes, respectively; deconvolution helped to identify cone centers at the PRLF for this observer. It is interesting to note that although peak densities were nearly identical in both eyes, the falloff in density was much more rapid in the right eye; density fell to half of its peak value ~0.47° from the PRLF in the right eye and ~0.88° in the left eye. Mean peak cone density for the four carrier eyes examined was 97,818 cones/mm<sup>2</sup> (SD = 8,239). The average for the three carriers (with both eyes averaged for carrier BCMc1) is 97,254 cones/mm<sup>2</sup> (SD = 9,995). Cones were not resolved at the center of the fovea using AOSLO for the control observer, density was measured in a previous imaging study using a flood illumination AO system for this observer and was reported as 226,929 cones/ mm<sup>2</sup> (Putnam et al., 2005).

#### 5.4.4 Mosaic Regularity

Mosaic regularity was assessed by using the Delaunay triangulation in MATLAB to find cone neighbors and to evaluate the number of neighbors of each cone. In a perfectly regular triangular lattice arrangement each cone has 6 neighbors. However, a perfect triangular lattice arrangement is not found in the human retina, especially in the fovea, because the spacing between receptors increases rapidly with increasing distance from the center of the fovea. The percentage of cones having six neighbors, averaged at 0.1 degree intervals for all carrier eyes is plotted in Figure 40. Values are plotted relative to the PRLF. For comparison, the average of 6 normal eyes (the control eye and 5 normal eyes from Chapter 4 (Rossi et al., 2009) ) are shown as blue circles; measurements for normal eyes within 0.3 degrees from the PRLF are excluded due to the lack of sufficient data from normal subjects in that area. For the normal eyes, data from 5 eyes is averaged at the 0.4° location while 6 eyes are averaged elsewhere. For the carrier eyes, four eyes are averaged between 0° and 1.4° and three eyes elsewhere. Due to individual variations in regularity, some of the individual differences are obscured in the averaged data. The maximum percentage of cones with 6 neighbors for normal eyes ranged from 54.6% to 75.5% at locations between 0.56 and 1.75 degrees from the foveal center. The average maximum percentage of cones with 6 neighbors was 66.1% for the normal eyes (SD = 7.7). The maximum percentage of cones having 6 neighbors was 56.9%, 55.6%, 57.3% and 58% at

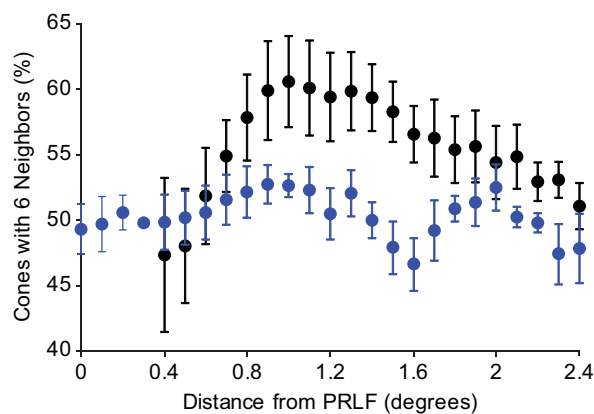


**Figure 40| Percentage of cones having 6 neighbors.** Mean percentage of cones averaged at 0.1 degree intervals for the BCM carriers (blue circles) and 6 normal observers (black circles; control eye and 5 from Chapter 4). Error bars are  $\pm$  SEM.

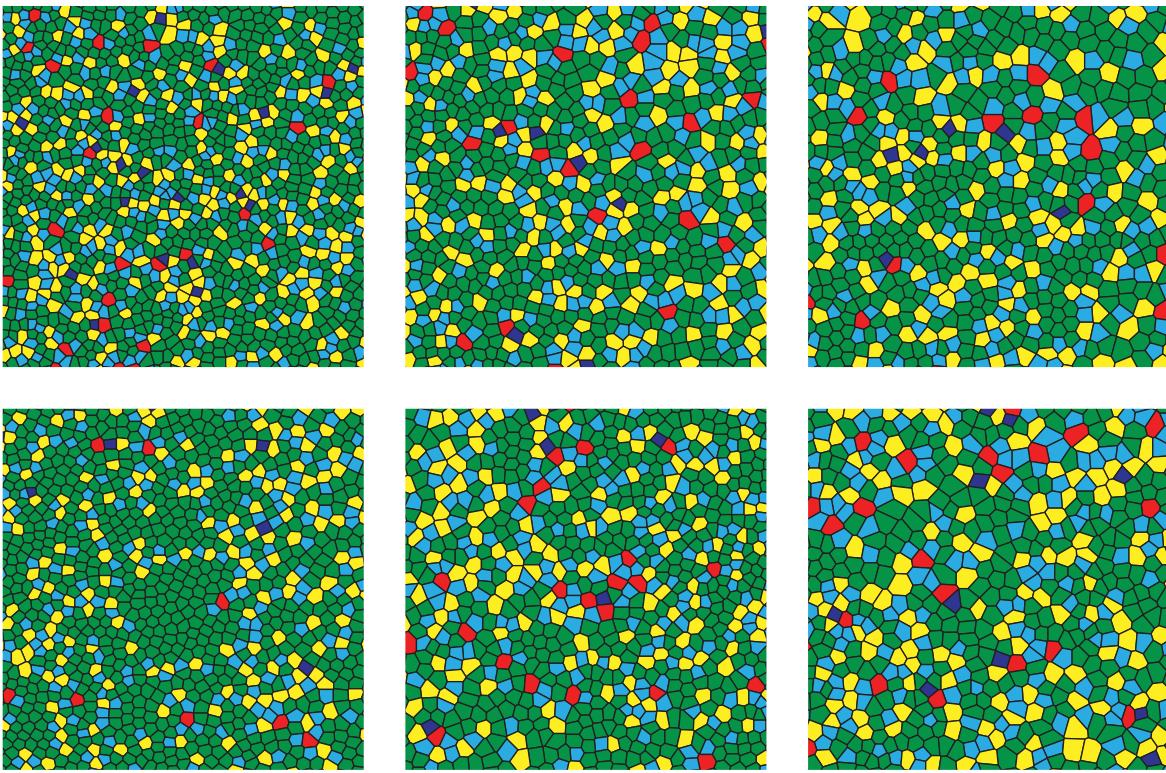


**Figure 41| Voronoi diagrams.** Voronoi diagrams of cone mosaic from images shown in figure 36. Images dimensions are  $0.5^\circ \times 0.5^\circ$ , centered  $1^\circ$  from the PRLF. Left column (top) is the control eye and left column (bottom) is a normal retina with large spacing (S3 from Chapter 4). Center column (top) is BCMc1 (OS) and right column (top) is BCMc2 (OD). Center column (bottom) is BCMc2; right column (bottom) is BCMc3. Voronoi patch color corresponds to the number of neighbors of each cone, where blue, cyan, green, yellow, and red polygons correspond to cones having, respectively,  $\leq 4$ ,  $5$ ,  $6$ ,  $7$ , or  $\geq 8$  neighbors.

eccentricities of  $0.95^\circ$ ,  $0.59^\circ$ ,  $1.1^\circ$ , and  $2.69^\circ$  for BCMc1(OS), BCMc1(OD), BCMc2 and BCMc3, respectively. The average maximum percentage of cones having 6 neighbors was 57% for all carrier eyes ( $SD = 1$ ). The Voronoi diagrams are also a useful tool for visually inspecting the regularity of the mosaic. Voronoi diagrams were created in MATLAB and are shown in Figure 41 for the 4 carrier eyes, the control eye and from a patch of mosaic from the eye from Chapter 4 which had the largest cone spacing; patches correspond to the  $0.5^\circ \times 0.5^\circ$  areas centered  $1^\circ$  from the PRLF shown in Figure 36.

#### 5.4.5 Fixation Stability

Fixation stability was assessed by precisely localizing the position of the stimulus on the retina for each frame of each psychophysical trial. The standard deviation of the position of the stimulus on the retina at each psychophysics test location is a precise measurement of the fixational spread of the eye. The standard deviation of the stimulus position (averaged for both x and y directions) is plotted versus eccentricity in Figure 42. For comparison, a linear regression fit with upper and lower 95% confidence interval lines is plotted for a group of normal observers (5 eyes from Chapter 4 (Rossi et al., 2009) and the control eye from this study). Two of the BCM carriers (BCMc1 and BCMc3) had fixational eye movements that were outside the

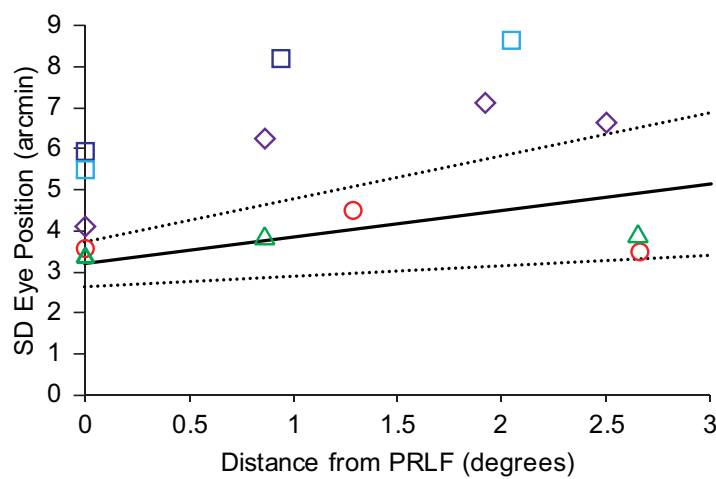


**Figure 42| Fixation stability at resolution test locations.** SD of stimulus position averaged for vertical and horizontal directions as a function of eccentricity. Solid and dashed lines are linear regression line and upper and lower 95% confidence intervals fit to data from 6 normal eyes (control eye and 5 normal eyes from Chapter 4). BCMc1 (OS), BCMc1 (OD), BCMc2, BCMc3, and control eye are shown respectively as light blue squares, dark blue squares, green triangles, purple diamonds, and red circles. BCMc1 & BCMc3 fell outside the normal range at all locations, while BCMc2 and the control eye fell within the normal range at all test locations.

normal range at all locations, while one (BCMc2) was within the normal limits at all test locations. Figure 43 compares the SD of eye position when observers either looked at the fixation target or at the stimulus. Fixation was more stable for both groups when looking at the stimulus than when looking at the fixation target, with the carriers being less stable than normal observers in both conditions.

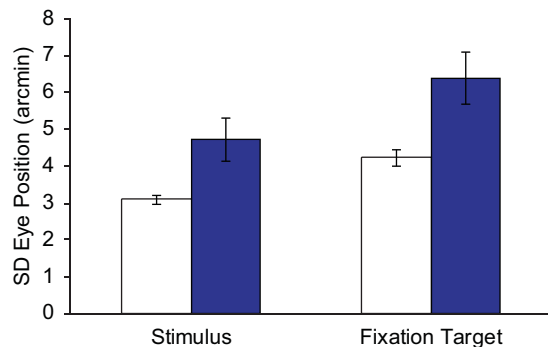


**Figure 43| Fixational stability when observers looked at the stimulus or fixation target.** Fixation was more stable for both groups when looking at the stimulus. Normal observers (white bars) are more stable than carriers (blue bars) in either condition. Mean of 6 normal eyes is shown (the control eye, and the 5 normal eyes from Chapter 4). Mean of 4 carrier eyes is shown. Error bars are  $\pm$  SEM.

#### 5.4.6 Cone Spacing and the Nyquist Limit of the Cone Mosaic

Minimum intercone-distance (ICD), the average center-to-center distance between a cone and each of its nearest neighbors, was higher in the carrier eyes compared to normal eyes. The average minimum ICD measured from the four carrier eyes was 0.794 arcmin ( $SD = 0.034$ ). BCMc3 had the largest minimum ICD of 0.842 arcmin. BCMc1 had minimum ICD of 0.786 arcmin in each eye. BCMc2 had the lowest ICD, at 0.763 arcmin. Minimum ICD was found within 3 arcmin of the PRLF for all carrier eyes. An assessment of mosaic regularity confirmed a fairly triangular packing arrangement in the carrier retina, indicating that this was probably an appropriate method for calculating  $N_c$ .  $N_c$  across the horizontal temporal retina is shown in Figure 44a. For comparison, the mean  $N_c$  and mean  $\pm 2$  SD of six normal observers (the control eye and 5 from a previous study) and mean  $N_c$  calculated from the density measurements of

Curcio (Curcio et al., 1990b) are also shown. Densities from Curcio were converted to  $N_c$  using the following equation:

$$N_c = \left( \frac{60}{m} \right) \times \sqrt{\frac{\sqrt{3}}{2d}} \quad (5)$$

Where  $m$  is the number of mm per degree and  $d$  is cone density. A value of  $m$  of 0.289 was used, assuming all eyes were emmetropic with a 24 mm axial length.

Minimum  $N_c$  was 0.680, 0.681, 0.661 and 0.730 arcmin for BCMc1 (OD), BCMc1 (OS), BCMc2 and BCMc3, respectively. Mean minimum  $N_c$  was 0.688 arcmin ( $SD = 0.029$ ) for the four carrier eyes.  $N_c$  was estimated for the control eye based upon a cone density measurement obtained previously (Putnam et al., 2005). Since it was previously shown that the PRLF of this observer was displaced from the position of peak cone density to an area where density had fallen to ~10% below its peak, peak density was first reduced by 10% to estimate the density at the PRLF and then converted to  $N_c$  using the same equation used for the Curcio data, but with the appropriate  $m$  value for this subject (Table 4). This resulted in an estimate of  $N_c$  of 0.39' at the PRLF for the control eye.

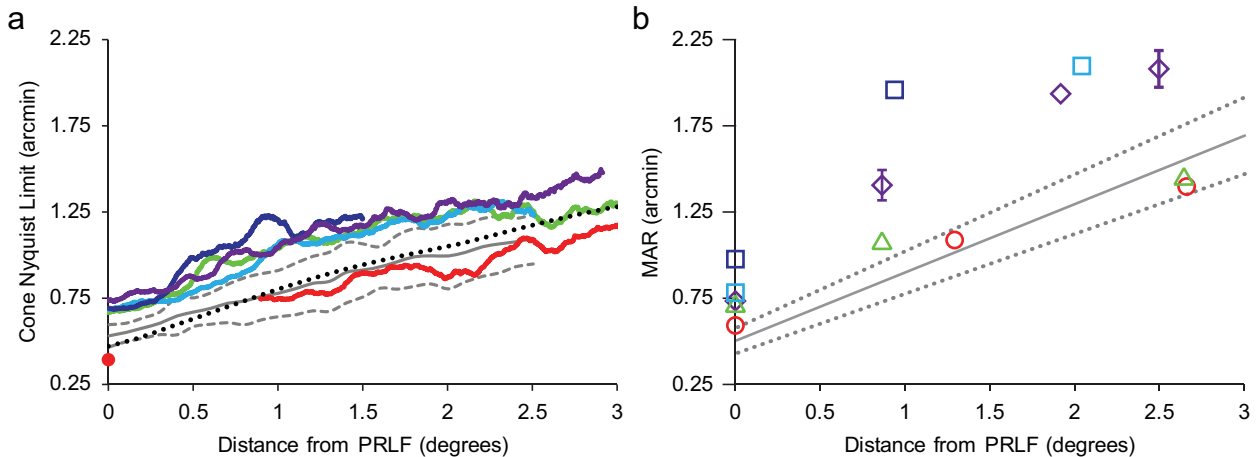


**Figure 44| a) Nyquist limit of the cone mosaic ( $N_c$ ).** BCMc1(OS), BCMc1(OD), BCMc2, BCMc3, and control eye are shown respectively as light blue, dark blue, green, purple, and red lines. Red circle denotes estimate of  $N_c$  from density of control eye measured in a previous study (Putnam et al., 2005). Dotted black line shows mean  $N_c$  derived from average densities of Curcio (Curcio et al., 1990b). Solid and dashed grey lines show the mean  $\pm 2 SD$  for 6 normal eyes (the control eye and the 5 normal eyes from Chapter 4). **b) Visual resolution (MAR) as a function of eccentricity.** BCMc1 (OS), BCMc1 (OD), BCMc2, BCMc3, and control eye are shown respectively as light blue squares, dark blue squares, green triangles, purple diamonds, and red circles. Solid and dashed lines are regression line and 95% confidence intervals fit to the data of 5 normal observers from Chapter 4.

#### 5.4.7 Visual Resolution and $N_c$

MAR is plotted versus eccentricity in Figure 44b. Cone mosaics overlaid with topographic maps of stimulated cones are shown in Figure 45. As can be seen from Figure 45, the stimuli did not always fall precisely along the horizontal meridian, so MAR is plotted versus linear distance from the PRLF in Figure 44b. For comparison, a linear regression fit to the data of 5 normal observers from Chapter 4 is plotted with 95% confidence intervals as the dashed and solid lines, respectively. The control observer fell within the normal range at all test locations; it should be noted that he was near the high end of the normal range at the PRLF. This is not

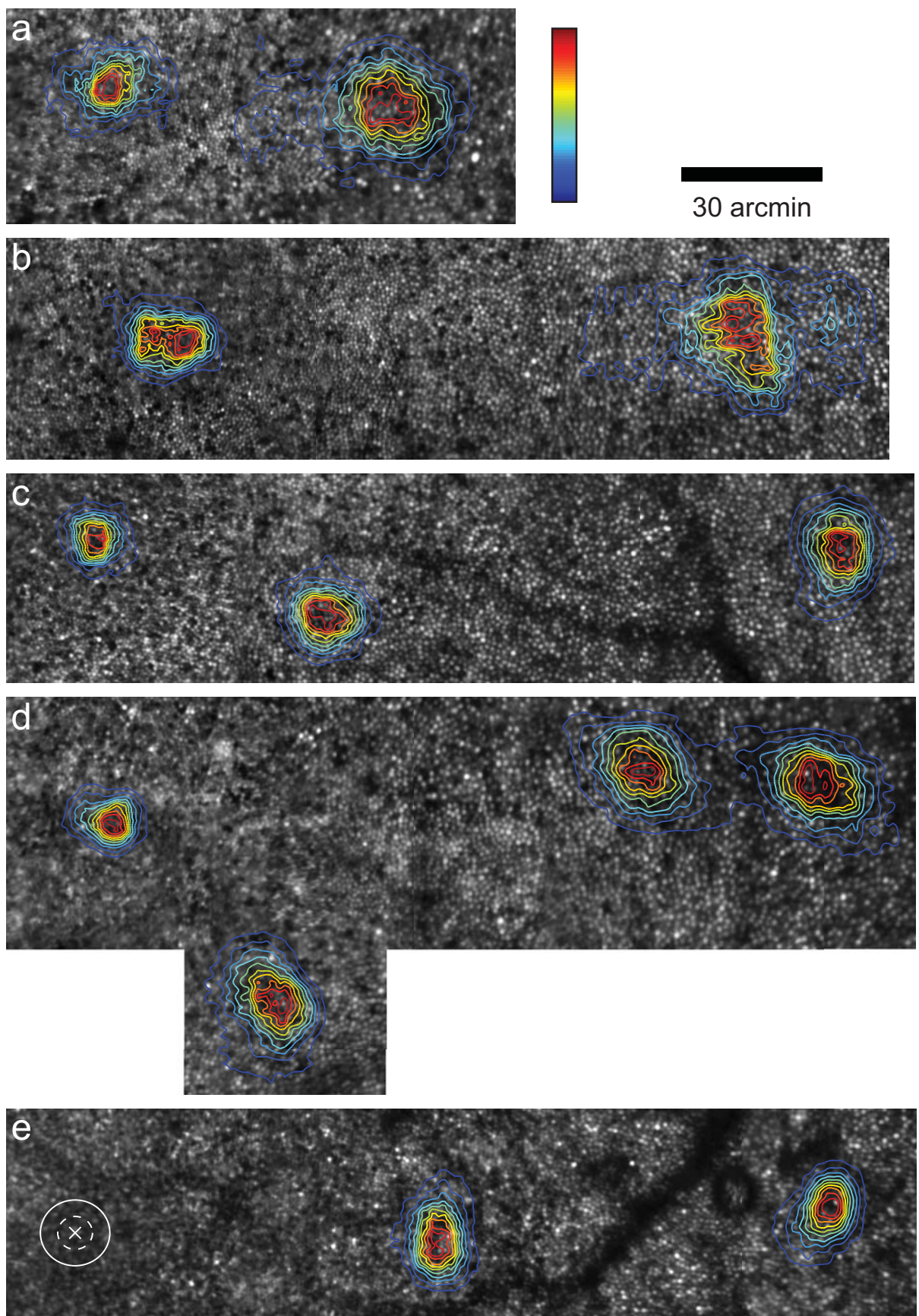


**Figure 45| Retinal imagery overlaid with contour lines showing stimulated cones.** (previous page) Topographical maps overlaid in color show the normalized level of cone stimulation at each test location. a) BCMc1 (OS); b) BCMc1 (OD); c) BCMc2; d) BCMc3; e) control. Cones appear as bright circles. Each cone stimulated over the course of the psychophysical tests was localized on the mosaic using methods described in Chapter 4. Color bar shows normalized level of cone stimulation; PRLF is the location at the far left of all images. Since cones were not visualized at the PRLF for the control eye, an X marks the PRLF, with the solid and dashed white ellipses drawn to show  $\pm 1$  and  $\pm 2$  SD of stimulated area, respectively.

surprising as this observer was myopic and as was shown in Chapters 2 and 3, myopes tend to perform worse than emmetropes in AO corrected tests of visual resolution (Rossi et al., 2007). Resolution was outside the normal range at the PRLF and at the  $0.86^\circ$  location for BCMc2, however her performance fell back to within the normal range by the  $2.64^\circ$  test location. It should be noted that she also was outside the normal range for  $N_c$  until  $\sim 2.5^\circ$  from the PRLF. The other carrier eyes had worse resolution than expected for normal eyes at all test locations. BCMc1, who had both eyes tested, and had similar spacing at the PRLF in each eye had worse resolution in her right eye at the PRLF; it is interesting to note that her right eye was the one that showed the more rapid decrease in density away from the PRLF. Her performance at the  $0.94^\circ$  test location in her right eye ( $MAR = 1.96'$ ) was similar to that at the  $2^\circ$  test location in her left

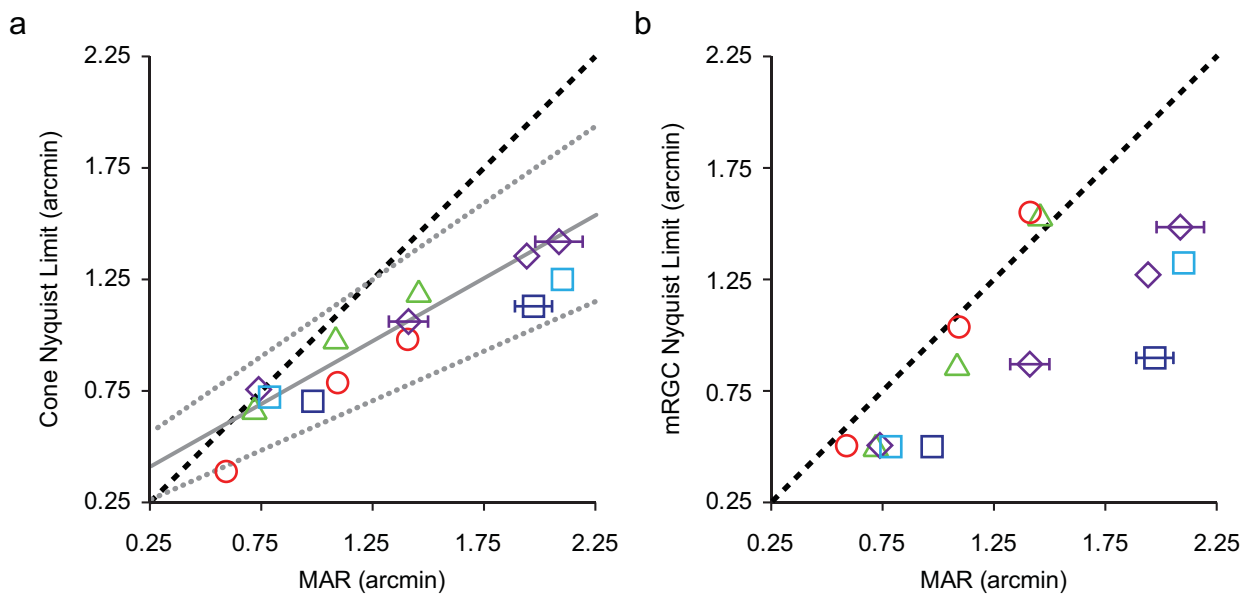
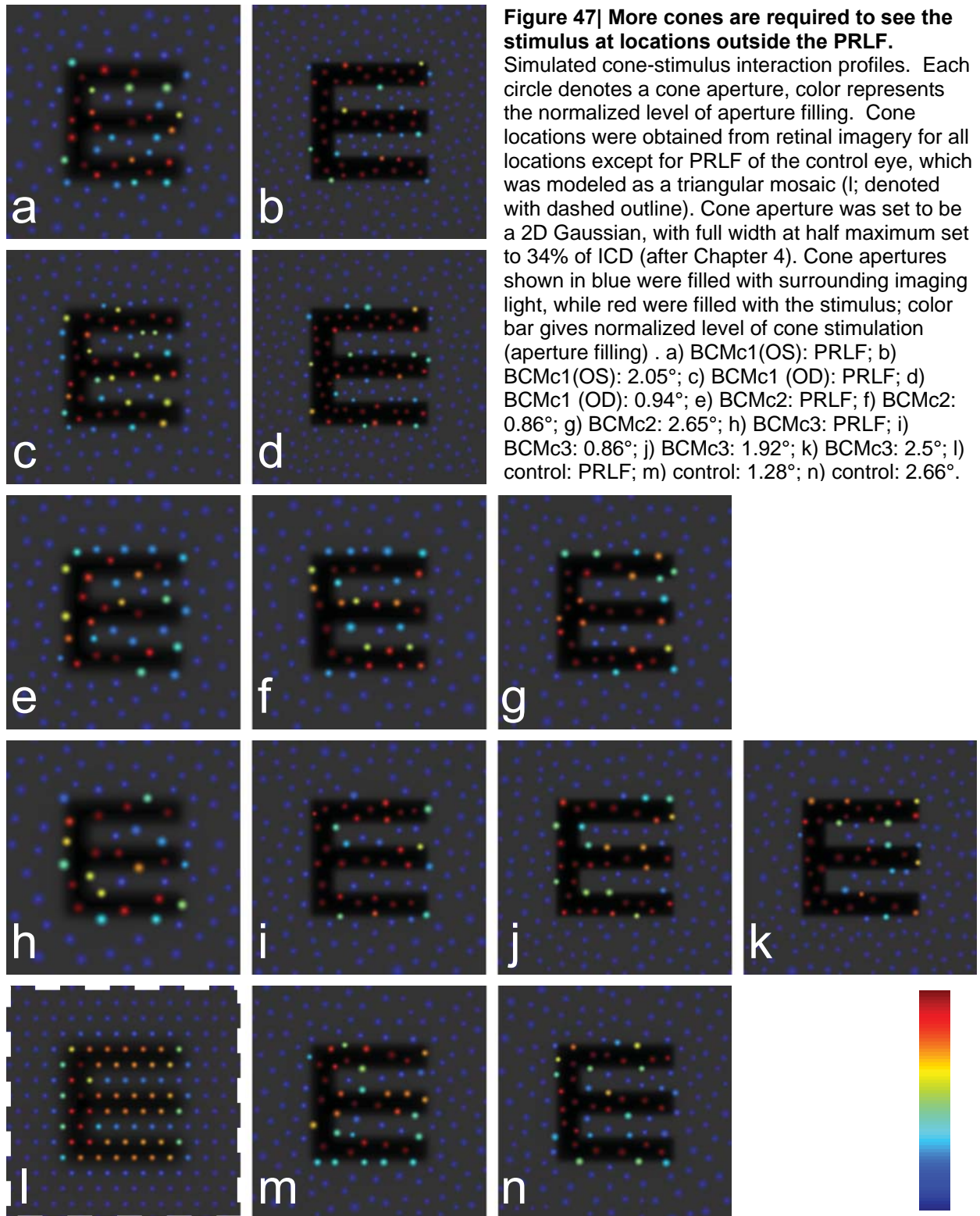


**Figure 46| a) MAR is worse than predicted by the Nyquist limit of the cone mosaic outside the PRLF.** BCMc1 (OS), BCMc1 (OD), BCMc2, BCMc3, and control eye are shown respectively as light blue squares, dark blue squares, green triangles, purple diamonds, and red circles. Dashed black line is the 1:1 line of equality. Solid and dotted gray lines are linear regression line with 95% upper and lower confidence intervals from the data of 5 normal observers from Chapter 4. Error bars are  $\pm$  SEM and omitted when smaller than the symbol. **b) Nyquist limit of the normal eye's mRGC mosaic does not predict resolution outside the PRLF for BCM carriers.** BCMc1 (OS), BCMc1 (OD), BCMc2, BCMc3, and control are shown respectively as light blue squares, dark blue squares, green triangles, purple diamonds, and red circles. Dashed black line is the 1:1 line of equality. MAR of control eye and BCMc2 at the most eccentric test location fit well with the Drasdo model (Drasdo et al., 2007) estimates of  $N_{mRGC}$  outside the PRLF; resolution at the other test locations for BCMc2 and for the other 3 carrier eyes at all locations is worse than predicted by  $N_{mRGC}$ .



eye ( $MAR = 2.1'$ ), where  $N_c$  was similar in both eyes ( $N_c$  was  $1.13'$  and  $1.25'$  in her right and left eyes, respectively).

$MAR$  is plotted against  $N_c$  at resolution test locations in Figure 46a. For comparison, a linear regression line with 95% confidence intervals fit from the data the normal observers from

Chapter 4 is shown as the solid and dotted grey lines, respectively. MAR agreed well with estimates of  $N_c$  at the PRLF for three of the four carrier eyes. There was a moderate difference between MAR and  $N_c$  at the PRLF for observer BCMc1 in her right eye. The control eye had a moderate difference between MAR and  $N_c$  at the PRLF as well, indicating that the resolution deficit seen in myopia can, at least in part, be attributed to postreceptoral factors (see Chapter 3) (Rossi et al., 2007).

Most normal observers are well matched to estimates of  $N_c$  at the PRLF, as was shown in Chapter 4. Outside the PRLF, MAR decreased at a greater rate with increasing eccentricity than predicted by  $N_c$ . This finding is in agreement with results obtained and reported in Chapter 4 for normal observers (Rossi et al., 2009). Figure 47 shows simulated patterns of cone stimulation for a threshold sized stimulus located at the center of each test location for each observer. Cone apertures were estimated from ICD and are colored relative to the normalized level of cone stimulation. The diffraction limited PSF was used to blur the stimulus and the blurred stimulus is overlaid as semi-transparent shading. Since cones were not resolved at the PRLF for the control eye, a simulated hexagonal mosaic with the estimated spacing for the control eye was used. As can be seen clearly from this simulation, more cones were stimulated by the threshold sized stimulus as distance from the PRLF increased, just as was shown for normal observers in Chapter 4.

#### **5.4.8 Visual Resolution compared to $N_{mRGC}$ for Normal Eyes Suggests Significant Post-Receptoral Differences in the Carrier Retina**

MAR is plotted against the estimated normal Nyquist limit of the mRGC mosaic (derived from the model of Drasdo and colleagues (Drasdo et al., 2007)) in Figure 46b. The data points from normal observers tend to cluster around the dashed 1:1 line of equality (Rossi et al., 2009); this expected relationship was found for the control eye. Linear regression lines fit to the data from normal observers have an average slope close to one, indicating that MAR matches the Nyquist limit of the mRGC mosaic (see Chapter 4). A linear regression line fit to the data from the control observer had a slope of 1.26, slightly higher than the average of five other normal eyes (1.01); the increased slope relative to normal observers can again most likely be attributed to the myopic shift towards reduced resolution at the PRLF, and, additionally by the small number of data points obtained.

The findings for the BCM carriers are quite different from what has been shown previously for normal observers. For BCMc2, the data points fall below the equality line at the PRLF and  $0.86^\circ$  test locations, with the data point for the most eccentric test location ( $2.65^\circ$ ) falling near the equality line, where she also appeared normal on all other measures. Data points for the other 3 carrier eyes fall below the line of equality at all locations, showing that MAR is worse than predicted by the Drasdo et al. model of mRGC density from normal eyes (Drasdo et al., 2007). This indicates significant post-receptoral differences in BCM carriers.

### **5.5 Discussion**

#### **5.5.1 Cone Loss in the BCM Carrier Occurs Early in Development**

The average peak cone density for the four carrier eyes examined was about half of the average peak cone density of  $199,000$  cones/ $\text{mm}^2$  in normal eyes (Curcio et al., 1990b). The two lowest peak cone densities in that report were  $98,200$  and  $120,000$  cones/ $\text{mm}^2$ , which the authors stated were likely to be underestimates (Curcio et al., 1990b). Even if they are valid, then this analysis showed that the average peak density of the four carrier eyes is less than the lowest

density measured in normal eyes. The reduction in cone density was logically coupled to an increase in cone spacing. Mean  $N_c$  was 68% higher in the carrier retina than in the normal retina (Curcio et al., 1990b). This difference (0.218 arcmin) is greater than 2 SD away from the mean from normal eyes (Curcio et al., 1990b).

However, the reduced cone density and increased cone spacing seen in the carrier retina did not appear to be linked to a significant increase in cone packing disorder. The major difference seen in the packing arrangement of cones between the normal and carrier eyes was the lack of a peak in regularity  $\sim 1^\circ$  from the PRLF. In the averaged data from the normal eyes, the percentage of cones having six neighbors rose above 60% between  $0.9^\circ$  and  $1.3^\circ$  degrees. The percentage of cones having six neighbors never rose above 60% in any of the carrier eyes. Curcio and Sloan examined the packing arrangement of cones in a single histological specimen and found the most regular packing arrangement at  $\sim 0.2\text{-}0.35$  mm ( $\sim 0.7^\circ\text{-}1.2^\circ$ ) from the location of peak density (Curcio et al., 1992). It is probable that the absence of a highly regular area around  $1^\circ$  in the carrier eyes is due to reduced cone density. It has been suggested that one factor influencing mosaic regularity around the foveal center is the degree to which cones are closely apposed and thereby become subject to the physical constraints of close packing (Curcio et al., 1992). Evidence supporting this is found in the extreme similarity of pointing direction of individual cones (Roorda et al., 2002a). Increased cone spacing near the fovea in the carrier retina reduces this constraint.

Since large gaps in the mosaic corresponding to the locations of lost cones were not observed in the BCM carrier, but rather a fairly regular mosaic of larger than normal cones with decreased density and increased spacing relative to normal retina was observed, one hypothesis concerning the development of the carrier retina, namely that the cones expressing the non-functional photopigment survive to maturity, can be eliminated. The hypothesis that is consistent with the anatomical findings is that cones that inactivate the healthy cone opsin gene degenerate early in development, prior to receptor migration.

### **5.5.2 Fixational Eye Movements are Abnormal in BCM**

The average SD of fixation for the normal observers when looking at the stimulus was similar to that observed by other researchers (Putnam et al., 2005; Putnam et al., 2005; Steinman, 1965). The larger SD of fixation when both groups of observers looked at the fixation target relative to the stimulus was not surprising as target size, luminance and color (all of which were different for the fixation target relative to the stimulus) have been shown to affect fixational stability (Steinman, 1965). The relatively larger spread of fixation found in the carriers is consistent with the abnormalities in eye movements previously observed in BCM carriers (Gottlob, 1994). It should be noted that BCMc2 had a pattern of fixation that was within the normal range at all locations; she is the carrier who also had the best resolution, highest cone density, and presumably the least amount of cone loss. She was also the youngest of the three carriers examined. It is interesting to note that for test locations at the PRLF, MAR was moderately correlated with the SD of fixation for the carriers ( $R^2 = 0.70$ ) but not as well for the normal observers ( $R^2 = 0.31$ ).

However, the larger motion probably did not cause the resolution in the carriers to be reduced, as it has been shown that visual resolution is largely unaffected by retinal image motion (Westheimer & McKee, 1975). In fact, the relative fixational instability seen in two of the three carriers is probably a result of their increased  $N_c$  and lower MAR, consistent with the hypothesis of Steinman and colleagues, that one fixates accurately in order to see clearly, not because one

sees clearly (Steinman, Pizlo, Forofonova, & Epelboim, 2003). The fixation control mechanism is probably relaxed in the carrier because the larger cone spacing of the carrier retina tolerates a larger degree of image motion without interfering with resolution. That is, the carrier is probably less stable than normal because they can tolerate a larger amount of retinal image motion without it interfering in their ability to see clearly.

### 5.5.3 Loss of Cones Leads to Loss of RGCs in the Carrier Retina

The discord seen between MAR and the theoretical Nyquist limit of the normal mRGC mosaic suggest that there are significant postreceptoral differences in the carrier retina. As outlined in the introduction there were two possible hypotheses concerning retinal circuitry in the carrier retina related to loss of functional cones. One hypothesis was that the reduced number of functional cones might be paired with a normal density of retinal ganglion cells, leading to a higher proportion of single cone centered mRGC receptive fields across the central fovea in the carrier retina. Single-cone centered mRGC receptive fields form the so-called private-line and if there were a normal density of mRGCs in the carrier retina, it would be expected that this private line might exist across the range of test locations. This hypothesis can be eliminated, as it is shown here that MAR and  $N_c$  are matched only at the PRLF and that MAR falls off at a greater rate than predicted by  $N_c$  just outside the PRLF, following the pattern seen for normal observers (Rossi et al., 2009).

The other hypothesis was that the loss of functional cones in BCM carriers would lead to a concomitant loss of RGCs. This hypothesis was supported by the psychophysical findings, which show that the relationship between MAR and  $N_c$  is similar to normal in the BCM carrier. Furthermore, it is shown here that the theoretical  $N_{mRGC}$  based upon mRGC receptive field density measurements from normal eyes (Drasdo et al., 2007) does not fit with the data obtained from BCM carriers, except for the most eccentric test location of BCMc2. The finding that carrier performance at all other test locations was worse than predicted by the model provides further evidence of loss of mRGCs in BCM. That this loss is local and is a consequence of the cone loss is supported by the results from BCMc2 at the most eccentric test location. This carrier was within the normal range on all measures at this test location, and fit well with the model prediction for  $N_{mRGC}$  limited resolution at that test location. This finding is consistent with the proposed coupled cone-RGC loss hypothesis: a reduction in mRGC density is predicted only where reduced cone density is observed.

### 5.5.4 MAR- $N_c$ Relationship is Similar to Normal Eyes Despite Coupled Cone-mRGC Loss in the Carrier Retina

Examining in detail the relationship between  $N_c$  and MAR found in the carrier, it can be seen that the relationship is similar to what was observed in both the normal retina and to what was predicted from the model of Drasdo and colleagues. As can be seen from Figure 46a, for a given  $N_c$ , the carriers achieved better MAR than the control eye and fell well within the normal limits measured in Chapter 4. However, the eccentricities at which equivalent MAR- $N_c$  pairings were found in the carrier were much closer to the PRLF than in normal retina. For a given MAR, the difference between  $N_c$  and MAR is similar in both the normal and carrier retina. In fact, corresponding values of  $N_c$  and MAR found in the carriers were similar to model predictions at all test locations, however, they were not found at the model-predicted eccentricities.

Figure 48 re-plots the data shown in Figure 46a, along with the data from the normal

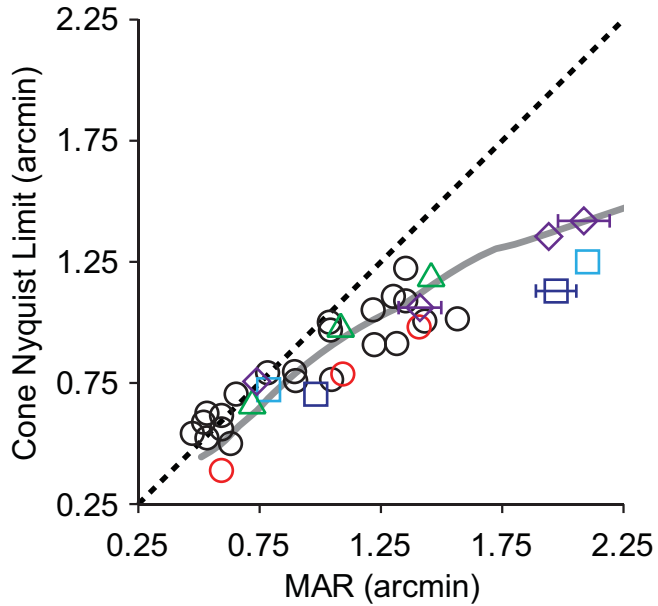


**Figure 48| BCM carriers and normal observers have a similar relationship between MAR and  $N_c$ .** Data from figure 46 is replotted with model predictions and data obtained in Chapter 4 for normal eyes. BCMc1 (OS), BCMc1 (OD), BCMc2, BCMc3, and control are shown respectively as light blue squares, dark blue squares, green triangles, purple diamonds, and red circles. Observers from Chapter 4 are shown as black circles. Dashed black line is the 1:1 line of equality. The solid line shows the mean  $N_c$  obtained by Curcio et al. (Curcio, Sloan, Kalina, & Hendrickson, 1990b) plotted against  $N_{mRGC}$  (an estimate of the neural MAR) from the model of Drasdo et al. (Drasdo, Millican, Katholi, & Curcio, 2007).

observers examined in Chapter 4, and a curve showing the theoretical relationship between  $N_c$  and the  $N_{mRGC}$  predicted from the Drasdo et al. model (Drasdo et al., 2007). Theoretical  $N_c$  was calculated from the average cone density across the horizontal meridian reported by Curcio using equation 4, using a conversion factor ( $m$ ) of 0.289 mm per degree (assuming that each eye was a 24 mm axial length emmetropic eye). For each eccentricity at which an  $N_c$  measurement was calculated, a corresponding value of  $N_{mRGC}$  was computed using the general model of mRGC receptive field density of Drasdo and colleagues (Drasdo et al., 2007). It can be seen that both the normal and carrier data points fall near the model prediction curve. Points near the PRLF for the experimental data are slightly shifted upward from model prediction. This is not surprising as  $N_c$  was estimated at the PRLF for 4 of 5 observers from the previous study in Chapter 4; these estimates contain errors and are, on average, higher than  $N_c$  estimates derived from the peak density measurements of Curcio. It is also likely that the estimate of  $N_c$  from the average data of Curcio contains some error because the true conversion factor for those eyes between mm and degrees of visual angle is not known. The large range of cone densities observed at the foveal center also makes predictions at this location subject to a large amount of variability.

The agreement between model predictions and empirical data was better outside the PRLF, where measurements of  $N_c$  were made directly. It is interesting to note that carrier data points beyond the range of test values obtained for normal observers still follow the trend predicted by the model. This shows that the carrier retina can be thought of, in effect, as an eccentricity-shifted version of the normal retina. For example, observer BCMc3 had a MAR of 1.41 arcmin when her  $N_c$  was 1.06 arcmin, falling near the model prediction for that MAR- $N_c$  pairing, however, the model predicts that this combination would be found at an eccentricity of  $\sim 2.3^\circ$  in a normal retina, whereas it was observed at an eccentricity of only  $0.86^\circ$  degrees in BCMc3, a difference of  $1.42^\circ$ .

What does this tell us about the retinal circuitry of the carrier retina? It seems to indicate that for a given cone spacing, the downstream neural circuitry is similar in both normal and carrier retinas. The major difference, aside from the cone loss, appears to be the relationship between cone spacing and eccentricity, because the relationship between  $N_c$  and MAR is not disrupted. This finding indicates that the  $N_{mRGC}$  is largely determined by the  $N_c$ . This suggests

that the number of mRGCs in the retina is directly related to the number of cones and that the cone loss seen in the carrier leads to a subsequent loss of RGCs.

It is hard to imagine how the visual system would deal with a mismatch between the number of cones and mRGCs. It seems possible that, as was suggested in the introduction, it might enable persistence of the so-called private line to larger eccentricities than found in the normal retina, outside the PRLF. However, it is not clear how a 4:1 ratio of mRGCs to cones would be implemented at the foveal center or if it would be advantageous. The ON- and OFF-center mRGC sub-mosaics are thought to be spatially redundant in the central fovea, requiring 2 mRGCs per cone; it does not seem plausible for there to be multiply redundant ON and OFF arrays or that there is a mechanism for such circuitry to be implemented. There may be a spatial limit to the size of a single-cone centered mRGC receptive field, as a discord between MAR and  $N_c$  at the PRLF in the carrier eye with the largest cone spacing was observed. However, as a discord between MAR and  $N_c$  at the PRLF was also observed, cortical factors are likely also involved in limiting MAR in the carrier, as is probably the case in myopia (Chapter 3). Further insight into the organization of mRGC receptive fields near the PRLF is required.

## 5.6 Conclusions

1. Peak cone density in BCM carriers is, on average, 50% lower than normal.
2. Cones destined to express the mutant opsin gene degenerate early in development.
3. Cone loss leads to loss of RGCs in the BCM carrier.
4. There is a similar relationship between MAR and  $N_c$  in the BCM carrier.
5. Cone density governs ganglion cell density in the human retina.

## Dissertation Summary

The main aim of the experiments described in this dissertation was to study the limits to visual resolution imposed at each stage in the visual process. The results of these experiments make several contributions towards this goal. Under natural viewing conditions the optics of the eye form a fundamental limit to visual resolution (Campbell et al., 1965). Minimizing this limitation with adaptive optics correction of ocular aberrations allowed for the effect of aberrations to be separated from retinal and cortical limits. The results of these experiments show that much of the large variability in visual resolution seen in normal eyes is a result of optical aberrations. When high order ocular aberrations are minimized with adaptive optics, the range of visual resolution measurements obtained for normal eyes is much smaller than is observed clinically, showing that much of the variability in visual resolution in normal eyes is due to optical factors alone.

The sampling theory of vision and previous research suggested that when optical factors were minimized the sampling limit of the cone mosaic would govern visual resolution across the central visual field. However, these experiments have revealed that this is not the case, as the actual situation is much more complex. The sampling limit of the cone mosaic only limits resolution very close to the foveal center and even for that case, only in some eyes. Even mild refractive error can cause an observer to not reach the visual resolution that might be attainable based upon optical and photoreceptor sampling limits alone, as was suggested by the results of Chapters 2 & 3, and confirmed by the results of Chapters 4 & 5. More evidence is required on the relationship between cone spacing and refractive error to validate this finding, but the results of Chapter 3 suggest that  $N_c$  would have to increase by 28% in mildly myopic eyes to fully account for the observed differences, an amount that seems unlikely for low myopia based on current evidence. Cortical insensitivity to high spatial frequencies must at least partially account for why all observers may not attain the resolution that may be afforded by retinal sampling limitations. The notion of adaptation to aberrations as a limiting mechanism seems implausible given the results presented in Chapter 2 and the complexities that this adaptation mechanism would have to exhibit that were discussed in Chapter 3.

The sampling limit of the mosaic of midget retinal ganglion cells appears to be the primary limiting factor that governs visual resolution across the visual field, as reductions in MAR with eccentricity closely match estimates of  $N_{mRGC}$ . This evidence supports the model of ganglion cell receptive field density across the visual field from which  $N_{mRGC}$  was estimated (Drasdo et al., 2007). Fascinating insight into the organization and development of the visual system has resulted by combining the knowledge gained in Chapters 2-4 with the study of carriers of BCM reported in Chapter 5. Since the genetic mutation in the carrier only affected the ability of a cone to make functional photopigment, this study provided compelling evidence that functional photopigment is required for cone photoreceptors to survive to maturity. Cone loss in the carrier led to dramatic reductions in MAR across the visual field that could best be explained by a subsequent loss of ganglion cells. Since the cause of the cone loss was purely due to the non-functioning photopigment gene, the loss of ganglion cells predicted by resolution measurements can be considered to be entirely a consequence of the loss of cones. This suggests that ganglion cell density is driven by cone density. The finding that resolution measurements were similar to model predictions based on the relationship between the  $N_c$  and  $N_{mRGC}$  provided further evidence that cone density is the primary determinant of the development of the RGC circuitry that underlies visual resolution in humans. Overall these studies make important contributions towards understanding the limits of human visual resolution.

## Reference List

- Ahumada, A. J. & Poirson, A. (1987). Cone sampling array models. *Journal of the Optical Society of America A*, 4, 1493-1502.
- American National Standards Institute. (2000). American National Standard for safe use of lasers. ANSI Z136.1-2000. ANSI.
- Anderson, R. S. & Thibos, L. N. (1999a). Relationship between acuity for gratings and tumbling-E letters in peripheral vision. *Journal of the Optical Society of America A*, 16, 2321-2333.
- Anderson, R. S. & Thibos, L. N. (1999b). Sampling limits and critical bandwidth for letter discrimination in peripheral vision. *Journal of the Optical Society of America A*, 16, 2334-2342.
- Applegate, R. A. (1991). Monochromatic aberrations in myopia. In *Noninvasive assessment of the visual system, Technical Digest Series* (pp. 234-237). Washington, D.C.: Optical Society of America.
- Applegate, R. A., Ballantine, C., Gross, H., Sarver, E. J., & Sarver, C. A. (2003a). Visual acuity as a function of Zernike mode and level of root mean square error. *Optometry and Vision Science*, 80, 97-105.
- Applegate, R. A., Marsack, J. D., Ramos, R., & Sarver, E. J. (2003b). Interaction between aberrations to improve or reduce visual performance. *Journal of Cataract and Refractive Surgery*, 29, 1487-1495.
- Arathorn, D. W., Yang, Q., Vogel, C. R., Zhang, Y., Tiruveedhula, P., & Roorda, A. (2007). Retinally stabilized cone-targeted stimulus delivery. *Optics Express*, 15, 13731-13741.
- Artal, P., Benito, A., & Tabernero, J. (2006). The human eye is an example of a robust optical design. *Journal of Vision*, 6, 1-7.
- Artal, P., Chen, L., Fernández, E. J., Singer, B., Manzanera, S., & Williams, D. R. (2004). Neural compensation for the eye's optical aberrations. *Journal of Vision*, 4, 281-287.
- Artal, P., Santamaría, J., & Bescós, J. (1988). Retrieval of wave aberration of human eyes from acutal point-spread-function data. *Journal of the Optical Society of America A*, 5, 1201-1206.
- Atchison, D. A., Schmid, K. L., & Pritchard, N. (2006). Neural and optical limits to visual performance in myopia. *Vision Research*, 46, 3707-3722.
- Ayyagari, R., Kakuk, L. E., Coats, C. L., Bingham, Y. T., Felius, J., & Sieving, P. A. (1999). Bilateral macular atrophy in blue cone monochromacy (BCM) with loss of the locus control region (LCR) and part of the red pigment gene. *Molecular Vision*, 5.

Azzopardi, P. & Cowey, A. (1993). Preferential representation of the fovea in the primary visual cortex. *Nature*, 361, 719-721.

Bailey, I. L. & Lovie, J. E. (1976). New design principles for visual acuity letter charts. *American Journal of Optometry and Physiological Optics*, 53, 740-745.

Baraas, R. C., Carroll, J., Gunther, K. L., Chung, M., Williams, D. R., Foster, D. H. et al. (2007). Adaptive optics retinal imaging reveals S-cone dystrophy in tritan color-vision deficiency. *Journal of the Optical Society of America A*, 24, 1438-1447.

Baron, W. S. & Westheimer, G. (1973). Visual acuity as a function of exposure duration. *Journal of the Optical Society of America*, 63, 212-219.

Beard, B. L., Levi, D. M., & Reich, L. N. (1995). Perceptual learning in parafoveal vision. *Vision Research*, 35, 1679-1690.

Bennett, A. G. & Rabbetts, R. B. (1989). *Clinical visual optics*. London: Butterworths.

Bennett, A. G., Rudnicka, A. R., & Edgar, D. F. (1994). Improvements on Littmann's method of determining the size of retinal features by fundus photography. *Graefe's Archive for Clinical and Experimental Ophthalmology*, 232, 361-367.

Berson, E. L., Sandberg, M. A., Maquire, A., Bromley, W. C., & Roderick, T. H. (1986). Electroretinograms in carriers of blue cone monochromatism. *American Journal of Ophthalmology*, 102, 254-261.

Bland, J. M. & Altman, D. G. (1986). Statistical methods for assessing agreement between two methods of clinical measurement. *The Lancet*, i, 307-310.

Bondarko, V. M. & Danilova, M. V. (1997). What spatial frequency do we use to detect the orientation of a Landolt C? *Vision Research*, 37, 2153-2156.

Brainard, D. H. (1997). The psychophysics toolbox. *Spatial Vision*, 10, 433-436.

Buehren, T., Collins, M. J., & Carney, L. G. (2005). Near work induced wavefront aberrations in myopia. *Vision Research*, 45, 1297-1312.

Burkhardt, J. (2005). HEX\_GRID Matlab Library [Computer software].  
[http://people.sc.fsu.edu/~burkhardt/m\\_src/hex\\_grid/hex\\_grid.html](http://people.sc.fsu.edu/~burkhardt/m_src/hex_grid/hex_grid.html).

Byram, G. M. (1944). The physical and photochemical basis of visual resolving power. *Journal of the Optical Society of America*, 34, 718-738.

Campbell, F. W. & Green, D. G. (1965). Optical and retinal factors affecting visual resolution. *Journal of Physiology*, 181, 576-593.

Campbell, F. W. & Robson, J. G. (1968). Application of Fourier analysis to the visibility of gratings. *Journal of Physiology*, 197, 551-566.

Campbell, M., Harrison, E., & Simonet, P. (1990). Psychophysical measurement of blur on the retina due to optical aberrations of the eye. *Vision Research*, 30, 1587-1602.

Carkeet, A., Luo, H. D., Tong, L., Saw, S. M., & Tan, D. T. (2002). Refractive error and monochromatic aberrations in Singaporean children. *Vision Research*, 42, 1809-1824.

Carroll, J., Neitz, J., & Neitz, M. (2002). Estimates of L:M cone ratio from ERG flicker photometry and genetics. *Journal of Vision*, 2, 531-542.

Carroll, J. C., Rossi, E. A., Porter, J., Tait, D. M., Neitz, J., Roorda, A. et al. (2009). Deletion of X-linked opsin gene array locus control region results in disrupted foveal morphology. *In Preparation*.

Charman, W. N. (2005). Aberrations and myopia. *Ophthalmic & Physiological Optics*, 25, 285-301.

Charman, W. N. & Simonet, P. (1997). Yves Le Grand and the assessment of retinal acuity using interference fringes. *Ophthalmic & Physiological Optics*, 17, 164-168.

Charman, W. N. & Walsh, G. (1985). The optical phase transfer function of the eye and the perception of spatial phase. *Vision Research*, 25, 619-623.

Chen, B., Makous, W., & Williams, D. R. (1993). Serial spatial filters in vision. *Vision Research*, 33, 413-427.

Chen, J. C., Brown, B., & Schmid, K. L. (2006). Delayed mfERG responses in myopia. *Vision Research*, 46, 1221-1229.

Chen, L., Artal, P., Gutierrez, D., & Williams, D. R. (2007). Neural compensation for the best aberration correction. *Journal of Vision*, 7, 9.1-9.

Chen, L., Singer, B., Guirao, A., Porter, J., & Williams, D. R. (2005). Image metrics for predicting subjective image quality. *Optometry and Vision Science*, 82, 358-369.

Cheng, H., Barnett, J. K., Vilupuru, A. S., Marsack, J. D., Kasthurirangan, S., Applegate, R. A. et al. (2004). A population study on changes in wave aberrations with accommodation. *Journal of Vision*, 4, 272-280.

Cheng, X., Bradley, A., Hong, X., & Thibos, L. N. (2003). Relationship between refractive error and monochromatic aberrations of the eye. *Optometry and Vision Science*, 80, 43-49.

Chui, T. Y., Yap, M. K., Chan, H. H., & Thibos, L. N. (2005). Retinal stretching limits peripheral visual acuity in myopia. *Vision Research*, 45, 593-605.

Chui, T. Y. P., Song, H., & Burns, S. A. (2008). Individual variations in human cone photoreceptor packing density: variations with refractive error. *Investigative Ophthalmology & Visual Science*, 49, 4679-4687.

- Coletta, N. J. & Watson, T. (2006). Effect of myopia on visual acuity measured with laser interference fringes. *Vision Research*, 46, 636-651.
- Coletta, N. J. & Williams, D. R. (1987). Psychophysical estimate of extrafoveal cone spacing. *Journal of the Optical Society of America A*, 4, 1503-1513.
- Collins, J. W. & Carney, L. G. (1990). Visual performance in high myopia. *Current Eye Research*, 9, 217-223.
- Collins, M. J., Wildsoet, C. F., & Atchison, D. A. (1995). Monochromatic aberrations and myopia. *Vision Research*, 35, 1157-1163.
- Cowey, A. & Rolls, E. T. (1974). Human cortical magnification factor and its relation to visual acuity. *Experimental Brain Research*, 21, 447-454.
- Curcio, C. A. & Allen, K. A. (1990a). Topography of ganglion cells in human retina. *The Journal of Comparative Neurology*, 300, 5-25.
- Curcio, C. A. & Sloan, K. R. (1992). Packing geometry of human cone photoreceptors: variation with eccentricity and evidence for local anisotropy. *Visual Neuroscience*, 9, 169-180.
- Curcio, C. A., Sloan, K. R., Kalina, R. E., & Hendrickson, A. E. (1990b). Human photoreceptor topography. *The Journal of Comparative Neurology*, 292, 497-523.
- Curcio, C. A., Sloan, K. R., Packer, O., Hendrickson, A. E., & Kalina, R. E. (1987). Distribution of cones in human and monkey retina: individual variability and radial asymmetry. *Science*, 236, 579-582.
- D'Zmura (1996). Bergmann on visual resolution. *Perception*, 25, 1223-1234.
- Dacey, D. M. (1993). The mosaic of midget ganglion cells in the human retina. *Journal of Neuroscience*, 13, 5334-5355.
- Derrington, A. M. & Lennie, P. (1984). Spatial and temporal contrast sensitivities of neurones in lateral geniculate nucleus of macaque. *Journal of Physiology*, 357, 219-240.
- DeValois, R. L., Albrecht, D. G., & Thorell, L. G. (1982). Spatial frequency selectivity of cells in macaque visual cortex. *Vision Research*, 22, 545-560.
- DeValois, R. L. & DeValois, K. K. (1988). *Spatial vision*. Oxford psychology series no. 14. New York: Oxford University Press.
- DeVries, S. H., Qi, X. S. R., Makous, W., & Sterling, P. (2002). Electrical coupling between mammalian cones. *Current Biology*, 12, 1900-1907.
- Drasdo, N. (1977). The neural representation of visual space. *Nature*, 266, 554-556.

Drasdo, N., Millican, C. L., Katholi, C. R., & Curcio, C. A. (2007). The length of Henle fibers in the human retina and a model of ganglion receptive field density in the visual field. *Vision Research*, 47, 2901-2911.

Duncan, R. O. & Boynton, G. M. (2003). Cortical magnification within human primary visual cortex correlates with acuity thresholds. *Neuron*, 38, 659-671.

Enoch, J. M. (1963). Optical properties of the retinal receptors. *Journal of the Optical Society of America*, 53, 71-85.

Enoch, J. M. & Hope, G. M. (1973). Interferometric resolution determinations in the fovea and parafovea. *Documenta Ophthalmologica*, 34, 143-156.

Fernández, E. J., Prieto, P. M., & Artal, P. (2009). Bonocular adaptive optics visual simulator. *Optics Letters*, 34, 2628-2630.

Fine, I. & Jacobs, R. A. (2002). Comparing perceptual learning across tasks: a review. *Journal of Vision*, 2, 190-203.

Fiorentini, A. & Maffei, L. (1976). Spatial contrast sensitivity of myopic subjects. *Vision Research*, 16, 437-438.

Gardner, J. C., Michaelides, M., Holder, G. E., Kanuga, N., Webb, T. R., Mollon, J. D. et al. (2009). Blue cone monochromacy: Causative mutations and associated phenotypes. *Molecular Vision*, 15, 876-884.

George, S. & Rosenfield, M. (2004). Blur adaptation and myopia. *Optometry and Vision Science*, 81, 543-547.

Georgeson, M. A. & Sullivan, G. D. (1975). Contrast constancy: deblurring in human vision by spatial frequency channels. *Journal of Physiology*, 252, 627-656.

Goodman, J. W. (1968). *Introduction to Fourier optics*. San Francisco: McGraw-Hill.

Gottlob, I. (1994). Eye movement abnormalities in carriers of blue-cone monochromatism. *Investigative Ophthalmology & Visual Science*, 35, 3556-3560.

Green, D. G. (1970). Regional variations in the visual acuity for interference fringes on the retina. *Journal of Physiology*, 207, 351-356.

Green, D. G. & Campbell, F. W. (1965). Effect of focus on the visual response to a sinusoidally modulated spatial stimulus. *Journal of the Optical Society of America*, 55, 1154-1157.

Grieve, K., Tiruveedhula, P., Zhang, Y., & Roorda, A. (2006). Multi-wavelength imaging with the adaptive optics scanning laser ophthalmoscope. *Optics Express*, 14, 12230-12242.

Guez, J. E., Le Gargasson, J. F., Massin, P., Rigaudière, F., Grall, T., & Gaudric, A. (1998). Functional assessment of macular hole surgery by scanning laser ophthalmoscopy. *Ophthalmology, 105*, 694-699.

Hartmann, J. (1900). Bemerkungen ueber den Bau und die Justierung von Spktrographen. *Zeitschrift fuer Instrumentenkunde, 20*, 47.

He, J. C., Sun, P., Held, R., Thorn, F., Sun, X., & Gwiazda, J. E. (2002). Wavefront aberrations in eyes of emmetropic and moderately myopic school children and young adults. *Vision Research, 42*, 1063-1070.

Helmholtz, H. V. (1962). *Helmholtz's Treatise on Physiological Optics*. (vols. I & II) New York: Dover Publications, Inc.

Herzog, M. H. & Fahle, M. (1997). The role of feedback in learning a vernier discrimination task. *Vision Research, 37*, 2133-2141.

Hirsch, J. & Hylton, R. (1984). Quality of the primate photoreceptor lattice and limits of spatial vision. *Vision Research, 24*, 347-355.

Hirsch, J. & Miller, W. H. (1987). Does cone positional disorder limit resolution? *Journal of the Optical Society of America A, 4*, 1481-1492.

Hirsch, M. J. (1945). Relation of visual acuity to myopia. *Archives of Ophthalmology, 34*, 418-421.

Hofer, H., Carroll, J., Neitz, J., Neitz, M., & Williams, D. R. (2005). Organization of the human trichromatic cone mosaic. *Journal of Neuroscience, 25*, 9669-9679.

Hofer, H., Chen, L., Yoon, G.-Y., Singer, B., Yamauchi, Y., & Williams, D. R. (2001). Improvement in retinal image quality with dynamic correction of the eye's aberrations. *Optics Express, 8*, 631-643.

Howell, E. R. & Hess, R. F. (1978). The functional area for summation to threshold for sinusoidal gratings. *Vision Research, 18*, 369-374.

Howland, B. & Howland, H. C. (1976). Subjective measurement of high-order aberrations of the eye. *Science, 193*, 580-582.

Howland, H. C. (2000). The history and methods of ophthalmic wavefront sensing. *Journal of Refractive Surgery, 16*, S552-S553.

Howland, H. C. & Howland, B. (1977). A subjective method for the measurement of monochromatic aberrations of the eye. *Journal of the Optical Society of America, 67*, 1508-1518.

Hubel, D. H. & Wiesel, T. N. (1974). Uniformity of monkey striate cortex: a parallel relationship between field size, scatter, and magnification factor. *Journal of Comparative Neurology, 158*, 295-305.

Jaworski, A., Gentle, A., Zele, A. J., Vingrys, A. J., & McBrien, N. A. (2006). Altered visual sensitivity in axial high myopia: a local postreceptoral phenomenon? *Investigative Ophthalmology & Visual Science*, 47, 3695-3702.

Johnson, C. A. & Leibowitz, H. W. (1979). Practice effects for visual resolution in the periphery. *Perception & Psychophysics*, 25, 439-442.

Karni, A., Tanne, D., Rubenstein, B. S., Askenasy, J. J., & Sagi, D. (1994). Dependence on REM sleep of overnight improvement of a perceptual skill. *Science*, 265, 679-682.

Kastner, S., Schneider, K. A., & Wunderlich, K. (2006). Beyond a relay nucleus: neuroimaging views on the human LGN. *Progress in Brain Research*, 155, 125-143.

Kawabata, H. & Adachi-Usami, E. (1997). Multifocal electroretinogram in myopia. *Investigative Ophthalmology & Visual Science*, 38, 2844-2851.

Kolb, H. (1970). Organization of the outer plexiform layer of the primate retina: electron microscopy of golgi impregnated cells. *Philosophical Transactions of the Royal Society, London, B*, 258, 261-283.

Kolb, H. & Marshak, D. (2003). The midget pathways of the primate retina. *Documenta Ophthalmologica*, 106, 67-81.

Krill, A. E. (1977). Congenital Color Vision Defects. In *Krill's Hereditary Retinal and Choroidal Diseases. Volume II. Clinical Characteristics*. (pp. 355-390). Hagerstown, MD: Harper & Row.

Le Gargasson, J. F., Rigaudiere, F., Guez, J. E., Schmitt, D., & Grall, Y. (1992). Value of scanning laser ophthalmoscopy in the evaluation of the visual function of 47 patients with moderate cataracts associated with maculopathyVI. Value of scanning laser ophthalmoscopy in the evaluation of optotype reading capacities. *Clinical Vision Sciences*, 7, 531-540.

Levi, D. M., Klein, S. A., & Aitsebaomo, A. P. (1985). Vernier acuity, crowding and cortical magnification. *Vision Research*, 25, 963-977.

Li, K. Y., Tiruveedhula, P., & Roorda, A. (2009). Adaptive optics imaging and analysis of cone photoreceptors near the fovea center. *Investigative Ophthalmology & Visual Science* 50[E-Abstract 4770].

Ref Type: Abstract

Li, K. Y. & Roorda, A. (2007). Automated identification of cone photoreceptors in adaptive optics retinal images. *Journal of the Optical Society of America A*, 24, 1358-1363.

Liang, J., Grimm, B., Goelz, S., & Bille, J. F. (1994). Objective measurement of wave aberrations of the human eye with the use of a Hartmann-Schack wave-front sensor. *Journal of the Optical Society of America A*, 11, 1949-1957.

- Liang, J., Williams, D. R., & Miller, D. T. (1997). Supernormal vision and high-resolution retinal imaging through adaptive optics. *Journal of the Optical Society of America A*, 14, 2884-2892.
- Liou, S. W. & Chiu, C. J. (2001). Myopia and contrast sensitivity function. *Current Eye Research*, 22, 81-84.
- Ludvigh, E. (1941). Extrafoveal visual acuity as measured with snellen test letters. *American Journal of Ophthalmology*, 24, 303-310.
- MacLeod, D. I. A., Williams, D. R., & Makous, W. (1992). A visual nonlinearity fed by single cones. *Vision Research*, 32, 347-363.
- Mainster, M. A., Timberlake, G. T., Webb, R. H., & Hughes, G. W. (1982). Scanning laser ophthalmoscopy. *Ophthalmology*, 89, 852-857.
- Marcos, S., Berbero, S., & Llorente, L. (2002). The sources of optical aberrations in myopic eyes. *Investigative Ophthalmology & Visual Science*, 43, E-Abstract 1510.
- Marcos, S. & Navarro, R. (1997). Determination of the foveal cone spacing by ocular speckly interferometry: Limiting factors and acuity predictions. *Journal of the Optical Society of America A*, 14, 731-740.
- McMahon, M. J., Lankheet, M. J. M., Lennie, P., & Williams, D. R. (2000). Fine structure of parvocellular receptive fields in the primate fovea revealed by laser interferometry. *The Journal of Neuroscience*, 20, 2043-2053.
- Merigan, W. H. & Katz, L. M. (1990). Spatial resolution across the macaque retina. *Vision Research*, 30, 985-991.
- Mersereau, R. M. (1979). The processing of hexagonally sampled two-dimensional signals. *Proceedings of the IEEE*, 67, 930-953.
- Mon-Williams, M., Tresilian, J. R., Strang, N. C., Kochhar, P., & Wann, J. P. (1998). Improving vision: neural compensation for optical defocus. *Proceedings of the Royal Society B: Biological Sciences*, 265, 71-77.
- Nathans, J., Davenport, C. M., Maumenee, I. H., Lewis, R. A., & Hejtmancik, J. F. (1989). Molecular genetics of human blue cone monochromacy. *Science*, 245, 831-838.
- Nathans, J., Maumenee, I. H., Zrenner, E., Sadowski, B., Sharpe, L. T., Lewis, R. A. et al. (1993). Genetic heterogeneity among blue-cone monochromats. *The American Journal of Human Genetics*, 53, 987-1000.
- Nathans, J., Thomas, D., & Hogness, D. S. (1986). Molecular genetics of human color vision: the genes encoding blue, green and red pigments. *Science*, 232, 202.

- Netto, M. V., Ambrósio, R. Jr., Shen, T. T., & Wilson, S. E. (2005). Wavefront analysis in normal refractive surgery candidates. *Journal of Refractive Surgery*, 21, 332-338.
- Nyquist, H. (1928). Certain topics in telegraph transmission theory. *Transactions of the A.I.E.E.*, 617-644.
- Østerberg, G. A. (1935). Topography of the layer of rods and cones in the human retina. *Acta Ophthalmologica*, 13, 1-97.
- Packer, O. & Williams, D. R. (2003). Light, the retinal image, and photoreceptors. In S.K. Shevell (Ed.), *The science of color* (2 ed., pp. 41-102). Amsterdam; Boston: Elsevier.
- Pallikaris, A., Williams, D. R., & Hofer, H. (2003). The reflectance of single cones in the living human eye. *Investigative Ophthalmology & Visual Science*, 44, 4580-4592.
- Paquin, M. P., Hamam, H., & Simonet, P. (2002). Objective measurement of optical aberrations in myopic eyes. *Optometry and Vision Science*, 79, 285-291.
- Parker, A. J. & Hawken, M. J. (1985). Capabilities of monkey cortical cells in spatial-resolution tasks. *Journal of the Optical Society of America*, A, 2, 1101-1114.
- Pelli, D. G. (1997). The VideoToolbox software for visual psychophysics: Transforming numbers into movies. *Spatial Vision*, 10, 437-442.
- Pesudovs, K. (2005). Involvement of neural adaptation in the recovery of vision after laser refractive surgery. *Journal of Refractive Surgery*, 21, 144-147.
- Piotrowski, L. N. & Campbell, F. W. (1982). A demonstration of the visual importance and flexibility of spatial-frequency amplitude and phase. *Perception*, 11, 337-346.
- Pokorny, J., Smith, V. C., Verriest, G., & Pinckers, A. J. L. G. (1979). *Congenital and acquired color vision defects*. New York: Grune & Stratton.
- Polat, U. & Tyler, C. W. (1999). What pattern the eye sees best. *Vision Research*, 39, 887-895.
- Polyak, S. L. (1941). *The retina*. Chicago: University of Chicago Press.
- Poonja, S., Patel, S., Henry, L., & Roorda, A. (2005). Dynamic visual stimulus presentation in an adaptive optics scanning laser ophthalmoscope. *Journal of Refractive Surgery*, 21, 575-580.
- Porter, J., Guirao, A., Cox, I. G., & Williams, D. R. (2001). Monochromatic aberrations of the human eye in a large population. *Journal of the Optical Society of America*, A, 18, 1793-1803.
- Putnam, N. M., Hofer, H., Doble, N., Chen, L., Carroll, J., & Williams, D. R. (2005). The locus of fixation and the foveal cone mosaic. *Journal of Vision*, 5(7), 632-639.

Radhakrishnan, H., Pardhan, S., Calver, R. I., & O'Leary, D. J. (2004a). Effect of positive and negative defocus on contrast sensitivity in myopes and non-myopes. *Vision Research*, 44, 1869-1878.

Radhakrishnan, H., Pardhan, S., Calver, R. I., & O'Leary, D. J. (2004b). Unequal reduction in visual acuity with positive and negative defocusing lenses in myopes. *Optometry and Vision Science*, 81, 14-17.

Rentschler, I. & Treutwein, B. (1985). Loss of spatial phase relationships in extrafoveal vision. *Nature*, 313, 308-310.

Robson, J. G. & Graham, N. (1981). Probability summation and regional variation in contrast sensitivity across the visual field. *Vision Research*, 21, 409-418.

Roorda, A. & Glasser, A. (2004). Wave aberrations of the isolated crystalline lens. *Journal of Vision*, 4, 250-261.

Roorda, A. & Williams, D. R. (2002a). Optical fiber properties of individual human cones. *Journal of Vision*, 2, 404-412.

Roorda, A., Romero-Borja, W., Donnelly, W. J., III, Queener, H., Hebert, T., & Campbell, M. (2002b). Adaptive optics scanning laser ophthalmoscopy. *Optics Express*, 10, 405-412.

Rosenblum, W. M. & Christensen, J. L. (1976). Objective and subjective spherical aberration measurement of the human eye. In E. Wolf (Ed.), *Progress in Optics* (pp. 69-91). North-Holland, Amsterdam.

Rosenfield, M., Hong, S. E., & George, S. (2004). Blur adaptation in myopes. *Optometry and Vision Science*, 81, 657-662.

Rossi, E. A. & Roorda, A. (2009). The relationship between visual resolution and cone spacing in the human fovea. *Nature Neuroscience*.

Rossi, E. A., Weiser, P., Tarrant, J., & Roorda, A. (2007). Visual performance in emmetropia and low myopia after correction of high-order aberrations. *Journal of Vision*, 7(8), 1-14.

Rovamo, J. & Virsu, V. (1979). An estimation and application of the human cortical magnification factor. *Experimental Brain Research*, 37, 495-510.

Rovamo, J., Virsu, V., & Näsänen, R. (1978). Cortical magnification factor predicts the photopic contrast sensitivity of peripheral vision. *Nature*, 271, 54-56.

Saarinen, J., Rovamo, J., & Virsu, V. (1989). Analysis of spatial structure in eccentric vision. *Investigative Ophthalmology & Visual Science*, 30, 293-296.

Sarver, E. J. & Applegate, R. A. (2004). The importance of the phase transfer function to visual function and visual quality metrics. *Journal of Refractive Surgery*, 20, S504-S507.

Shannon, C. E. (1949). Communication in the presence of noise. *Proceedings of the IRE*, 37, 10-21.

Sharpe, L. T., Stockman, A., Jägle, H., & Nathans, J. (1999). Opsin genes, cone photopigments, color vision, and color blindness. In K.R. Gegenfurtner & L. T. Sharpe (Eds.), *Color vision: from genes to perception* (pp. 3-52). Cambridge, UK: Cambridge University Press.

Shira, M. M., Wade, A. R., & Tyler, C. W. (2007). Two-dimensional mapping of the central and parafoveal visual field to human visual cortex. *Journal of Neurophysiology*, 97, 4284-4295.

Shlaer, S. (1937). The relation between visual acuity and illumination. *The Journal of General Physiology*, 21, 165-187.

Simonet, P. & Campbell, M. C. W. (1990). The optical transverse chromatic aberration on the fovea of the human eye. *Vision Research*, 30, 187-206.

Sincich, L. C., Zhang, Y., Tiruveedhula, P., Horton, J. C., & Roorda, A. (2009). Resolving single cone inputs to visual receptive fields. *Nature Neuroscience*, 12, 967-969.

Smallman, H. S., MacLeod, D. I. A., He, S., & Kentridge, R. W. (1996). Fine grain of the neural representation of human spatial vision. *Journal of Neuroscience*, 16, 1852-1859.

Snyder, A. W. & Miller, W. H. (1977). Receptor diameter and spacing for highest resolving power. *Journal of the Optical Society of America*, 67, 696-698.

Spivey, B. E., Pearlman, J. T., & Burian, H. M. (1964). Electroretinographic findings (including flicker) in carriers of congenital X-linked achromatopsia. *Documenta Ophthalmologica*, 18, 367-375.

Steinman, R. M. (1965). Effect of target size, luminance, and color on monocular fixation. *Journal of the Optical Society of America*, 55, 1158-1165.

Steinman, R. M., Pizlo, Z., Forofonova, T. I., & Epelboim, J. (2003). One fixates accurately *in order to* see clearly not *because* one sees clearly. *Spatial Vision*, 16, 225-241.

Stiles, W. S. & Crawford, B. H. (1933). The luminous efficiency of rays entering the eye pupil at different points. *Proceedings of the Royal Society of London. Series B: Biological Sciences*, 112, 428-450.

Strang, N. C., Winn, B., & Bradley, A. (1998). The role of neural and optical factors in limiting visual resolution in myopia. *Vision Research*, 38, 1713-1721.

Subbaram, M. V. & Bullimore, M. A. (2002). Visual acuity and the accuracy of the accommodative response. *Ophthalmic & Physiological Optics*, 22, 312-318.

- Thibos, L. N. (1998). Acuity perimetry and the sampling theory of visual resolution. *Optometry and Vision Science*, 75, 399-406.
- Thibos, L. N. (2000). Formation and sampling of the retinal image. In K.K. De Valois (Ed.), *Seeing* (pp. 1-49). San Diego: Academic Press.
- Thibos, L. N., Bradley, A., Still, D. L., Zhang, X., & Howarth, P. A. (1990). Theory and measurement of ocular chromatic aberration. *Vision Research*, 30, 33-49.
- Thibos, L. N., Cheney, F. E., & Walsh, D. J. (1987). Retinal limits to the detection and resolution of gratings. *Journal of the Optical Society of America A*, 4, 1524-1529.
- Thorn, F., Corwin, T. R., & Comerford, J. P. (1986). High myopia does not affect contrast sensitivity. *Current Eye Research*, 5, 639.
- Thorn, F. & Schwartz, F. (1990). Effect of dioptric blur on Snellen and grating acuity. *Optometry and Vision Science*, 67, 3-7.
- Timberlake, G. T., Mainster, M. A., Peli, E., Augliere, R. A., Essock, E. A., & Arend, L. E. (1986). Reading with a macular scotoma. I. Retinal location of scotoma and fixation area. *Investigative Ophthalmology & Visual Science*, 27, 1137-1147.
- Timberlake, G. T., Mainster, M. A., Webb, R. H., Hughes, G. W., & Tempe, C. L. (1982). Retinal localization of scotomata by scanning laser ophthalmoscopy. *Investigative Ophthalmology & Visual Science*, 22, 91-97.
- Tomita, T. (1970). Electrical activity of vertebrate photoreceptors. *Quarterly reviews of biophysics*, 3, 179-222.
- Troilo, D., Xiong, M., Crowley, J. C., & Finlay, B. L. (1996). Factors controlling the dendritic arborization of retinal ganglion cells. *Visual Neuroscience*, 13, 721-733.
- Tscherning, M. (1894). Die Monochromatischen abberationen des Menschlichen Auges. *Z.Psychol.Physiol.Sinn.*, 6, 456-471.
- Virsu, V. & Rovamo, J. (1979). Visual resolution, contrast sensitivity, and the cortical magnification factor. *Experimental Brain Research* 37, 475-494.
- Walsh, G., Charman, W. N., & Howland, H. C. (1984). Objective technique for the determination of monochromatic aberrations of the human eye. *Journal of the Optical Society of America A*, 1, 987-992.
- Wang, Y., Macke, J. P., Merbs, S. L., Zack, D. J., Klaunberg, B., Bennett, J. et al. (1992). A locus control region adjacent to the human red and green visual pigment genes. *Neuron*, 9, 429-440.
- Wässle, H., Grünert, U., Röhrenbeck, J., & Boycott, B. B. (1989). Cortical magnification factor and the ganglion cell density of the primate retina. *Nature*, 341, 643-646.

Wässle, H., Grünert, U., Röhrenbeck, J., & Boycott, B. B. (1990). Retinal ganglion cell density and cortical magnification factor in the primate. *Vision Research*, 30, 1897-1911.

Watson, A. B. & Pelli, D. G. (1983). QUEST: A Bayesian adaptive psychometric method. *Perception & Psychophysics*, 33, 113-120.

Webb, R. H., Hughes, G. W., & Pomerantzeff, O. (1980). Flying spot TV ophthalmoscope. *Applied Optics*, 19, 2991-2997.

Webster, M. A., Georgeson, M. A., & Webster, S. M. (2002). Neural adjustments to image blur. *Nature Neuroscience*, 5, 839-840.

Weiskrantz, L. & Cowey, A. (1963). Striate cortex lesions and visual acuity of the rhesus monkey. *Journal of Comparative and Physiological Psychology*, 56, 225-231.

Wertheim, T. (1894). Über die indirekte Sehschärfe. *Zeitschrift für Psychologie*, 7, 172-189.

Westheimer, G. (2006). Specifying and controlling the optical image on the human retina. *Progress in Retinal and Eye Research*, 25, 19-42.

Westheimer, G. (1960). Modulation thresholds for sinusoidal light distributions on the retina. *Journal of Physiology*, 152, 67-74.

Westheimer, G. (1966). The Maxwellian view. *Vision Research*, 6, 669-682.

Westheimer, G. (1982). The spatial grain of the perifoveal visual field. *Vision Research*, 22, 157-162.

Westheimer, G. (2001). Is peripheral visual acuity susceptible to perceptual learning in the adult? *Vision Research*, 41, 47-52.

Westheimer, G. (2003). Visual acuity. In P.L. Kaufman & A. Alm (Eds.), *Adler's physiology of the eye* (10th ed., pp. 453-469). St. Louis: Mosby.

Westheimer, G. & McKee, S. P. (1975). Visual acuity in the presence of retinal-image motion. *Journal of the Optical Society of America*, 65, 847-850.

Weymouth, F. W. (1958). Visual sensory units and the minimum angle of resolution. *American Journal of Ophthalmology*, 46, 102-113.

Weymouth, F. W., Hines, D. C., Acres, L. H., Raaf, J. W., & Wheeler, M. C. (1928). Visual acuity within the area centralis and its relation to eye movements and fixation. *American Journal of Ophthalmology*, 11, 947-960.

Wildsoet, C. F., Atchison, D. A., & Collins, M. J. (1993). Longitudinal chromatic aberration as a function of refractive error. *Clinical & Experimental Optometry*, 76, 119-122.

Williams, D. R. & Hofer, H. (2004). Formation and acquisition of the retinal image. In L.M.Chalupa & J. S. Werner (Eds.), *The visual neurosciences* (pp. 795-810). Cambridge, MA: The MIT Press.

Williams, D., Sekiguchi, N., & Brainard, D. (1993). Color, contrast sensitivity, and the cone mosaic. *Proceedings of the National Academy of Sciences*, 90, 9770-9777.

Williams, D., Yoon, G.-Y., Porter, J., Guirao, A., Hofer, H., & Cox, I. (2000). Visual benefit of correcting higher order aberrations of the eye. *Journal of Refractive Surgery*, 16, S554-S559.

Williams, D. R. (1985a). Aliasing in human foveal vision. *Vision Research*, 25, 195-205.

Williams, D. R. (1985b). Visibility of interference fringes near the resolution limit. *Journal of the Optical Society of America A*, 2, 1087-1093.

Williams, D. R. (1986). Seeing through the photoreceptor mosaic. *Trends in Neuroscience*, 9, 193-198.

Williams, D. R. (1988). Topography of the foveal cone mosaic in the living human eye. *Vision Research*, 3, 433-454.

Williams, D. R. & Coletta, N. J. (1987). Cone spacing and the visual resolution limit. *Journal of the Optical Society of America A*, 4, 1514-1522.

Williams, D. R. & Collier, R. (1983). Consequences of spatial sampling by a human photoreceptor mosaic. *Science*, 221, 385-387.

Wyszecki, G. & Stiles, W. S. (1982). *Color science: Concepts and methods, quantitative data and formulae*. (2nd ed.) New York, NY: John Wiley & Sons.

Yap, Y. L., Levi, D. M., & Klein, S. A. (1987). Peripheral hyperacuity: three-dot bisection scales to a single factor from 0 to 10 degrees. *Journal of the Optical Society of America A*, 4, 1554-1561.

Yau, K.-W. (1994). Phototransduction mechanisms in retinal rods and cones. *Investigative Ophthalmology & Visual Science*, 35, 9-32.

Yellott, J. I. (1982). Spectral analysis of spatial sampling by photoreceptors: topological disorder prevents aliasing. *Vision Research*, 22, 1205-1210.

Yellott, J. I. (1983). Spectral consequences of photoreceptor sampling in the rhesus retina. *Science*, 221, 382-385.

Yoon, G. Y., Jeong, T. M., Cox, I. G., & Williams, D. R. (2004). Vision improvement by correcting high-order aberrations with phase plates in normal eyes. *Journal of Refractive Surgery*, 20, S527.

Yoon, G. Y., Jeong, T. M., Cox, I. G., & Williams, D. R. (2009). Vision improvement by correcting high-order aberrations with phase plates in normal eyes. *Journal of Refractive Surgery*, 20, S527.

Yoon, G.-Y. & Williams, D. R. (2002). Visual performance after correcting the monochromatic and chromatic aberrations of the eye. *Journal of the Optical Society of America A*, 19, 266-275.

Yoon, M. K., Roorda, A., Zhang, Y., Nakanishi, C., Wong, L.-J. C., Zhang, Q. et al. (2009). Adaptive optics scanning laser ophthalmoscopy images in a family with the mitochondrial DNA T8993C mutation. *Investigative Ophthalmology & Visual Science*, 50, 1838-1847.

Zadok, D., Levy, Y., Segal, O., Barkana, Y., Morad, Y., & Avni, I. (2005). Ocular higher-order aberrations in myopia and skiascopic wavefront repeatability. *Journal of Cataract and Refractive Surgery*, 31, 1128-1132.

Zhang, X., Bradley, A., & Thibos, L. N. (1993). Experimental determination of the chromatic difference of magnification of the human eye and the location of the anterior nodal point. *Journal of the Optical Society of America A*, 10, 213-220.

Zhang, X., Thibos, L. N., & Bradley, A. (1991). Relation between the chromatic difference of refraction and the chromatic difference of magnification for the reduced eye. *Optometry and Vision Science*, 68, 456-458.

Zhang, Y., Poonja, S., & Roorda, A. (2006). MEMS-based adaptive optics laser ophthalmoscopy. *Optics Letters*, 31, 1268-1270.

Zhang, Y. & Roorda, A. (2006). Evaluating the lateral resolution of the adaptive optics scanning laser ophthalmoscope. *Journal of Biomedical Optics*, 11, 014002-1-014002-5.